

Comparison and synthesis of sea-level and deep-sea temperature variations over the past 40 million years

Eelco J Rohling^{1,1}, Gavin Lee Foster^{2,2}, Thomas Gernon^{2,2}, Katharine Grant^{1,1}, David Heslop^{3,3}, Fiona D Hibbert^{4,4}, Andrew P. Roberts^{1,1}, and Jimin Yu^{1,1}

¹Australian National University

²University of Southampton

³Research School of Earth Sciences

⁴University of York

November 30, 2022

Abstract

Global ice volume (sea level) and deep-sea temperature are key measures of Earth's climatic state. We synthesize evidence for multi-centennial to millennial ice-volume and deep-sea temperature variations over the past 40 million years, which encompass the early glaciation of Antarctica at ~34 million years ago (Ma), the end of the Middle Miocene Climate Optimum, and the descent into the bipolar glaciation state from ~3.4 Ma. We compare different sea-level and deep-water temperature reconstructions that are grounded in data to build a resource for validation of long-term numerical model-based approaches. We present: (a) a new ice-volume and deep-sea temperature synthesis for the past 5.3 million years; (b) a single template reconstruction of ice-volume and deep-sea temperature for the interval between 5.3 and 40 Ma; and (c) a discussion of uncertainties and limitations. We highlight key issues associated with glacial state changes in the geological record from 40 Ma to the present that require specific attention in further research. These include offsets between calibration-sensitive versus more thermodynamically guided deep-sea paleothermometry proxy measurements; a conundrum related to the magnitudes of sea-level and deep-sea temperature change at the Eocene-Oligocene transition at 34 Ma; a discrepancy in deep-sea temperature levels during the Middle Miocene between proxy reconstructions and model-based deconvolutions of deep-sea oxygen isotope data; and a hitherto unquantified non-linear reduction of glacial deep-sea temperatures through the past 3.4 million years toward a near-freezing deep-sea temperature asymptote, while sea level stepped down in a more linear manner.

Comparison and synthesis of sea-level and deep-sea temperature variations over the past 40 million years

Eelco J. Rohling^{1,2}, Gavin L. Foster², Thomas M. Gernon², Katharine M. Grant¹, David Heslop¹, Fiona D. Hibbert³, Andrew P. Roberts¹, Jimin Yu^{1,4}

1. Research School of Earth Sciences, Australian National University, Canberra, ACT 2601, Australia.
2. Ocean and Earth Science, University of Southampton, National Oceanography Centre, Southampton, SO14 3ZH, UK.
3. Department of Environment and Geography, University of York, York, YO10 5NG, UK.
4. Pilot National Laboratory for Marine Science and Technology (Qingdao), Qingdao, 266237, China.

Plain Language Summary	3
ABSTRACT	4
1. INTRODUCTION	5
2. DEFINITIONS AND APPROACH	9
3. LONG-TERM ICE-VOLUME OR SEA-LEVEL RECORDS	17
3.1. <i>Scaling of δ_c records to sea-level</i>	18
3.2. <i>Statistical deconvolution of ice-volume and deep-sea temperature impacts on δ_c</i>	19
3.3. <i>Paired δ_c and Mg/Ca or clumped isotope-based temperature measurements</i>	21
3.4. <i>The marginal sea residence-time method</i>	24
3.5. <i>Statistically generalized sea-level records from diverse suites of input records</i>	27
3.6. <i>Inverse modeling</i>	28
3.7. <i>Process modeling of ice-volume, δ_{ice}, δ_w, and T_w changes</i>	31
4. UPDATE OF PROCESS MODELING TO GUIDE COMPARISONS	33
5. PLIO-PLEISTOCENE SYNTHESIS AND DEEPER-TIME COMPARISONS	36
5.1. <i>Initial Plio-Pleistocene comparisons on published chronologies</i>	36
5.2. <i>Plio-Pleistocene fine-tuning and synthesis</i>	39
5.3. <i>Deeper-time comparisons and sensitivity tests</i>	42
6. DISCUSSION	47
6.1. <i>Uncertainty assessment</i>	47
6.2. <i>The EOT conundrum</i>	50
6.3. <i>Middle Miocene changes</i>	52
6.4. <i>Stepping down into Northern Hemisphere glaciation</i>	54
6.5. <i>A 40-Myr synthesis</i>	56
7. CONCLUSIONS	58
Acknowledgements	62
Data Availability Statement	62
SUPPLEMENT	64
REFERENCES	66

Plain Language Summary

Global ice volume (hence, sea level) and deep-sea temperature are important measures of Earth's climatic state. To better understand Earth's climate cycles in response to its orbitally driven insolation cycles, we evaluate and synthesize evidence for ice-volume (sea-level) and deep-sea temperature variations at multi-centennial to millennial resolution throughout the last 40 million years. These last 40 million years encompass the major build-up of Antarctic glaciation from about 34 million years ago, and development of extensive Northern Hemisphere ice sheets from about 3.4 million years ago. We present a new template synthesis of ice-volume (sea-level) and deep-sea temperature for the past 5.3 million years, with extension through the interval between 5.3 and 40 Ma with wider uncertainties. We also highlight a number of remaining questions about major climate transitions, including the early glaciation history of Antarctica, the end of the so-called Middle Miocene Climate Optimum from about ~14.5 Ma, and the descent over the past several million years into conditions with extensive ice-age maxima in both hemispheres.

ABSTRACT

Global ice volume (sea level) and deep-sea temperature are key measures of Earth's climatic state. We synthesize evidence for multi-centennial to millennial ice-volume and deep-sea temperature variations over the past 40 million years, which encompass the early glaciation of Antarctica at ~34 million years ago (Ma), the end of the Middle Miocene Climate Optimum, and the descent into bipolar glaciation from ~3.4 Ma. We compare different sea-level and deep-water temperature reconstructions to build a resource for validating long-term numerical model-based approaches. We present: (a) a new template synthesis of ice-volume and deep-sea temperature variations for the past 5.3 million years; (b) an extended template for the interval between 5.3 and 40 Ma; and (c) a discussion of uncertainties and limitations. We highlight key issues associated with glacial state changes in the geological record from 40 Ma to present that require attention in further research. These include offsets between calibration-sensitive versus thermodynamically guided deep-sea paleothermometry proxy measurements; a conundrum related to the magnitudes of sea-level and deep-sea temperature change at the Eocene-Oligocene transition at 34 Ma; a discrepancy in deep-sea temperature levels during the Middle Miocene; and a hitherto unquantified non-linear reduction of glacial deep-sea temperatures through the past 3.4 million years toward a near-freezing deep-sea temperature asymptote, while sea level stepped down in a more uniform manner. Uncertainties in proxy-based reconstructions hinder further distinction of "reality" among reconstructions. It seems more promising to further narrow this using three-dimensional ice-sheet models with realistic ice-climate-ocean-topography-lithosphere coupling, as computational capacities improve.

1. INTRODUCTION

Understanding ice-volume (sea-level) and deep-sea temperature variations over the past 40 million years is important for many lines of research. For example, it will lead to (a) a better understanding of ice sheet (in-)stability under different climate conditions, with implications for sea-level responses to anthropogenic warming (e.g., [Umgiesser et al., 2011](#); [Foster and Rohling, 2013](#); [Rohling et al., 2013b](#); [Pollard et al., 2015](#); [Clark et al., 2016](#); [DeConto and Pollard, 2016](#); [Bamber et al., 2019](#); [Gornitz et al., 2019](#); [Gasson and Keisling, 2020](#); [Gomez et al., 2020](#); [Lear et al., 2020](#); [DeConto et al., 2021](#)). Sea level records, together with deep-sea temperature records, are also essential for (b) improving insights into the processes involved in changing Earth's long-term climate state (e.g., [DeConto and Pollard, 2003](#); [Katz et al., 2008](#); [Foster and Rohling, 2013](#); [De Vleeschouwer et al., 2017](#); [Miller et al., 2020](#); [Westerhold et al., 2020](#); [Boettner et al., 2021](#); [Rohling et al., 2021](#)); and (c) assessing whether, and to what extent, Earth's climate sensitivity to radiative forcing changes depended on the initial climate state, with relevance for anthropogenic climate change (e.g., [Hansen et al., 2007, 2008](#); [Köhler et al., 2010](#); [Masson-Delmotte et al., 2010](#); [PALAEOSENS, 2012](#); [Rohling et al., 2012, 2018](#); [von der Heydt et al., 2016](#); [Stap et al., 2018](#)). Finally, enhanced understanding of sea-level change supports: (d) quantification of coastal stability related to vertical crustal movements, including the influences of mantle dynamic topography and glacio-isostatic adjustments (for references, see [section 2](#)); and (e) improved determination of the drivers of past biogeographic and paleo-anthropological migration, isolation, and diversification patterns (e.g., [Elias et al., 1996](#); [Gilbert et al., 2003](#); [Fernandes, 2006](#); [Bailey, 2010](#); [Armitage et al., 2011](#); [Abbate and Sagri, 2012](#); [Rohling et al., 2013a](#); [Rolland, 2013](#); [Qi et al., 2014](#); [Molina-Venegas et al., 2015](#); [Lee et al., 2020](#); [Adeleye et al., 2021](#); [Machado et al., 2021](#); [Hill et al., 2022](#); [Hölzchen et al., 2022](#)).

Climate variability on 10^4 to 10^5 -year timescales is dominated by cyclic variations in seasonal and spatial insolation patterns, due to Earth's orbital variations (e.g., [Hays et al., 1976](#); [Imbrie and Imbrie, 1980](#); [Imbrie et al., 1984, 1992, 1993](#); [Pisias et al., 1984](#); [Martinson et al., 1987](#); [Zachos et al., 2001, 2008](#); [Lisiecki and Raymo, 2005](#); [De Vleeschouwer et al., 2017](#); [Miller et al., 2020](#); [Westerhold et al., 2020](#)). Beside carbon-cycle changes, ice-volume and ocean-temperature variations are dominant “slow” feedback and response processes in these cycles (e.g., [Hansen et al., 2007, 2008](#); [Köhler et al., 2010](#); [Masson-Delmotte et al.,](#)

2010; Rohling et al., 2012, 2018; PALAEOSENS, 2012). The long, high-frequency variability-suppressing, integration timescales of global ice-volume and deep-sea temperature changes allow time series of these variables to provide in-depth insights into Earth's global climate state adjustments on timescales of several thousands of years and longer.

Building on foundational work by Urey (1947, 1953), McCrea (1950), Epstein et al. (1951), Emiliani (1955), Olausson (1965), and Shackleton (1967), it is well established that changes in the oxygen isotope composition ($\delta^{18}\text{O}$, in per mil; ‰) of marine carbonates reflect a combination of changes in sea-water $\delta^{18}\text{O}$ and temperature (Figure 1). Here, $\delta^{18}\text{O} = 1000 \times (^{18}\text{O}/^{16}\text{O}_{\text{sample}} - ^{18}\text{O}/^{16}\text{O}_{\text{reference}}) / (^{18}\text{O}/^{16}\text{O}_{\text{reference}})$. Since that pioneering work, $\delta^{18}\text{O}$ analyses have become a vital tool for studying Cenozoic climate change (the last 66 million years). Notably, studies that focus on carbonate $\delta^{18}\text{O}$ of well-preserved benthic (sea-floor-dwelling) foraminifera from the deep sea have provided insights into changes in global ice volume (local hydrological gradients are largely averaged out) and deep-sea temperature, which can then be deconvolved (e.g., Shackleton and Opdyke, 1973; Miller et al., 1987, 2005, 2011, 2020; Zachos et al., 2001, 2008; Bintanja and van de Wal., 2008; Lisiecki and Raymo, 2005; de Boer et al., 2010, 2013, 2017; Waelbroeck et al., 2002; Elderfield et al., 2012; Bates et al., 2014; Spratt and Lisiecki, 2016; Ford and Raymo, 2019; Berends et al., 2019, 2021; Jakob et al., 2020; Westerhold et al., 2020; Rohling et al., 2021). Although smaller influences exist (green in Figure 1), they are commonly reduced by studying longer (1000-y) time scales, by restricting analysis to a single species per record (hence, aiming for a single habitat type with no large respiratory CO_2 or $[\text{CO}_3^{2-}]$ variations), and by controlling for life stage (ontogeny) by analyzing specimens in narrow size ranges. Thus, deconvolution almost exclusively concerns the two dominant components: $\Delta\delta_c = \Delta\delta_{(T_w)} + \Delta\delta_w$, where $\Delta\delta_c$ is the relative change in primary deep-sea benthic foraminiferal carbonate δ_c measurements from sediment cores, $\Delta\delta_{(T_w)}$ is the component of δ_c change related to deep-sea temperature (T_w) changes due to temperature-dependent water-to-carbonate oxygen isotope fractionation, and $\Delta\delta_w$ is the ice-volume-related change in mean sea-water $\delta^{18}\text{O}$ (δ_w). The $\Delta\delta_{(T_w)}$ component relates to isotopic equilibrium fractionation (a function of temperature) in the reaction $\text{Ca}^{2+} + 2\text{HCO}_3^- \rightleftharpoons \text{CaCO}_3 + \text{CO}_2 + \text{H}_2\text{O}$. The equilibrium fractionation factor between calcite and water was first determined systematically by O'Neil et al. (1969), with a minor adjustment proposed by Harmon and Schwarcz (1981). Kim and O'Neil (1997) further

refined the relationship, finding that the $\delta^{18}\text{O}$ change with temperature is more pronounced at low temperatures (about $-0.25 \text{ ‰ } ^\circ\text{C}^{-1}$ temperature increase) than at higher temperatures (about $-0.2 \text{ ‰ } ^\circ\text{C}^{-1}$). For deep-sea temperatures, we here use $-0.25 \text{ ‰ } ^\circ\text{C}^{-1}$.

Mean ocean temperature is dominated by the vast deep sea. For example, today's global mean ocean temperature is $\sim 3.5^\circ\text{C}$ (Pawlowicz, 2013), mean surface water temperature is $\sim 16.5^\circ\text{C}$ (<https://www.ncdc.noaa.gov/sotc/global/202108>), and mean *in-situ* deep-sea temperature is $\sim 1\text{--}2^\circ\text{C}$ (Emery, 2001; Pawlowicz, 2013), which includes the component of pressure-related deep-sea warming (it is what a thermometer would measure). Oceanographers often remove the pressure-related component when reporting temperature (and density) structure in the oceans; they report so-called potential temperature, which is depth independent. Paleoceanographic studies determine deep-sea temperature using tools that rely on thermodynamic stable isotope fractionation or trace element partitioning in microfossil carbonates from the seafloor, which provide a measure of *in situ* temperature. For the common depth range of the open ocean, the difference between *in situ* and potential temperature is typically $< 0.5^\circ\text{C}$. For brevity, paleoceanographers commonly omit the term "*in situ*" when referring to deep-sea temperature. Temperature in the ocean interior is a conservative property that (beside the depth-related pressure influence) changes only as a result of ocean circulation and mixing, and temperature adjustments in the vast ocean interior, thus, span multi-centennial to millennial timescales governed by ocean circulation rates. Deep-sea temperature is set by water temperatures in deep-water formation regions, so the near-surface sea-water freezing temperature (about -1.9°C) in deep-water formation regions represents an asymptote to deep-sea cooling (for illustration, see [section 5.3](#)). Accounting for pressure-related warming (Pawlowicz, 2013), this implies a mean deep-sea temperature asymptote at about -1.4 to -1.7°C ; which, in turn, implies a maximum limit to deep-sea cooling of 2.4 to 3.7°C relative to present. Given that global mean ocean temperature during the last glacial maximum (LGM) was $2.57 \pm 0.24^\circ\text{C}$ lower than today (Bereiter et al., 2018), it is evident that LGM deep-sea temperatures approached the freezing asymptote.

The mass of continental ice that does not displace seawater today has a sea-level equivalent volume (m_{seq}) of 65.1 m ; that is, if it all melted, global mean sea level would rise by 65.1 m . Continental ice exists mainly in the Antarctic Ice Sheet (AIS; $57.8 \text{ m}_{\text{seq}}$) and Greenland Ice

Sheet (GrIS; 7.3 m_{seq}) ([Winnick and Caves, 2015](#)). The AIS has two parts; the West Antarctic Ice Sheet (WAIS; ~4.5 m_{seq}) and the much larger East Antarctic Ice Sheet (EAIS; 53.3 m_{seq}). We report first-decimal-point sea-level accuracy to maintain consistency with previous work, even though there will be influences of thermosteric (thermal expansion) and halosteric (saline contraction) effects, and from our assumption of essentially modern (invariant) bathymetry and topography.

Continental ice sheets wax and wane as the net balance varies between mass accumulation (mainly snowfall) and loss through melting, ablation, and calving into the sea. Large ice sheets grow over thousands to tens of thousands of years (with occasional multi-centennial steps), and experience major decay over multi-centennial to multi-millennial timescales, which is reflected in high-resolution sea-level records (e.g., [Fairbanks, 1989](#); [Bard et al., 1990a, 1990b](#); [Hanebuth et al., 2000, 2009](#); [Yokoyama et al., 2000, 2018](#); [Lambeck and Chappell, 2001](#); [Chappell, 2002](#); [Cutler et al., 2003](#); [Siddall et al., 2003, 2008a, 2008b, 2010](#); [Rohling et al., 2004, 2009, 2019, 2021](#); [Arz et al., 2007](#); [Clark et al., 2009](#); [Carlson, 2011](#); [Stanford et al., 2011](#); [Carlson and Clark, 2012](#); [Grant et al., 2012, 2014](#); [Bates et al., 2014](#); [Lambeck et al., 2014](#); [Webster et al., 2018](#); [Ishiwa et al., 2019](#)). Continental ice sheets store large quantities of highly ¹⁸O-depleted water, relative to ¹⁶O, due to Rayleigh distillation during atmospheric vapor transport from evaporation sites to high-latitude precipitation sites (e.g., [Dansgaard, 1964](#); [Garlick, 1974](#); see overview in [Rohling and Cooke, 1999](#)), which leaves the ocean relatively enriched in ¹⁸O ([Figure 2](#)). Consequently, mean global sea-water $\delta^{18}\text{O}$ (δ_w) increases with increasing ice volume and, thus, sea-level lowering. For more detail on $\delta^{18}\text{O}$ fundamentals, see [Rohling and Cooke \(1999\)](#).

Here we assess ice-volume (sea-level) and deep-sea temperature variations on orbital timescales over the past 40 million years. We compare and contrast sea-level and deep-water temperature reconstructions that are fundamentally grounded in data, and we discuss common signals, differences, and uncertainties. We limit this review to data-based reconstructions because they are essential for validating modeling-only approaches. Fully coupled climate-system models cannot yet simulate multi-million-year timescales, but will eventually require independent datasets for model tuning, parameterization, and validation.

We synthesize ice-volume (sea-level) and deep-sea temperature records for the Plio-Pleistocene (i.e., since 5.3 million years ago, Ma), resolved in 1,000-year time steps. We also

present an extension of a single record back to 40 Ma, in 1,000-year time steps. We discuss limitations and uncertainties in the methods evaluated, we explore the robustness of the reconstructions using sensitivity tests, and we compare records to seek to resolve uncertainties and/or to propose future research avenues. Finally, we highlight new insights from the synthesis about emerging trends and patterns, in terms of Earth's long-term climate evolution, particularly during changes between climate states.

2. DEFINITIONS AND APPROACH

Sea level is most intuitively measured in near-coastal settings. However, changing tides, barometric pressure changes, ocean currents, and regional sea-water temperature and salinity (e.g., those related to El Niño–La Niña fluctuations, or the Indian Ocean Dipole) impose regional water-level changes on daily to interannual timescales even if global mean sea level (GMSL) is constant. GMSL represents a time-mean state that is long enough to eliminate the effects of such meteorological variations (Gregory et al., 2019). To further complicate matters, the land-surface base level can change in addition to sea level. Sea-level reconstructions on geological timescales average out daily to interannual variability—but they must account for vertical seabed level and lithospheric changes (i.e., vertical crust and solid upper mantle movements).

Regionally variable upward and downward seabed and/or lithosphere movements can result from, for example, (a) sediment accumulation and compaction; (b) tectonic movements; (c) postglacial rebound in and around variable ice masses and (un-)loading effects due to sea-water mass variations over shelves and the deep sea floor, which are commonly considered under the term glacio-isostatic adjustment (GIA); and (d) long-term mantle-density and mantle-flow related changes known as “dynamic topography”. Thus, at any coastal location, observed sea-level variations are referred to as relative sea-level (RSL) changes. Corrections for various lithospheric and/or sea-bed movement types are needed to translate observed RSL changes into GMSL changes, which commonly also account for gravitational and rotational impacts of large (ice-sheet) mass changes on Earth's surface (e.g., Clark et al., 1978; Nakiblogu and Lambeck, 1980; Nakada and Lambeck, 1987; Peltier, 1988, 1994, 1998, 2004; Mitrovica and Peltier, 1991; Milne and Mitrovica, 1998, 2008;

Lambeck and Chappell, 2001; Mitrovica et al., 2001; Mitrovica and Milne, 2003; Peltier and Fairbanks, 2006; Moucha et al., 2008; Vermeersen and Schotman, 2009; Braun, 2010; Gomez et al., 2010a, 2010b; Raymo et al., 2011; Tamisea and Mitrovica, 2011, Lambeck et al., 2011, 2014; Rowley et al., 2013; Rovere et al., 2014; Peltier et al., 2015; Austermann et al., 2017; Ferrier et al., 2017; Whitehouse, 2018; Gregory et al., 2019; Kuchar et al., 2020; Mitrovica et al., 2020; Yokoyama and Purcell, 2021). Such corrections carry uncertainties because of the choice of model and model parameters used (e.g., Milne and Mitrovica, 2008; Raymo et al., 2011; Grant et al., 2014; Rohling et al., 2017; Whitehouse, 2018; Dumitru et al., 2019, 2021; Kuchar et al., 2020; Peak et al., 2022). For example, Braun (2010) stated that: “mantle dynamics remain poorly constrained, but by linking mantle flow to surface topography, and the evolution of this dynamic topography through time, we obtain a means of using the geological record to constrain the dynamics and viscosity of the mantle and the density structure that controls its flow,” which effectively proposes that instead of attempting to correct observations (such as RSL), “the goal would be to directly invert geological observations to constrain the Earth’s mantle dynamics through time.” This is one among many approaches for studying lithosphere-asthenosphere dynamics, with major uncertainties apparent among methods (Rychert et al., 2020). Regarding GIA corrections from RSL into GMSL, a complication arises from the fact that uncertain past spatial ice-mass distributions during glacial maxima have considerable impacts on the corrections that apply during subsequent interglacials (e.g., Rohling et al., 2017; Dendy et al., 2017). For example, assuming an LGM ice distribution for older glacials is inappropriate (e.g., Rohling et al., 2017; Dendy et al., 2017). Translation of RSL into GMSL, therefore, carries substantial uncertainties. Regardless, the slow nature of isostatic (order 10^4 to 10^5 years) and dynamic and tectonic topography (order 10^5 to 10^6 years) changes allows RSL records to be used with confidence to identify rapid sea-level movements (Supplementary Figure S1), which allows ages from these well-dated records to be transferred to rapid changes in benthic $\delta^{18}\text{O}$ records.

On geological timescales, such as the past 40 million years considered here, GMSL changes are dominated by continental ice-volume variations, which account for variability between about +65 m in an ice-free world and about –130 m during a major bi-polar glacial maximum, relative to present sea level (e.g., de Boer et al., 2010; Miller et al., 2020; Rohling

et al., 2017, 2021; and references therein). Thermosteric influences on sea-level change occurred over a ~10 °C mean deep-sea temperature range over the past 40 million years, which only accounts for less than 7 m of this total (Hieronymus, 2019). Long-term seafloor spreading variations affect spreading-ridge and, thus, ocean-basin volume, and so can also influence sea level (Conrad, 2013), but are not considered here because total seafloor production and spreading rates have remained relatively steady over the 40-Myr timescale investigated (Gernon et al., 2021; and references therein) (Figure 3). Regarding the influence of continental ice-volume variations on GMSL, we note that GMSL only reflects changes in the continental ice volume that does not displace seawater. GMSL does not reflect changes in continental ice volume that displaces seawater, such as floating ice shelves and ice grounded below sea level in basins that would otherwise be filled with seawater. Offsets between GMSL changes and total continental ice-volume changes can, thus, amount to 15% during glacial maxima (Broecker et al., 1975; Polyak et al., 2001; Jakobsson et al., 2008, 2010, 2016; Niessen et al., 2013; Rohling et al., 2017; Goelzer et al., 2020; and references therein).

Variations in total continental ice volume are one of the key “slow” feedbacks in the energy balance of Earth’s climate in response to external climate forcing—predominantly orbital forcing (e.g., Hays et al., 1976; Imbrie and Imbrie, 1980; Imbrie et al., 1984, 1992, 1993; Piasias et al., 1984; Martinson et al., 1987; Zachos et al., 2001, 2008; Lisiecki and Raymo, 2005; De Vleeschouwer et al., 2017; Miller et al., 2020; Westerhold et al., 2020)—along with carbon cycle changes that determine greenhouse gas variations (e.g., Hansen et al., 2007, 2008; Köhler et al., 2010; Masson-Delmotte et al., 2010; PALAEOSSENS, 2012; Rohling et al., 2012, 2018). Global ice-volume variations predominantly exert this influence via the role of ice-sheet surface area in the reflectivity of Earth’s surface to incoming short-wave radiation at high latitudes; the ice-albedo effect. For an illustration of the spatio-temporal distribution of the annual mean radiative impact of this effect over the past 500,000 years, see the distribution after Loutre et al. (2004), modified in Rohling et al. (2012) to include “baseline” interglacial albedo following Fasullo and Trenberth (2008) with superimposed ice-albedo adjustments following Broccoli (2000), Manabe and Broccoli (1985), and Broccoli and Manabe (1987). Note that “slow” in “slow feedback” is a relative categorization given that certain mechanisms can substantially accelerate ice-volume changes to centennial (or even

shorter) timescales, such as a positive feedback loop of melt-back to lower, warmer elevations that drives further melt (e.g., [Levermann and Winkelmann, 2016](#)) or ice-shelf-collapse related processes ([Pollard et al., 2015](#); [deConto and Pollard, 2016](#)). With specific focus on processes that are accelerating mass loss in the Greenland ice sheet to centennial and even decadal timescales, [Box et al. \(2022\)](#) listed: “*tidewater glacier acceleration and destabilization by submarine melting* ([Truffer and Fahnestock, 2007](#); [Khazendar et al., 2019a,b](#); [Wood et al., 2021](#)); *loss of floating ice shelves* ([Mouginot et al., 2015](#)); *accelerating interior motion from increased melt and rainfall* ([Doyle et al., 2015](#)); *enhanced basal thawing due to hydraulically released latent heat and viscous warming* ([Phillips et al., 2010](#)); *amplified surface melt run-off due to bio-albedo darkening* ([Stibal et al., 2017](#)); and *impermeable firn layers* ([MacFerrin et al., 2019](#)) amplified by ice-sheet surface hypsometry ([Mikkelsen et al., 2016](#); [van As et al., 2017](#)).” In West Antarctica, sea-floor data indicate sustained pulses of very rapid Thwaites Glacier retreat (>2 km per day) within the past two centuries that are related to tidally modulated grounding-line migration ([Graham et al., 2022](#)).

To understand past climate changes in relation to changes in the radiative balance of climate, it is of interest to directly reconstruct total continental ice volume, rather than sea-level-based reconstructions that can underestimate total continental ice volume by up to ~15%. Direct total continental ice-volume reconstructions can be obtained in different ways from deep-sea $\delta^{18}\text{O}$ records measured on the carbonate shells of sea-floor dwelling (benthic) foraminifera; many such reconstructions in addition provide insight into deep-sea temperature variations ([Shackleton and Opdyke, 1973](#); [Miller et al., 1987, 2005, 2011, 2020](#); [Zachos et al., 2001, 2008](#); [Bintanja and van de Wal., 2008](#); [Lisiecki and Raymo, 2005](#); [de Boer et al., 2010, 2013, 2017](#); [Waelbroeck et al., 2002](#); [Elderfield et al., 2012](#); [Bates et al., 2014](#); [Spratt and Lisiecki, 2016](#); [Ford and Raymo, 2019](#); [Berends et al., 2019, 2021](#); [Jakob et al., 2020](#); [Westerhold et al., 2020](#); [Rohling et al., 2021](#)).

Since the $\delta^{18}\text{O}$ method was pioneered ([Urey, 1947, 1953](#); [McCrea, 1950](#); [Epstein et al., 1951](#); [Emiliani, 1955](#); [Olausson, 1965](#); [Shackleton, 1967](#)), benthic $\delta^{18}\text{O}$ records have been developed for many hundreds of sediment cores on a global scale. Carefully selected records have been compiled into so-called “stacks” or “megasplices” that cover many millions of years in a continuous manner, at millennial-scale resolution (e.g., [Imbrie et al.,](#)

1984; Martinson et al., 1987; Miller et al., 1987, 2001, 2020; Bassinot et al., 1994; Zachos et al., 2001, 2008; Karner et al., 2002; Lisiecki and Raymo, 2005; De Vleeschouwer et al., 2017; Westerhold et al., 2020). Here we use two leading recent benthic $\delta^{18}\text{O}$ records (Lisiecki and Raymo, 2005; Westerhold et al., 2020) to deconvolve ice-volume and deep-sea temperature change. Our assessment assumes that Earth's surface water $\delta^{18}\text{O}$ has remained constant (i.e., a steady-state balance exists between $\delta^{18}\text{O}$ exchange impacts of seafloor hydrothermal activity and surface weathering) over the past 40 million years, which is supported by reconstructed sea-water $\delta^{18}\text{O}$ stability over the past 500 million years (Ryb and Eiler, 2018).

Chronologies for benthic $\delta^{18}\text{O}$ stacks and splices are obtained from diverse techniques, starting with relatively low-resolution constraints from biostratigraphy and magnetic polarity stratigraphy, with refinement by tuning—in different ways—of variability in studied records to Earth's orbital variability, which is the central driver of the climate cycles of interest (e.g., Hays et al., 1976; Berger, 1978; Imbrie and Imbrie, 1980; Imbrie et al., 1984, 1992, 1993; Martinson et al., 1987; Berger and Loutre, 1991, 1992; Laskar et al., 1993, 2004, 2011; Lisiecki and Raymo, 2005; De Vleeschouwer et al., 2017; Miller et al., 2020; Westerhold et al., 2020). Total uncertainty ranges of resultant chronologies reduce from ~40 thousand years (kyr) at around 5 Ma, to ~4 kyr in the last million years (Lisiecki and Raymo, 2005).

Given our emphasis on orbital-timescale variability over 40 million years, we focus primarily on total ice-volume (V_{ice} , reported in meters sea-level equivalent, m_{seq}) and deep-sea temperature (T_w) inferred from deep-sea carbonate-shelled benthic foraminiferal $\delta^{18}\text{O}$ records (hereafter, δ_c). As a central thread in our assessment, to guide comparison between methods over different timescales, we use the deconvolution approach of Rohling et al. (2021) (Figures 4, 5) on the Lisiecki and Raymo (2005) and Westerhold et al. (2020) records, starting with these records on their original chronologies. We then harmonize the chronologies and add fine-tuning using radiometrically constrained ages for major transitions. In this method, a constrained polynomial regression-based conversion is used between δ_c and GMSL (Figure 6a, after Spratt and Lisiecki, 2016), followed by a new process modeling approach to approximate the growth and decay histories of the four dominant ice sheets over the past 40 million years: AIS, GrIS, the North American Laurentide Ice Sheet complex (LIS), and the Eurasian Ice Sheet complex (EIS), along with their $\delta^{18}\text{O}_{\text{ice}}$ (δ_{ice})

characteristics, and their imposed sea-water $\delta^{18}\text{O}_{\text{water}}$ (δ_w) changes (Rohling et al., 2021). The sum of imposed δ_w changes for all ice sheets is then subtracted from deep-sea δ_c changes (Lisiecki and Raymo, 2005; Westerhold et al., 2020) to yield $\delta^{18}\text{O}$ residuals that reflect water-to-carbonate oxygen isotope fractionation changes due to *in-situ* deep-water temperature variations (Figure 5c). For more detail, see section 3.7.

The method of Rohling et al. (2021) accounts quantitatively for all major interdependences between ice volume, δ_{ice} , δ_w , δ_c , and T_w , so it provides a useful framework for comparison and validation across these parameters (Rohling et al., 2021). This multi-parameter validation potential underlies our use of this method as the central thread against which to compare results from other approaches. Moreover, multi-parameter validation (especially when including organic paleothermometry methods from likely deep-water formation regions; e.g., Hutchinson et al., 2021) can also reveal potential impacts of alteration (drift) of the original δ_c and other shell-chemical signatures as a result of diagenetic recrystallization (Raymo et al., 2018). This is because such post-depositional chemical alterations depend on sedimentary fluid advection-diffusion, with different gradients and reaction rates for different elements, so that post-depositional reactions are unlikely to remain within the bounds of mutually consistent variations in the deconvolution model, and because organic methods would not be affected by these carbonate-specific processes (Rohling et al., 2021).

Comparisons can be made with RSL data from different archives, such as (a) fossil corals and near-coastal cave deposits (e.g., Veeh and Veevers, 1970; Edwards et al., 1987, 1993, 1997; Fairbanks, 1989; Bard et al., 1990a, 1990b, 1991; 1996a, 1996b, 2010; Chen et al., 1991; Hamelin et al., 1991; Dia et al., 1992, 1997; Stein et al., 1993; Eisenhauer et al., 1993, 1996; Zhu et al., 1993; Gallup et al., 1994, 2002; Stirling et al., 1995, 1998, 2001; Chappell et al., 1996; Colonna et al., 1996; Galewsky et al., 1996; Ludwig et al., 1996; Stirling, 1996; Camoin et al., 1997, 2004; Toscano and Lundberg, 1998; Esat et al., 1999; Hearty et al., 1999, 2007; Israelson and Wohlfarth, 1999; Sherman et al., 1999; Vezina et al., 1999; Blanchon and Eisenhauer, 2000; Fruijtier et al., 2000; Walter et al., 2000; Camoin et al., 2001, 2004; Lambeck and Chappell, 2001; Yokoyama et al., 2001a, 2018; Blanchon et al., 2002; Cutler et al., 2002, 2003, 2004; Hearty, 2002; Muhs et al., 2002a, 2002b, 2006; 2011, 2012a, 2012b; Multer et al., 2002; Zhao and Yu, 2002; Chappell, 2002; Cabioch et al., 2003, 2008; Cutler et al., 2003, 2004; Thompson et al., 2003, 2011; Potter et al., 2004; Speed and Cheng, 2004;

Chiu et al., 2005; Fairbanks et al., 2005; Mortlock et al., 2005; Sun et al., 2005; Thompson and Goldstein, 2005; Ayling et al., 2006; Collins et al., 2006; Frank et al., 2006; Peltier and Fairbanks, 2006; Riker-Coleman et al., 2006; Coyne et al., 2007; Zazo et al., 2007; Andersen et al., 2008, 2010; McCulloch and Mortimer, 2008; O’Leary et al., 2008a, 2008b, 2013; Blanchon et al., 2009; Clark et al., 2009; Thomas et al., 2009, 2012; Dorale et al., 2010; McMurty et al., 2010; Carlson, 2011; Stanford et al., 2011; Carlson and Clark, 2012; Descamps et al., 2012; Kennedy et al., 2012; Lewis et al., 2012; Toscano et al., 2012; Medina-Elizalde, 2013; Moseley et al., 2013; Lambeck et al., 2014; Dutton et al., 2015; Abdul et al., 2016; Hibbert et al., 2016, 2018; Leonard et al., 2016; Wainer et al., 2017; Webster et al., 2018; Yokoyama et al., 2018; Ishiwa et al., 2019; Dumitru et al., 2019, 2021); (b) stratigraphically virtually continuous records from the relatively well-dated (Red Sea and Mediterranean Sea) marginal basin sea-level methods, which rely on water residence-time calculations that depend on the depth of the shallow straits that form a gateway between these basins and the open ocean (Figure 7) (Rohling et al., 1998; Siddall et al., 2003, 2004; Biton et al., 2008; Rohling et al., 2009, 2014; Grant et al., 2012, 2014; Yokoyama and Purcell, 2021); and (c) sediment-sequence based RSL information (e.g., Rabineau et al., 2006; Kominz et al., 2008, 2016; Naish and Wilson, 2009; Grant et al., 2019). However, there are issues with such comparisons. Coral and cave-deposit estimates represent RSL at single dated points in time and space and, therefore, generally offer relatively limited long-term stratigraphic continuity. Coral data are also typically limited by relatively short temporal coverage over just two or three glacial cycles (~350,000 years), and can suffer from habitat-depth uncertainties and region-specific environmental impacts (e.g., Woodroffe and Webster, 2014; Braithwaite, 2016; Hibbert et al., 2016, 2018; Rohling et al., 2017, 2019). Finally, all RSL methods require corrections for vertical land movements due to tectonic, GIA, and dynamic topography effects (e.g., Milne and Mitrovica, 2008; Rovere et al., 2014; Austermann et al., 2017; Mitrovica et al., 2020; Peak et al., 2022). Regardless, comparison of RSL records with ice-volume (or GMSL) records remains valuable, even without crustal movement corrections, because of the independent age control of various RSL records on rapid transitions. Corals and cave deposits are dated directly with radiometric methods (radiocarbon and/or U-series). The chronology of the Red Sea record is radiometrically constrained through signal correlation with radiometrically dated cave records (Grant et al., 2012, 2014). The Mediterranean record is radiometrically constrained through radiocarbon

dating, tephrochronology, and correlation with nearby cave records, with further chronostratigraphic constraints from a well-known relationship between Mediterranean humid events and precession minima (Lourens et al., 1996, 2001; Grant et al., 2012; Larrasoaña et al., 2013; Rohling et al., 2014, 2015, 2017; Konijnendijk et al., 2014; Satow et al., 2015; Grant et al., 2016, 2017). Here, we mainly use well-dated RSL reconstructions to verify and refine chronological control of ice-volume (or GMSL) records, rather than for their sea-level information. Long-term “drift” in the Mediterranean record to anomalously high RSL values before ~1.5 Ma (Rohling et al., 2014; 2021) means that we only use the last 150,000 years of the Mediterranean record for SE Aegean Sea core LC21, where the chronology is tightly constrained by a combination of radiocarbon dating, tephrochronology, and oxygen isotope correlation between core LC21 and Soreq Cave, Israel (Grant et al., 2012; Rohling et al., 2014, 2017). As a special case for the Middle and Late Pliocene, cave-deposit-based RSL benchmarks from Mallorca are used because they have been both radiometrically dated and meticulously corrected for all known vertical land movement sources, including GIA and tectonic or dynamic topography-related changes (Dumitru et al., 2019, 2021). Similar work for Early Pliocene coastal deposits in Patagonia suggests that GMSL stood at 28.4 ± 11.7 m (1σ) at 4.69–5.23 Ma (Rovere et al., 2020). Such corrected benchmarks provide unique validation criteria for continuous ice-volume (GMSL) reconstructions through that time interval.

Finally, we acknowledge a plethora of other RSL reconstruction methods from coral microatolls, salt-marsh and mud-flat deposits, coastal deposits and drowned coastlines, and structures such as Roman fishtanks (e.g., van de Plassche, 1986; Gehrels, 1994, 2000; Yokoyama et al., 2000, 2001b, 2006; Hanebuth et al., 2000, 2009; Gehrels et al., 2001; Sivan et al., 2001, 2004, 2016; Shennan and Horton, 2002; Kienast et al., 2003; Woodroffe and Horton, 2005; Barry et al., 2008; Dabrio et al., 2011; Kemp et al., 2011; Engelhart and Horton, 2012; Lewis et al., 2013; Ishiwa et al., 2015; Shennan et al., 2015; Khan et al., 2017; Meltzner et al., 2017; Hallmann et al., 2018; Hibbert et al., 2018; Dutton et al., 2021; and references therein). We do not include these methods because of their typically limited temporal coverage through (mainly) the last 20,000 years, and occasionally further back to the last interglacial. Regardless, these methods have provided valuable and often precise RSL information that sets a broader context to the long-term methods discussed here.

414

415 3. LONG-TERM ICE-VOLUME OR SEA-LEVEL RECORDS

416 In this section, we discuss the main approaches for determining long-term (near-)
417 continuous sea-level variability and in most cases also *in situ* deep-water temperature
418 variability, in roughly chronological order of development. In [section 3.1](#), we discuss direct
419 scaling of δ_c records to sea-level records; the focus in [section 3.2](#) is on statistical
420 deconvolutions of δ_c records, while that in [section 3.3](#) is on assessment of paired δ_c and
421 independent paleothermometry measurements. In [section 3.4](#), we present the marginal sea
422 residence-time method, while the focus in [section 3.5](#) is on statistically generalized sea-level
423 reconstruction from diverse input records. In the final two sections, two hybrid data-
424 modeling philosophies are discussed: inverse modeling approaches are discussed in [section](#)
425 [3.6](#) and a new process modeling method is highlighted in [section 3.7](#).

426 Fundamentally, all methods discussed below—except for the marginal seas approach
427 ([section 3.4](#))—rely on deep-sea δ_c time series that span hundreds of thousands or millions of
428 years, using $\Delta\delta_c = \Delta\delta_{(Tw)} + \Delta\delta_w$. Here, $\Delta\delta_w$ reflects ice-volume changes because continental
429 ice preferentially stores the lighter isotope (^{16}O) over the heavier isotope (^{18}O) ([Figure 2](#)).
430 This implies that there should be a useful relationship between δ_w changes and z_{SL} changes
431 (here termed the $\Delta\delta_w:\Delta z_{SL}$ relationship), where Δz_{SL} is the total sea-level (ice-volume)
432 change in m_{seq} . Almost all studies use linear approximations for this relationship (i.e.,
433 $\Delta\delta_w:\Delta z_{SL}$ is treated as a constant). Comparison between $\delta^{18}\text{O}$ changes in fossil carbonate and
434 coral-based sea-level variations led to early suggestions that $\Delta\delta_w:\Delta z_{SL}$ is $0.012 \pm 0.002 \text{ ‰}$
435 m^{-1} ([Fairbanks and Matthews, 1978](#); [Aharon, 1983](#); [Chappell and Shackleton, 1986](#); [Labeyrie](#)
436 [et al., 1987](#); [Shackleton, 1987](#); [Fairbanks, 1989](#)). More recent work compared deep-sea
437 sediment porewater δ_w measurements with sea-level constraints and inferred a value of
438 $0.009 \pm 0.001 \text{ ‰ } m^{-1}$ ([Schrag et al., 1996](#); [Adkins et al., 2002](#)), although re-evaluation of the
439 porewater method has indicated wider uncertainties ([Miller et al., 2015](#)). [Raymo et al.](#)
440 [\(2018\)](#) report a $0.008\text{--}0.011 \text{ ‰ } m^{-1}$ range from the literature and then selected a single
441 preferred value of $0.011 \text{ ‰ } m^{-1}$. In contrast, [Waelbroeck et al. \(2002\)](#) argued for a value of
442 $0.0085 \text{ ‰ } m^{-1}$, and [Miller et al. \(2020\)](#) used $0.013 \text{ ‰ } m^{-1}$ based on ice-sheet endmember
443 δ_{ice} calculations ([Winnick and Caves, 2015](#)), but both studies emphasized that individual ice-

sheet δ_{ice} and associated global mean δ_{ice} changes should be modeled (e.g., Cuffey, 2000; Lhomme, 2004; Lhomme et al., 2005). This was explored over the last 40 million years by Rohling et al. (2021), who used it to quantify distinct $\Delta\delta_w:\Delta z_{SL}$ non-linearity (section 3.7). The marginal sea residence-time method (e.g., Rohling et al., 1998, 2009; 2014; Rohling, 1999; Fenton et al., 2000; Siddall et al., 2003, 2004; section 3.4) is fundamentally different in that it relies on amplified change in basin sea-water $\delta^{18}O$ (and salinity) due to water residence-time changes in response to water exchange restriction through shallow straits that connect the basins with the open ocean (Figure 7). This method mostly uses planktonic foraminiferal carbonate analyses, but can also consider fine-fraction carbonate, or benthic foraminiferal carbonate, and resolves RSL at the connecting straits.

3.1. Scaling of δ_c records to sea-level

In early work, direct scale comparisons were made between carbonate $\delta^{18}O$ and sea-level measurements based on giant clams in fossil coral reef complexes, with allowance for temperature influences (Aharon, 1983). In modern terms, the sea-level values considered were approximately RSL after correction for tectonic land movements; what was viewed as tectonic change was possibly at least partly due to GIA and/or dynamic topography. Chappell and Shackleton (1986) compared sea-level data with deep-sea benthic δ_c because much smaller temperature variations are expected in the cold deep sea, which results in a better signal-to-noise ratio than can be obtained from surface waters. They further concentrated on deep Pacific δ_c because it had already been inferred that Atlantic deep waters had undergone larger glacial-interglacial temperature fluctuations than Pacific and Indian Ocean deep waters (Duplessy et al., 1980). The sea-level values considered by Chappell and Shackleton (1986) were what we now know as RSL after correction for tectonic land movements; it is again possible that what was viewed as tectonic change was at least partly due to GIA and/or dynamic topography. Chappell and Shackleton (1986) determined a $\Delta\delta_w:\Delta z_{SL}$ value of 0.0097‰ m^{-1} from their comparisons, and also inferred that glacial deep Pacific temperatures were on average about 1.5 °C , and up to a potential maximum of 2.5 °C , lower than today. This landmark result effectively represents the first deconvolution of $\Delta\delta_c$ into both its $\Delta\delta_w$ and $\Delta\delta_{(Tw)}$ components; this estimate has stood the test of time. Similar

glacial deep-sea cooling values have been derived from meticulous inter-ocean $\Delta\delta_c$ comparisons (Labeyrie et al., 1987). Estimates from later paleothermometry proxies only slightly adjusted Last Glacial Maximum deep-sea cooling estimates to 2-3 °C relative to the Holocene (e.g., Martin et al., 2002; see section 3.3), which has been contested (Skinner and Shackleton, 2005), but agrees well with the $2.57 \pm 0.24^\circ\text{C}$ LGM global ocean cooling determined using noble gases trapped in ice cores (Bereiter et al., 2018).

Cutler et al. (2003) directly compared coral-based RSL data (after tectonic movement correction) with Atlantic and Pacific δ_c records over the last 140,000 years, and derived glacial deep-sea cooling. They found that peak interglacials stand out as brief “top-hat shaped” warm anomalies in an otherwise roughly 2 °C colder deep ocean with much more muted variability. Arz et al. (2007) undertook a similar direct scaling, but used a benthic δ_c record of the past 80 kyr from the northern Red Sea (under two different temperature assumptions) and coral-based RSL data of Fairbanks (1989), Chappell (2002), Cutler et al. (2003), and Thompson and Goldstein (2005). Finally, the combined work of Naish et al. (2009) and Miller et al. (2012) related RSL from near-coastal sediment-sequence stratigraphy to δ_c between about 3.3 and 2.3 Ma to provide a highly resolved record of relative sea-level variability for that time interval.

3.2. Statistical deconvolution of ice-volume and deep-sea temperature impacts on δ_c

Along with direct scaling between δ_c changes and sea-level estimates (section 3.1), more nuanced statistics-driven comparisons have been made. Such statistically guided $\Delta\delta_c$ deconvolution into $\Delta\delta_w$ and $\Delta\delta_{(Tw)}$ has employed a range of methods, starting with a comparison of different regressions between δ_c and coastal sea-level benchmarks for different ocean basins, and separated between intervals of glaciation and deglaciation, over 430,000 years (Waelbroeck et al., 2002). Waelbroeck et al. (2002) used RSL data in their regressions (Bard et al., 1990a, 1990b, 1996a; Stein et al., 1993; Zhu et al., 1993; Gallup et al., 1994; Stirling et al., 1995; Chappell et al., 1996; Hanebuth et al., 2000; Yokoyama et al., 2000) based on the argument that “... rather than RSL, ... ice-volume equivalent sea level ... should be used. However, because the two are approximately proportional to each other for sites far from the former ice sheets, we have used ... RSL estimates” (Waelbroeck et al.,

2002). Similar arguments have been made by Siddall et al. (2010) and Stanford et al. (2011). While such direct use of RSL is a rough approximation, the alternative—full GIA and dynamic topography corrections—would also carry substantial uncertainties, especially for older benchmarks and regions with relatively limited knowledge of the geophysical context (section 2). Hence, pragmatic choices are made that reflect a balance between the accuracy, precision, and “signal-to-noise” ratios needed. The tectonic histories and uplift/subsidence corrections of the coral sites used in these approaches are complex (cf. Creveling et al., 2015), which may imply larger uncertainties than those considered previously.

Siddall et al. (2010) further developed the Waelbroeck et al. (2002) approach to span the past 5 million years, and used sea-level and ice-volume information from a wider range of methods (Oerlemans and Van der Veen, 1984; Fairbanks, 1989; Bard et al., 1990c, 2002; Stirling et al., 1998; Bamber et al., 2001; Lythe et al., 2001; Chappell, 2002; Cutler et al., 2003; Siddall et al., 2003, 2008b; Antonioli et al., 2004, 2007; Schellmann and Radtke, 2004; Thompson and Goldstein, 2006; Yokoyama et al., 2000). Regarding the RSL versus GMSL issue, Siddall et al. (2010) stated: “Where we use bench-mark sea-level indicators such as fossil coral reefs or submerged speleothem records, we only discuss sites distant from the former ice-sheet margins, which can be considered to represent [GMSL] to within several (i.e. typically < 2–3) meters (Bassett et al., 2005). Note that there is inadequate data and understanding of isostatic processes during this interval to be more exact.” While Waelbroeck et al. (2002) fitted non-linear regressions through δ_c and sea-level data, Siddall et al. (2010) used piece-wise linear interpolation of δ_c between sea-level markers. Next, the reconstructed sea-level variability (Δz_{SL}) was translated into $\Delta \delta_w$, the ice-volume related component of change in $\Delta \delta_c$, using a constant $\Delta \delta_w : \Delta z_{SL}$ value of $0.0085 \text{ } \text{‰} \text{ m}^{-1}$, which revealed the deep-sea temperature component based on $\Delta \delta_{(TW)} = \Delta \delta_c - \Delta \delta_w$. From this analysis, Siddall et al. (2010) inferred that glacial-interglacial T_w variations were of the order of $2 \pm 1 \text{ } ^\circ\text{C}$ over the past 5 million years (reported as a range, which we consider here as equivalent to a 95% confidence interval). Moreover, they found that the observation of Cutler et al. (2003)—that deep-sea temperature is consistently cold with muted variability, punctuated by sharp warm anomalies associated with peak interglacials—applied throughout the last 700,000 years.

Bates et al (2014) used largely the same approach as Siddall et al. (2010) but added last interglacial sea-level information from the compilation of Kopp et al. (2009), and considered a wider global array of deep-sea δ_c records. They found that the typically used transfer functions are not stable before the onset of the Mid Pleistocene Transition (MPT) at ~ 1.25 Ma. The modern type of glacial-interglacial deep-water circulation response developed during the MPT, which limits the usefulness of post-MPT transfer functions to pre-MPT records. Bates et al (2014) reported that Late Pleistocene glacial-interglacial T_w changes were about 2 ± 1 °C throughout the deep Pacific, Indian, and South Atlantic Ocean basins, but up to 3 ± 2 °C in the North Atlantic Ocean.

A final class of attempts to scale δ_c with ice volume should be mentioned that uses tropical surface planktonic foraminiferal records. The underlying assumption is that tropical surface temperatures might have varied even less than deep-sea temperatures (Matthews and Poore, 1980; Matthews, 1984; Prentice and Matthews, 1988). This hypothesis of invariant tropical surface temperature has since been rejected (e.g., Liu and Herbert, 2004; Lawrence et al., 2006; Etourneau et al. 2010; Li et al., 2011); we therefore do not discuss records from this method further.

3.3. Paired δ_c and Mg/Ca or clumped isotope-based temperature measurements

Deep-sea temperature reconstruction from independent paleothermometry measurements can be used to constrain $\Delta\delta_{(Tw)}$, which then isolates the $\Delta\delta_w$ component. Ideally, analyses would be based on an aliquot of the same microfossils used to measure δ_c variations: $\Delta\delta_c$. However, for geochemical reasons when working with benthic foraminifera, it is common to use infaunal species (that live within the sediment) for Mg/Ca and epifaunal species (that live atop the sediment) for δ_c from the same sample. Benthic foraminiferal Mg/Ca paleothermometry has long been used for this purpose (e.g., Martin et al., 2002; Lear et al., 2004; Sosdian and Rosenthal, 2009; Elderfield et al., 2012; Jakob et al., 2020), while clumped isotope (Δ_{47}) paleothermometry on benthic foraminifera is a more recent development (e.g., Modestou et al., 2020). Following temperature corrections, the “paired δ_c and paleothermometry” method commonly applies *a-priori* assumption-driven conversion of sea-water oxygen isotope residuals into sea-level-equivalent ice-volume

records (e.g., Lear et al., 2004; Sosdian and Rosenthal, 2009; Elderfield et al., 2012; Jakob et al., 2020). This sounds straightforward, but there are complications.

The most frequently used Mg/Ca temperature proxy (a proxy is an indirect measurement approximation) relies on empirical calibration of results for modern sediment samples using *in-situ* temperatures of overlying waters (e.g., Lear et al., 2002; Martin et al., 2002; Marchitto & deMenocal, 2003; Yu & Elderfield, 2008; Marchitto et al., 2007; Elderfield et al., 2010; Weldeab et al., 2016; Hasenfratz et al., 2017; Barrientos et al., 2018). These studies reveal specific calibrations for different benthic foraminiferal taxa, which can diverge considerably, but most are nonlinear with flat (insensitive) T_w profiles at typical low deep-sea temperatures. This causes considerable reconstructed T_w uncertainty of order ± 1 to 1.5 $^{\circ}\text{C}$ (1σ), which causes uncertainty of ± 0.25 to 0.38 ‰ in reconstructed δ_w variations that typically imply ± 20 to 30 m reconstructed sea-level uncertainties (Raymo et al., 2018).

Benthic Mg/Ca results may also be affected by varying deep-sea carbonate-ion concentrations (Elderfield et al., 1996; Yu and Elderfield, 2008; Yu & Broecker, 2010). Furthermore, complications from oceanic Mg- and Ca-concentration changes over timescales greater than multiple millions of years (e.g., Griffith et al., 2008; Coggon et al., 2010; Cramer et al. 2011; Evans and Müller, 2012; Evans et al., 2018; Lebrato et al., 2020, Modestou et al., 2020) may cause mean shifts to higher or lower calibrated values and a change in the relationship between Mg/Ca and T_w (Evans and Müller, 2012). Miller et al. (2020) used a 2-Myr smoothed Mg/Ca-based paleotemperature synthesis that accounted for such biases (Cramer et al., 2011) to deconvolve their δ_c splice over the past 66 million years. Miller et al. (2020) applied these “*long-term paleotemperature estimates to kyr-scale sampled δ_c records to interrogate sea-level change primarily on [... Myr- and shorter time scales]*.” They then extensively compared their inferred sea-level record with RSL records (Miller et al., 2005, 2011; Kominz et al., 2016) after making corrections for dynamic topography (Rowley et al., 2013). Using a smoothed long-term Mg/Ca paleotemperature record to make $\Delta\delta_{(T_w)}$ corrections means that a proportion of $\Delta\delta_{(T_w)}$ may remain uncorrected from shorter (orbital) δ_c variations; effectively, any $\Delta\delta_{(T_w)}$ portion below or above the long-term mean would remain and would be interpreted erroneously as a $\Delta\delta_w$ (ice-volume) component. Miller et al. (2020) detected and transparently discussed this issue in the form of negative $\Delta\delta_w$ anomalies in interglacial warm periods (low ice-volume anomalies; almost

reaching an ice-free state). They did not discuss similar potential anomalies in older intervals, but instead focussed on Myr-scale variability that is much less affected by this issue.

Clumped isotope (Δ_{47}) paleothermometry is less reliant on empirical calibration and is guided more by thermodynamic principles (e.g., Ghosh et al., 2006; Eiler, 2007; Eiler, 2011). The Δ_{47} relates the abundance of ^{13}C - ^{18}O bonds in the calcite lattice to the temperature at which the calcite precipitates (Eiler, 2007). The method does not require information on seawater chemistry in which the foraminifera calcified (Eiler, 2011), and similar changes between inorganic and organic carbonates indicate an absence of major vital (metabolic fractionation) effects (e.g., Tripathi et al., 2010; Grauel et al., 2013; Kele et al., 2015; Bonifacie et al., 2017; Rodríguez-Sanz et al., 2017; Peral et al., 2018; Piasecki et al., 2019; Meinicke et al., 2020). The sensitivity of the Δ_{47} proxy is only $\sim 0.003 \text{ ‰ } ^\circ\text{C}^{-1}$ (Kele et al., 2015), so high measurement precision and multiple measurement replications are needed (Rodríguez-Sanz et al., 2017). Until recently, this required larger sample sizes than is feasible with foraminifera, yet recent developments are overcoming this limitation (Schmid and Bernasconi, 2010; Bernasconi et al., 2011; Grauel et al., 2013; Hu et al., 2014; Müller et al., 2017), especially when combined with targeted statistical assessment of signal and noise distinction (Rodríguez-Sanz et al., 2017; Modestou et al., 2020). Regardless, state-of-the-art reconstruction uncertainties remain at least 2-3 $^\circ\text{C}$ (95% confidence interval) (Rodríguez-Sanz et al., 2017; Modestou et al., 2020).

Once δ_w variations are calculated (with uncertainties) from paired δ_c and paleotemperature measurements, sea-water oxygen isotope residuals can be converted into ice-volume estimates. It is relevant that deep-sea δ_w is much less sensitive to temporal atmospheric poleward vapor flux and thermohaline overturn variations than tropical δ_w , due to the much larger volume of the deep-sea relative to the warm surface layers (Mix, 1992). As mentioned above, conversion of deep-sea δ_w into ice-volume estimates is conventionally done using constant (linear) $\Delta\delta_w:\Delta z_{\text{SL}}$ approximations with values within the 0.008-0.014 ‰ m^{-1} range (e.g., Aharon, 1983; Labeyrie et al., 1987; Shackleton, 1987; Fairbanks, 1989; Schrag et al., 1996; Adkins et al., 2002; Waelbroeck et al., 2002; Siddall et al., 2010; Miller et al., 2015; Raymo et al., 2018; Jakob et al., 2020; Miller et al., 2020). The ubiquitous reliance on constant $\Delta\delta_w:\Delta z_{\text{SL}}$ approximations is unexpected given that the expectation from first

principles is that it should be nonlinear (Rohling et al., 2021). This is because the mean δ_{ice} of individual ice sheets changes with size and time (e.g., Aharon, 1983; Mix and Ruddiman, 1984; Chappell and Shackleton, 1986; Rohling and Cooke, 1999; Waelbroeck et al., 2002; Rohling et al., 2021), and because different ice sheets with different isotopic fractionation grow at different rates at different times (Rohling et al., 2021). Some studies have tried to accommodate nonlinearity by considering ranges for the $\Delta\delta_w:\Delta z_{SL}$ relationship; e.g., Jakob et al. (2020) considered a $\Delta\delta_w:\Delta z_{SL}$ range of 0.008-0.014 ‰ m⁻¹, with a “best estimate” of 0.011 ‰ m⁻¹. Waelbroeck et al. (2002) used a constant $\Delta\delta_w:\Delta z_{SL}$ value of 0.0085 ‰ m⁻¹, while Miller et al. (2020) used 0.013 ‰ m⁻¹, but both called for modeling of the $\Delta\delta_w:\Delta z_{SL}$ relationship, which follows in section 3.6.

Some studies apply deconvolutions based on simple assumptions informed by previous paleothermometry-based results. For example, Dumitru et al. (2019) simply applied a straightforward $\Delta\delta_c$ to ice-volume scaling by assuming that 75% of the signal is driven by ice volume, with the remaining 25% driven by temperature variations, arguing that this is consistent with Pleistocene Mg/Ca-based ocean temperature estimates (Elderfield et al., 2012; Miller et al., 2012). They also assumed a scaling of 0.011 ‰ m⁻¹ GMSL rise, after Naish et al. (2009) and Raymo et al. (2018). Instead, Hansen et al. (2008) argued that equal contributions of $\Delta\delta_w$ and $\Delta\delta_{(Tw)}$ to $\Delta\delta_c$ provide a good fit with observations, although this was later adjusted to account for a reducing temperature portion as freezing conditions are approached, and reciprocal change in the ice-volume portion (Hansen et al., 2013). The Hansen et al. (2013) reconstruction used two linear segments with a 2/3 versus 1/3 contribution of the temperature contribution to $\Delta\delta_c$ between times with δ_c larger than present and smaller than present, respectively, and the opposite for the ice-volume portion. Such assumption-driven approaches may be sufficient for first-order approximations, but process-based deconvolution is needed to obtain more representative results (sections 3.6. and 3.7).

3.4. The marginal sea residence-time method

The marginal sea method of sea-level reconstruction derives from work that documented and quantified amplified signals of, especially, glacial-interglacial $\delta^{18}O$ change and monsoon-

driven low-salinity events in the Mediterranean Sea (e.g., [Rossignol-Strick et al., 1982](#); [Rossignol-Strick., 1983, 1985, 1987](#); [Vergnaud-Grazzini, 1985](#); [Rohling and Bryden, 1994](#); [Rohling et al., 1994a, 2004, 2014, 2015](#); [Rohling, 1999](#); [Amies et al., 2019](#)) and glacial-interglacial $\delta^{18}\text{O}$ and salinity changes in the Red Sea ([Locke and Thunell, 1988](#); [Thunell et al., 1988](#); [Rohling, 1994b](#); [Hemleben et al., 1996](#); [Rohling and Bigg, 1998](#); [Rohling et al., 1998](#); [Fenton et al., 2000](#); [Siddall et al., 2003, 2004](#); [Biton et al., 2008](#)). Signal amplification in marginal seas is related to limited water-mass exchange with the open ocean through shallow connecting straits; the limiting sill depth is 137 m at Hanish Sill, Bab-el-Mandab passage, southern Red Sea ([Werner and Lange, 1975](#); [Rohling et al., 1998](#); [Fenton et al., 2000](#); [Siddall et al., 2002, 2003, 2004](#); [Lambeck et al., 2011](#)), and 284 m at the Camarinal Sill, Gibraltar Strait, western Mediterranean Sea ([Bryden and Kinder, 1991](#); [Bryden et al., 1994](#); [Matthiessen and Haines, 2003](#); [Naranjo et al., 2017](#)) ([Figure 7](#)). In both basins, water exchange through the strait is constrained hydraulically by the strait dimensions and the density contrast between waters inside and outside of the strait ([Bryden and Kinder, 1991](#); [Bryden et al., 1994](#); [Smeed, 1997, 2000](#); [Siddall et al., 2002, 2003, 2004](#)). This imposes a considerable water residence time within the basin (of order 10^2 years), where it is exposed to strong net evaporation ($\sim 0.6 \text{ m y}^{-1}$ for the Mediterranean, and $\sim 2 \text{ m y}^{-1}$ for the Red Sea). At lower sea levels, the sill passage becomes even more restricted, as does the water exchange, which extends the residence time of water within the basin and, thus, its duration of exposure to forcing. As a result, both salinity and sea-water $\delta^{18}\text{O}$ increase rapidly with sea-level lowering (note that the two properties change non-linearly relative to each other because freshwater terms all have zero salinity but a range of $\delta^{18}\text{O}$ values—e.g., [Rohling and Bryden, 1994](#); [Rohling et al., 1998, 2014](#); [Rohling, 1999](#); [Rohling and Bigg, 1998](#); [Siddall et al., 2003, 2004](#); [Matthiessen and Haines, 2003](#); [Biton et al., 2008](#); [Figure 7](#)).

The limiting factors in the marginal-sea sea-level method are depth and cross-sectional area of the shallowest sill within the connecting strait, so the reconstructed records are RSL for the sill location; GIA, tectonics, and dynamic topography can further affect results ([Siddall et al., 2003, 2004](#); [Grant et al., 2012, 2014](#); [Rohling et al., 2014](#)). Recent GIA reconstructions with three-dimensional Earth models suggest smaller departures from GMSL at the Bab-el-Mandab Strait than previous GIA reconstructions with one-dimensional Earth models, but

also indicate the potential existence of substantial time-lags between GMSL change and maximum GIA response (Peak et al., 2022).

The less restricted Mediterranean Sea has a glacial-interglacial sea-water $\delta^{18}\text{O}$ contrast that is about 2× amplified relative to the 1‰ open ocean value, while the highly restricted Red Sea has a 4-5× signal amplification. This has an impact on the importance of temperature uncertainties in the marginal-sea records. Especially in the Red Sea, and to a lesser extent the Mediterranean, sea-water $\delta^{18}\text{O}$ signal amplification increases signal-to-noise ratios when deriving sea-level variations from microfossil carbonate $\delta^{18}\text{O}$ records; that is, temperature uncertainty impacts are suppressed strongly, relative to open ocean studies. Moreover, warmer conditions cause stronger evaporation, and stronger shifts to more positive sea-water $\delta^{18}\text{O}$ values, which offsets the tendency toward more negative values due to water-to-carbonate $\delta^{18}\text{O}$ fractionation under warmer conditions. Hence, the marginal-sea sea-level method is much more robust to temperature uncertainties than open ocean reconstructions (Siddall et al., 2003, 2004; Rohling et al., 1999, 2014). This is especially the case in the Red Sea, which is much more restricted and has a much simpler hydrology than the Mediterranean. In the Red Sea method, generous temperature uncertainties ($\pm 2^\circ\text{C}$) imply a sea-level uncertainty of only ± 4 m, while large ($\pm 40\%$) changes in the basin-averaged net evaporation add ± 5 m and relative humidity uncertainties another ± 2 m; all at 2σ (Siddall et al., 2004). Hence, it makes little difference which carbonate phase is analyzed from Red Sea sediments because the residence-time effect on sea-water $\delta^{18}\text{O}$ greatly dominates variability (Rohling et al., 2009). In the Mediterranean method, RSL uncertainties at a similar level are $\sim\pm 20$ m, and there is much more noise between different carbonate phases (even between mixed-layer and deeper-dwelling foraminiferal species) (Rohling et al., 2014).

No major rivers drain into the Red Sea, and the steep rift-shoulder morphology means that most external rainfall drains away from the basin. Regardless, propagation of generous uncertainties implies that the 2σ sea-level uncertainty for each data point is ± 12 m (see above) (Siddall et al., 2003, 2004). Probabilistic analyses that take into account the stratigraphic context of the records and the total range uncertainty for each sea-level data point determine the mode and median records along with percentile distributions for their probability interval (comparable to a standard error of a mean), with 95% probability limits

of, on average, ± 6 m for the general Red Sea stack and no strict stratigraphic coherence between points (Grant et al., 2012, 2014), and ± 2.5 m when focusing on specific records from strictly consecutive sample series (Rohling et al., 2019). The Red Sea method is limited in time by the maximum age of available in-tact sedimentary sequences, which currently is ~ 550 ka (Rohling et al. 2009). Seismic data indicate considerable promise for extending the record by coring with advanced penetration techniques (Mitchell et al., 2015).

The Mediterranean receives much more fresh water from external watersheds than the Red Sea. This substantially complicates sea-level reconstructions based on Mediterranean microfossil carbonate $\delta^{18}\text{O}$ records. Especially African monsoon maxima during (precession-driven) Northern Hemisphere insolation maxima cause negative carbonate $\delta^{18}\text{O}$ anomalies that had to be omitted from the record before sea-level calculation (Rohling et al., 2014, 2017). While this successfully removed 100+ intervals, three anomalies were left (yellow bands in Figures 1 and 2 of Rohling et al., 2014). Moreover, Mediterranean sea-level estimates from the marginal sea method deviate considerably from other reconstructions before ~ 1.5 Ma (Rohling et al., 2014, 2021; Dumitru et al., 2019, 2021; Berends et al., 2021a). The Mediterranean method is evidently affected by secular change, which most likely reflects a “baseline shift in Mediterranean climate conditions from a warm/moist state to a warm/arid state at ~ 1.5 Ma” (Rohling et al., 2014). Hence, while the Mediterranean record extends back to ~ 5.3 Ma, when the current Strait of Gibraltar opened (e.g., Amarathunga et al., 2022; and references therein), there are continuity (thus, interpolation) and secular offset issues. We avoid these issues here by only using the Mediterranean RSL reconstruction for age information about major sea-level transitions within the last 150,000 years, based on data from core LC21, which has a particularly detailed chronology (Grant et al., 2012; Rohling et al., 2014).

3.5. Statistically generalized sea-level records from diverse suites of input records

Spratt and Lisiecki (2016) presented a sea-level reconstruction for the last 800,000 years based on principal component analysis of the combined information from 7 archives: (1) a South Pacific Mg/Ca-corrected benthic δ_w record from 3,290 m water depth (Elderfield et al., 2012); (2) a North Atlantic Mg/Ca-corrected benthic δ_w record from 3,427 m water

depth (Sosdian and Rosenthal, 2009); (3) a detrended first principal component of 34 Mg/Ca-temperature-corrected and 15 alkenone-temperature-corrected surface-water δ_w records (Shakun et al., 2015); (4) the statistical benthic δ_c scaling to RSL benchmarks of Waelbroeck et al. (2002); (5) the inverse model-based δ_c deconvolution of Bintanja et al. (2005) but not its more recent versions (Bintanja and van de Wal, 2008; de Boer et al., 2010, 2013, 2014; Berends et al., 2021a; see section 3.6); (6) the Mediterranean marginal sea record (Rohling et al., 2014); (7) the Red Sea marginal sea record (Siddall et al., 2003, 2004; Rohling et al., 2009), although not its latest generation (Grant et al., 2014). Spratt and Lisiecki (2016) considered a linear $\Delta\delta_w:\Delta z_{SL}$ conversion of 0.009 ‰ m⁻¹, arguing against use of higher values with the caveat that the value may change with “changes in the mean isotopic content of each ice sheet (Bintanja et al., 2005) and their relative sizes.” The Spratt and Lisiecki (2016) sea-level record is a useful synthesis of sea-level variability over the past 800,000 years, but it does not help (yet) to develop a better understanding of sea-level and deep-sea temperature (co)variations during past warm climates. The method could be updated using the latest-generation records for the past 800,000 years. It would also be particularly useful for the approach to be extended further back in time as more records emerge.

3.6. Inverse modeling

Inverse modeling is used to deconvolve ice-volume and deep-sea temperature impacts on carbonate oxygen isotope data, using one-dimensional (1D) or 3D ice models (e.g., Bintanja et al., 2005; Bintanja and van de Wal, 2008; de Boer et al., 2013, 2017; Berends et al., 2019, 2021a). Bintanja and van de Wal (2008) summarized the method as: “an inverse technique in conjunction with an ice-sheet model coupled to a simple deep-water temperature model.” The model is hemispheric; it simulates Northern Hemisphere ice sheets (excluding GrIS) only, using a 3D ice sheet-ice shelf-bedrock model that resolves ice thickness, ice temperature, and bedrock elevation, driven by air temperature variations. Stable oxygen isotope changes of ice are resolved by calculating both the isotopic content of precipitation and ice flow (Bintanja and van de Wal, 2008), which then allows calculation of $\Delta\delta_w$. They applied this method to the δ_c stack of Lisiecki and Raymo (2005) to “reconstruct mutually consistent 3-Myr time series of surface air temperature (continental and annual mean

778 *between 40° and 80° N), ice-sheet volume, and sea level.*” Core to the method is a derivation
 779 of continental mean Northern Hemisphere temperature through observation-constrained
 780 modeling that linearly relates the temperature (relative to present) to the difference
 781 between modeled and observed benthic δ_c over a centennial time step (Bintanja et al.,
 782 2005; Bintanja and van de Wal, 2008; de Boer et al., 2010).

783 De Boer et al. (2010) presented a set of 1D ice sheet models to extend the approach back to
 784 35 million years ago—using the δ_c records of Lisiecki and Raymo (2005) and Zachos et al.
 785 (2008)—and found good agreement with the 3D results of Bintanja and van de Wal (2008)
 786 over the last 3 million years (average Northern Hemisphere temperature and sea-level
 787 differences of 1°C and 6.2 m). De Boer et al. (2010) use this 1D method to resolve five
 788 hypothetical ice sheets: LIS, EIS, GrIS, WAIS, and EAIS, with ice flow over initially cone-
 789 shaped continental surfaces, and including bedrock adjustment to ice loading based on the
 790 principle of local isostatic equilibrium. The procedure for LIS and EIS relies on a similar
 791 Northern Hemisphere temperature assumption as used by Bintanja et al. (2005), and
 792 Bintanja and van de Wal (2008). For Antarctica and Greenland, however, de Boer et al.
 793 (2010) introduced difference factors (δT_{NH}) relative to the Northern Hemisphere
 794 temperature, which were then used to tune volume changes in those ice sheets so that a
 795 strong EAIS volume increase was found around the Eocene–Oligocene Transition (EOT), with
 796 simultaneous initiation of GrIS with LIS and EIS at the onset of Northern Hemisphere
 797 glaciation. A striking and testable suggestion from de Boer et al. (2010) is that $\Delta\delta_{(Tw)}$ was the
 798 major (~70%) contributor to $\Delta\delta_c$ between ~13 and ~3 Ma. During this interval, the modeled
 799 EAIS reached its maximum extent, which would limit the ice-volume ($\Delta\delta_w$) contribution to
 800 $\Delta\delta_c$. From ~3 Ma, ice volume gained importance again as Northern Hemisphere ice sheets
 801 developed. As a result, the de Boer et al. (2010) sea-level reconstruction has a flat and
 802 invariant segment between ~13 and ~3 Ma that hardly extends to >10 m above present-day
 803 sea level. Observational studies tend to suggest a more variable AIS (e.g., Harwood and
 804 Webb, 1990; Webb and Harwood, 1991; Wilson, 1995; Naish et al., 2009; Miller et al., 2012;
 805 Grant et al., 2019; Jakob et al., 2020). Moreover, subsequent modeling developments have
 806 improved the representation of ice flow, grounding-line dynamics and ice-ocean
 807 interactions, which allow for larger AIS variability during this period, including enhanced
 808 EAIS retreat during the Pliocene (Pollard et al., 2015) and Miocene (Gasson et al., 2016).

Subsequent work returned to 3D ice-sheet modeling, including Antarctica, using the coupled ANICE 3D ice-sheet-shelf model (de Boer et al., 2013, 2014, 2017; Berends et al., 2018, 2019, 2021a). These studies extended back to 5.0 Ma (de Boer et al., 2014) or 3.6 Ma in the most recent study (Berends et al., 2021a). Note that Berends et al. (2018, 2019, 2021a) included climate forcing from General Circulation Models, rather than the previously used simple temperature offsets; this fundamentally changed the inverse method from predicting sea-level to temperature relationships to predicting sea-level to CO₂ relationships. Berends et al. (2021a) compared their results with the reconstructions of Willeit et al. (2019). The Willeit et al. (2019) reconstruction is entirely model-based, so we do not consider it here (as explained in [section 1](#)). For comparison of that study with the methods discussed here, see Berends et al. (2021a), who reported good agreement through the major Pleistocene ice ages, but significant deviations during the warmer-than-present Pliocene. Berends et al. (2021a) attributed this to the fact that the Willeit et al. (2019) model only simulated the Northern Hemisphere, and arbitrarily assumed that the Antarctic sea-level contribution is 10% of that of northern ice sheets.

The linear relationship assumed in the inverse modeling approach between deep-sea δ_c (through temperature) and Northern Hemisphere high-latitude temperature seems to be at odds with consistently low deep-sea temperature with muted variability, punctuated by sharp warm anomalies at peak interglacials (Cutler et al., 2003; Elderfield et al., 2012; Siddall et al., 2010; Bates et al., 2014; Rohling et al., 2021). This Late Pleistocene signal structure in deep-sea temperature is more reminiscent of Antarctic ice-core and southern high-latitude temperature time series than Greenland, North Atlantic, or North Pacific temperature time series (e.g., Rohling et al., 2012, 2021; Rodrigues et al., 2017; Hasenfratz et al., 2019; Lee et al., 2021), with similar or shorter time scale variations over the last glacial cycle (Anderson et al., 2021). It is striking that this dominance of southern high-latitude variability in global deep-sea temperature variations is so apparent in the Late Pleistocene, when ice-ages were distinctly dominated by Northern Hemisphere ice-sheet waxing and waning. It would only be more pronounced during past warm times, when there was little Northern Hemisphere ice and ice-volume variations occurred only in Antarctica (e.g., Rohling et al. (2021) for hemispheric glaciation contrasts). This suggests that the inverse modeling approach, at least prior to the GCM-based approach of Berends et al. (2018,2019, 2021a), may have been

driven by temperature assumptions that are too Northern Hemisphere-biased, whereas global mean deep-sea temperature instead reflects a global high-latitude variability with strong Southern Hemisphere characteristics.

3.7. Process modeling of ice-volume, δ_{ice} , δ_w , and T_w changes

Process modeling (essentially using a data-informed conceptual model) offers a computationally efficient deconvolution of ice-volume impacts on seawater oxygen isotope ratios, with subsequent deep-sea temperature derivation from residuals between carbonate-based oxygen isotope data and calculated sea-water oxygen isotope changes (e.g., Rohling et al., 2021) (Figure 4). Rohling et al. (2021) first assessed the $\Delta\delta_w:\Delta z_{SL}$ relationship analytically to illustrate that it is fundamentally nonlinear in nature, and to explore its sensitivity to key assumptions and uncertainties. This analytical assessment clearly indicates the underlying complexity of the $\Delta\delta_w:\Delta z_{SL}$ relationship. Rohling et al. (2021) then presented a new process modeling approach that used published sea-level records (Grant et al., 2014; Rohling et al., 2014; Spratt and Lisiecki, 2016) to calculate mutually consistent ice-volume variations through time for four schematic planoconvex lens-shaped ice sheets: AIS, GrIS, LIS, and EIS. This was combined with calculations for each ice sheet of evolving oxygen isotope characteristics with mass-accretion and -loss and, thus, the mean $\delta^{18}O_{ice}$ (δ_{ice}) development for each ice sheet over time, with impacts on δ_w , δ_c , and T_w (compared with measured δ_c records). Next, the δ_c stack and mega-splice of Lisiecki and Raymo (2005) and Westerhold et al. (2020) were deconvolved to obtain reconstructions for the past 5.3 and 40 million years, respectively, with multiple validation criteria from independent observations. We use this approach here as a central thread to guide comparisons among various records.

The first stage in the process modeling deconvolution was a constrained polynomial regression-based conversion between δ_c and GMSL; namely, the $\Delta\delta_c:\Delta z_{SL}$ regression based on Spratt and Lisiecki (2016) with added sensitivity tests (Figures 6a). Here we explore this regression with further sensitivity tests (Figure 6b). Moreover, while we initially follow Rohling et al. (2021) in assuming that this relationship remained constant through time

(within uncertainties), we here also consider markedly different relationships for the Antarctic-dominated portion when $\Delta z_{SL} > 0$ m (see [sections 4, 5.3, and 6.1](#)).

Following the δ_c to GMSL conversion, process modeling is used to estimate growth and decay histories for four dominant ice volumes over the past 40 million years (V_{AIS} , V_{GRIS} , V_{LIS} , and V_{EIS} , in m_{seq}) along with their evolving δ_{ice} characteristics, and the imposed sea-water $\delta^{18}O_{water}$ (δ_w) changes ([Rohling et al., 2021](#)). Finally, the sum of the imposed δ_w changes for all ice sheets was subtracted from deep-sea δ_c changes ([Lisiecki and Raymo, 2005](#); [Westerhold et al., 2020](#)) to yield $\delta^{18}O$ residuals, which reflect water-to-carbonate oxygen isotope fractionation changes due to *in-situ* deep-water temperature variations of -0.25 ‰ $^{\circ}C^{-1}$ at the typically low deep-sea temperatures ([Kim and O’Neil, 1997](#)) ([Figures 4, 5c](#)).

The process modeling method demonstrated distinct hysteresis in mean δ_{ice} development versus individual ice volume ([Figure 8](#)). It also found a distinct nonlinearity in the relationship between changes in sea-water $\delta^{18}O$ and sea level (the $\Delta\delta_w:\Delta z_{SL}$ relationship), which was visually approximated by a fifth-order polynomial: $\Delta\delta_w = 9.6 \times 10^{-11} \Delta z_{SL}^5 + 1.9 \times 10^{-8} \Delta z_{SL}^4 + 2.5 \times 10^{-7} \Delta z_{SL}^3 - 1 \times 10^{-4} \Delta z_{SL}^2 - 0.015 \Delta z_{SL} - 0.133$. The fundamental processes underlying the “tilted gullwing” shape of the relationship are explained in the conceptual analysis of [Rohling et al. \(2021\)](#), who further emphasized that this relationship may be refined by use of growth/decay and Rayleigh distillation transfer functions for individual ice sheets that are based on less idealized ice-sheet growth and $\delta^{18}O$ models. Overall, the reconstructions of [Rohling et al. \(2021\)](#) agree with the observations of [Cutler et al. \(2003\)](#), [Elderfield et al. \(2012\)](#), [Siddall et al. \(2010\)](#), and [Bates et al. \(2014\)](#) that deep-sea temperature was consistently cold with muted variability during glacials, punctuated by sharp warm anomalies during peak interglacials. The reconstructions also agree with the 2.57 ± 0.24 °C global LGM ocean cooling inferred from noble gases trapped in ice cores ([Bereiter et al., 2018](#)), with Pliocene GMSL reconstructions ([Dumitru et al., 2019, 2021](#)), and with several other validation criteria, although discrepancies also exist, especially before ~22 Ma ([Rohling et al., 2021](#)).

Uncertainties in the method are dominated by uncertainty in the $\Delta\delta_c:\Delta z_{SL}$ regression extrapolation beyond the constraints of the Pleistocene data cloud (i.e., to sea levels above ~+10 m relative to present). [Rohling et al. \(2021\)](#) considered an extrapolation constrained to +65.1 m at the ice-free state as their main scenario, and sensitivity tests of: (1) the upper

95% probability limit of the main-case extrapolation, which tops out at ~86 m; and (2) a completely unconstrained extrapolation that tops out at ~50 m as a lower limit. We note that the flattening of the curve toward a high sea-level limit is directly related to the underpinning processes ([section 5.3](#)), and that it is supported by modeling studies, although the limit itself remains uncertain ([Fisher et al., 2018](#)). Here, we consider the same extrapolation limits as [Rohling et al. \(2021\)](#) because, beyond these bounds, unrealistic sea-level reconstructions occur with long-lasting Middle Miocene ice-free periods, or the presence of considerable Eocene ice sheets (equivalent to the modern combined GrIS + WAIS volume), respectively. However, as mentioned above, we also consider a wider range of superimposed uncertainties in our sensitivity tests (see [sections 4, 5.3, and 6.1](#)).

4. UPDATE OF PROCESS MODELING TO GUIDE COMPARISONS

We here use the process modeling approach ([Rohling et al., 2021](#)) as the main framework to support comparison among methods. We (1) make adjustments to the initial $\Delta\delta_c:\Delta z_{SL}$ regression to further explore uncertainties ([Figure 6](#)); (2) correct minor errors in the LIS and GrIS descriptions that caused a slight offset in the balance between the amount of sea-level change and the sum of reconstructed ice volumes (see [Supplement section A](#)); and (3) perform calculations in a probabilistic framework to better understand uncertainty propagation. In the $\Delta\delta_c:\Delta z_{SL}$ regression, extrapolation uncertainty beyond the constraining data cloud was considered comprehensively by [Rohling et al. \(2021\)](#) ([Figure 6a](#)) to which readers are referred for its implications. Here we additionally consider the prediction interval of the $\Delta\delta_c:\Delta z_{SL}$ regression to assess the robustness of the mean regression ([Figure 6b](#)). We, therefore, re-assess the mean regression and its prediction intervals. These prediction intervals are not conventional in a statistical sense, in that “noise” around the mean is not random, but instead consists of highly organized (orbital) cycles around the mean. This is evident when, before regression, filtering is performed on the δ_c and z_{SL} records to retain only Milankovitch (orbital) frequencies and eliminate shorter-period variability; prediction intervals in this case are virtually indistinguishable from those found without removal of sub-Milankovitch variability ([not shown](#)). The prediction intervals,

929 therefore, are measures of the scale of Milankovitch cycles around the long-term, secular
 930 mean, rather than measures of random variability around the regression.

931 We impose one additional constraint on the prediction intervals. Where prediction intervals
 932 normally widen with distance from the mean, here they must converge on a single known
 933 point: a sea level of +65.1 m where Earth enters an ice-free state (this also implies
 934 decreasing amplitudes of ice-volume variation with decreasing global ice volume). Within
 935 these constraints, we determine a “worst-case” noise scenario by converting δ_c records
 936 5,000 times in a Monte Carlo approach into sea level with the mean regression, using
 937 prediction intervals as if they (in the conventional sense) characterize true random scatter.
 938 This Monte Carlo sampling also includes error in the ages, assigned to avoid age reversals
 939 between consecutive data points at 95% probability. The newly sampled records are linearly
 940 interpolated. Next, we apply a series of N bootstrap samplings of sets of 500 sea-level
 941 records with replacement to calculate the median z_{SL} record (50th percentile), along with the
 942 0.5th and 99.5th percentiles to approximate how well the calculated z_{SL} median from the
 943 resampling procedure approximates the input data.

944 Comparison of the z_{SL} median with z_{SL} values calculated (with the main regression; [Figure 6](#))
 945 from the input δ_c data on their original timescale suggests offsets of the order of 1 m. This is
 946 captured adequately by a ± 2 or 3 m 99% probability interval for the median using N = 1000
 947 bootstrap samplings; hence, we use this as a useful interval to represent the uncertainty in
 948 characterizing the z_{SL} median. Note that that this merely marks the probability window
 949 within which the median of our procedure’s solutions is found when accounting for
 950 measurement uncertainties under certain input conditions (mainly the input record, applied
 951 age uncertainties, and $\Delta\delta_c:\Delta z_{SL}$ regression used). We also need a measure of the expected
 952 stochastic spread of values based on addition of new δ_c data; the prediction interval. As
 953 mentioned above, the prediction interval of the $\Delta\delta_c:\Delta z_{SL}$ regression ([Figure 6](#)) cannot be
 954 used for this purpose because it predominantly represents Milankovitch (orbital) variability
 955 around secular changes; it therefore is accounted for by the close match between the input
 956 data and our median Δz_{SL} . However, there is also δ_c uncertainty associated with stacking of
 957 δ_c values, which was calculated in the “Prob-stack” study at an average $1\sigma(\delta_c) = 0.16\%$
 958 across the past 5 million years ([Ahn et al., 2017](#)). Using our main Δz_{SL} regression ([Figure 6](#)),
 959 this translates into an average stochastic uncertainty level of ± 6.5 m at 1σ , or an 95%

confidence interval of about ± 13 m. Hence, the indicative stochastic prediction interval around our z_{SL} median within which 95% of newly added values to the benthic stacks may be expected is on average ± 13 m.

To avoid clutter and because we are interested in long-term median signals, we use our median z_{SL} solutions with the 99% probability intervals of the median as outlined above, along with the further propagation into T_w solutions. Complex non-linear interdependences exist within the closed sum $\Delta\delta_c = \Delta\delta_{(T_w)} + \Delta\delta_w$ (Figures 5d–f); to ensure that we consider median Δz_{SL} uncertainty propagation into ΔT_w uncertainties as conservatively as possible, we identify the T_w uncertainty interval as the interval between $\min(T_w)$ and $\max(T_w)$ across all three T_w values per time step (median and its propagated lower and upper 99% bounds).

Below, we compare our median reconstructions with previous approaches for the past 5.3 million years (Plio-Pleistocene) (Figures 9–15). Thereafter, we compare approaches back to 40 Ma. Finally, we explore potential implications of a different $\Delta\delta_c:\Delta z_{SL}$ relationship than that used by Rohling et al. (2021), especially for the AIS-dominated portion where $\Delta z_{SL} > 0$ m (sections 5.3 and 6.1). Different shapes of the $\Delta\delta_c:\Delta z_{SL}$ relationship may arise due to: (a) different Rayleigh distillation for the early AIS, following a relationship that is more typical of the “warmer” lower-latitude EIS and LIS than the “colder” modern high-latitude AIS and GrIS (Figure 16); (b) changes in subglacial paleotopography/-bathymetry (notably Antarctica over multi-million year timescales) due to erosion and tectonics (Wilson et al., 2012; Paxman et al., 2019; Hochmuth et al., 2020) that changed ice-sheet sensitivity to environmental conditions such as ocean temperature (and likely, therefore, δ_c) (Wilson et al., 2013; Stap et al., 2014; Gasson et al., 2016; Colleoni et al., 2018; Paxman et al., 2020); or (c) ocean gateway/circulation changes (e.g. Kennett, 1977; Sauermilch et al., 2021) and long-term seawater pH changes (e.g. Uchikawa & Zeebe, 2010) that affected ocean temperature (hence, δ_c) or δ_c directly, respectively.

5. PLIO-PLEISTOCENE SYNTHESIS AND DEEPER-TIME COMPARISONS

5.1. Initial Plio-Pleistocene comparisons on published chronologies

The colored double-headed arrows in [Figure 5a](#) indicate the timespans over which we consider comparisons among various records. We first compare records on their published chronologies over the last five glacial cycles ([Figure 9](#)), over the past 800,000 years ([Figure 10](#)), and through the Plio-Pleistocene (last 5.3 million years; [Figure 11](#)). We then present the same figures after “fine-tuning” the chronologies of our ([Rohling et al., 2021](#)) process model deconvolutions of the [Lisiecki and Raymo \(2004\)](#) and [Westerhold et al. \(2020\)](#) δ_c records using more directly dated records ([Figures 12–14](#), respectively). We conclude this section with a synthesis assessment ([Figure 15](#)).

Sea-level changes from our process model deconvolutions of the [Lisiecki and Raymo \(2004\)](#) and [Westerhold et al. \(2020\)](#) δ_c records are compared in [Figure 9a](#) with those of [Bates et al. \(2014; section 3.2\)](#), [Miller et al. \(2020; section 3.3\)](#), [Grant et al. \(2014; section 3.4\)](#), [Rohling et al. \(2014; core LC21 only; section 3.4\)](#), and a suite of RSL data from fossil corals that pass commonly applied age-reliability screening criteria ($\delta^{234}\text{U}_{\text{initial}}$, calcite $\leq 2\%$, and $[\text{}^{232}\text{Th}] \leq 2$ ppb; and $\delta^{234}\text{U}_{\text{initial}} = 147 \pm 5 \text{‰}$ when $0 < \text{age} \leq 17$ ka, $142 \pm 8 \text{‰}$ when $17 < \text{age} \leq 71$ ka, $147 \pm 5 \text{‰}$ when $71 < \text{age} \leq 130$ ka, and $147 + 5/-10 \text{‰}$ when $\text{age} > 130$ ka) ([Hibbert et al., 2016; section 2](#)). The coral data are plotted as elevation, and are tectonically corrected where appropriate (Z_{cp} in [Hibbert et al., 2016](#)), with sea level above this point depending on the paleo water depth of the coral species. As explained above, RSL information from the Red Sea ([Grant et al., 2014](#)), Mediterranean Sea ([Rohling et al., 2014](#)), and corals is used mainly here for chronological guidance. The corals provide a good chronology for the last 40,000 years and for the onset of the penultimate deglaciation at ~ 135 ka. The Mediterranean and Red Sea records provide strong chronologies since ~ 150 ka from combined radiocarbon dating, tephrochronology, and unambiguous signal agreement with radiometrically dated cave deposits in Israel ([Grant et al., 2012, 2014; Rohling et al., 2017](#); and references therein). Before 150 ka and back to 500 ka, the Red Sea chronology is well constrained by correlation of monsoon (dust) variations ([Roberts et al., 2011](#)) with radiometrically dated Chinese cave deposits, along with datings for deglaciations from radiometrically dated volcanic ash layers within river deposits in Italy ([Grant et al., 2014](#)). When plotting process

model deconvolutions of the [Lisiecki and Raymo \(2004\)](#) and [Westerhold et al. \(2020\)](#) δ_c records on their original chronologies ([Figure 9](#)), we observe convincing signal agreements with the RSL records, although key features in the deconvolutions are chronologically offset from corresponding features in the well-dated RSL records. This indicates that chronological fine-tuning is needed, as discussed later ([Figure 12](#)). Deep-sea temperature changes, relative to the present, from our process model deconvolutions of the [Lisiecki and Raymo \(2004\)](#) and [Westerhold et al. \(2020\)](#) δ_c records are compared in [Figure 9b](#) with those of [Bates et al. \(2014\)](#). We also include the estimate of LGM global ocean cooling inferred from noble gases in gas bubbles trapped in ice ([Bereiter et al., 2018](#)).

The [Bates et al. \(2014\)](#) and [Miller et al. \(2020\)](#) records are based on benthic δ_c time series that use a fundamentally similar chronology to the [Lisiecki and Raymo \(2004\)](#) δ_c record. While the [Bates et al. \(2014\)](#) single-site record is noisier than the 57-record stack of [Lisiecki and Raymo \(2004\)](#), both its sea-level and deep-sea temperature signal structures compare well with our process model deconvolutions of the [Lisiecki and Raymo \(2004\)](#) and [Westerhold et al. \(2020\)](#) δ_c records ([Figure 9](#)). Similar arguments hold for the [Miller et al. \(2020\)](#) sea-level record. The [Westerhold et al. \(2020\)](#) record did not aim for the most accurate chronology in this brief interval (it spans 66 million years); as a result, it has temporal offsets although it still has generally similar signal amplitudes and structure. Deep-sea temperature changes from both our process model deconvolutions of the [Lisiecki and Raymo \(2004\)](#) and [Westerhold et al. \(2020\)](#) δ_c records, and from [Bates et al. \(2014\)](#) all indicate generally cold conditions throughout the glacial cycles that are punctuated sharply by warmer intervals during interglacial maxima, especially over the last 450,000 years ([Figure 9b](#)) (see [Cutler et al., 2003](#); [Siddall et al., 2010](#)).

Next, we compare our process model deconvolutions of the [Lisiecki and Raymo \(2004\)](#) and [Westerhold et al. \(2020\)](#) δ_c records over the past 800,000 years for sea level ([Figure 10a](#)) with the [Miller et al. \(2020\)](#) record ([section 3.3](#)), the [Spratt and Lisiecki \(2016\)](#) statistical multi-record assessment ([section 3.5](#)), the [de Boer et al. \(2010\)](#) inverse modeling sea-level record ([section 3.6](#)), and the [Grant et al. \(2014\)](#) Red Sea RSL record ([section 3.7](#)). The overall glacial-interglacial structure is consistent among these records, despite resolution differences and timing offsets. There are also ~10 m amplitude discrepancies that reflect different input records, deconvolution approaches, and sometimes different smoothing

methods. Timing offsets are addressed later (see [Figure 13](#) for a chronologically fine-tuned version of [Figure 10](#) for the process model deconvolutions of the [Lisiecki and Raymo \(2004\)](#) and [Westerhold et al. \(2020\)](#) δ_c records). Deep-sea temperature records from our process model deconvolutions are compared in [Figure 10b](#) with Antarctic (air) temperature variations ([Jouzel et al., 2007](#)), and with LGM global ocean cooling inferred from noble gases in gas bubbles trapped in ice ([Bereiter et al., 2018](#)). There is a strong signal structure agreement over the last 800,000 years covered by the ice-core record, with deep-sea temperature variations scaling almost precisely to 1/4 of Antarctic temperature variability (see also [Rohling et al., 2021](#)), but some timing offsets must be addressed ([Figure 13b](#)).

Our process model deconvolutions of the [Lisiecki and Raymo \(2004\)](#) and [Westerhold et al. \(2020\)](#) δ_c records are compared for the last 5.3 million years in [Figures 11a](#) and [11b](#) with the reconstructions of [Bates et al. \(2014; section 3.2\)](#) and [Miller et al. \(2020; section 3.3\)](#), the inverse modeling results of [Berends et al. \(2021a; section 3.6\)](#), North Atlantic Mg/Ca-based deep-sea temperature and Mg/Ca-temperature-corrected sea-level results ([Jakob et al., 2020; section 3.3](#)), New Zealand sediment-sequence based sea-level amplitude scaling of δ_c records ([Naish et al., 2009; Miller et al., 2012; section 3.1](#)), New Zealand sediment-sequence based middle Pliocene amplitude estimates of RSL variations ([Grant et al., 2019](#)), GMSL estimates from corrected RSL data based on drowning cave deposits in Mallorca ([Dumitru et al., 2019; 2021; section 2](#)), Early Pliocene GMSL estimates from corrected RSL data based on Patagonian intertidal sediments ([Rovere et al., 2020](#)), and the [Bereiter et al. \(2018\)](#) LGM ocean cooling estimate. With the exceptions of the [Jakob et al. \(2020\)](#) sea-level and deep-sea temperature reconstructions, and the [Miller et al. \(2020\)](#) sea-level record, there is a high level of agreement among the records, which span diverse approaches and input data ([Figures 11a, 11b, 14](#)). The [Jakob et al. \(2020\)](#) data have anomalously large amplitudes (1.8× as large as those from other methods). Their deep-sea temperature data are based on Mg/Ca paleothermometry, and are shifted to higher values than global mean temperature because they are from the (relatively warm) North Atlantic Ocean. Yet this does not explain their large variation amplitudes; we infer that these Mg/Ca data may reflect variations in other environmental parameter(s) in addition to temperature ([Yu and Elderfield, 2008; Yu and Broecker, 2010](#)). From these large-amplitude deep-sea temperature variations, [Jakob et al. \(2020\)](#) calculated anomalously large-amplitude compensating δ_w variations, which they

converted into large-amplitude sea-level variations based on an assumed constant $\Delta\delta_w:\Delta z_{SL}$ relationship. The other record with substantial deviations, [Miller et al. \(2020\)](#), is discussed in detail in [section 5.3](#).

The [Berends et al. \(2021a\)](#) inverse-modeling sea-level reconstruction is based on the [Lisiecki and Raymo \(2004\)](#) δ_c record, and can be compared precisely with our process modeling sea-level reconstruction ([Figure 11c](#)). This reveals close agreement between results from these completely different approaches, with a negligible 3.3 m mean offset and 12.4 m standard deviation ([Figure 11d](#)). Some of the data spread arises from a smoother [Berends et al \(2021a\)](#) record than our ([Rohling et al., 2021](#)) assessment, which arises from greater inertia in ice-volume changes in the [Berends et al. \(2021a\)](#) approach. Regardless, coherence between these two entirely different deconvolution methods provides a degree of mutual validation, although ideally entirely independent sets of input data sets should be tested, and a conclusive explanation is needed for the AIS inertia difference.

5.2. Plio-Pleistocene fine-tuning and synthesis

Next, we fine-tune the chronologies of the [Lisiecki and Raymo \(2004\)](#) and [Westerhold et al. \(2020\)](#) δ_c records. Timing tie-points are indicated by red diamonds for the [Lisiecki and Raymo \(2004\)](#) record, and black diamonds for the [Westerhold et al. \(2020\)](#) record ([Figures 12–14](#)) and are listed in [Table 1](#). For the last 40,000 years, we use tuning targets from the fossil coral data. Further back to 150 ka, we use key changes in the Mediterranean Sea (LC21) and Red Sea records as tuning targets, and between 150 and 500 ka only key changes in the Red Sea record ([Figure 12](#)). Finally, we fine-tune the [Lisiecki and Raymo \(2004\)](#) and [Westerhold et al. \(2020\)](#) chronologies between 500 and 800 ka using the timing relationship observed between 0 and 500 ka among (a) the tuned deep-sea temperature variations based on our process modeling of the [Lisiecki and Raymo \(2004\)](#) and [Westerhold et al. \(2020\)](#) δ_c records; and (b) the Antarctic temperature variations of [Jouzel et al. \(2007\)](#) ([Figure 13](#)). Before 792 ka and until 5.3 Ma, we have minimally synchronized the [Westerhold et al. \(2020\)](#) record to the [Lisiecki and Raymo \(2004\)](#) record ([Figure 14](#)) because, at this stage, the [Lisiecki and Raymo \(2004\)](#) record (1) provides the most ubiquitously used Plio-Pleistocene chronology; and (2) has a nearly identical chronology to the Mediterranean Plio-Pleistocene

stack that was dated independently on a precession scale based on Green Sahara Periods (monsoon maxima) (Larrasoaña et al., 2013; Rohling et al., 2014, 2015; Grant et al., 2017, 2022; and references therein). Note that, for completeness when making a our joint Plio-Pleistocene synthesis, we in addition present the inverse, where the Lisiecki and Raymo (2004) chronology is tuned to that of Westerhold et al. (2020) between 792 ka and 5.3 Ma (below). Before 5.3 Ma, we always use the Westerhold et al. (2020) δ_c record on its originally published chronology.

The chronologically fine-tuned records based on Lisiecki and Raymo (2004) and Westerhold et al. (2020) (Figures 12–14) better illustrate general signal similarities among the long-term continuous records than their untuned counterparts (Figures 9–11), by removing distracting timing mismatches. This similarity is used below to create a Plio-Pleistocene synthesis record (Figure 15). In Figure 14, we plot both the longer inverse modeling reconstruction of de Boer et al. (2010) and the latest generation of that approach (Berends et al., 2021a). The two solutions are similar back to ~ 3 Ma, although the de Boer et al. (2010) record has somewhat smaller amplitude variations. Before ~ 3 Ma, the de Boer et al. (2010) reconstruction sits lower than even the lower bound of the Berends et al. (2021a) record, and continuation of the de Boer et al. (2010) record beyond 3.5 Ma also is also remarkably invariant and low relative to our process modeled reconstructions (Figure 14). This continuous feature of the de Boer et al. (2010) record, which extends from 3 to 13 Ma (Figure 16), is inconsistent with GMSL estimates from Mallorca (Dumitru et al., 2019, 2021) and Patagonia (Rovere et al., 2020) and with the RSL amplitude variability ranges of Grant et al. (2019). The Miller et al. (2020) sea-level reconstruction suggests greater variability than our process modeled estimates (Rohling et al., 2021) before ~ 3.5 Ma, and is inconsistent with GMSL estimates from Patagonia (Rovere et al., 2020) (Figures 14, 16).

Given strong similarities between the chronologically fine-tuned process model results for the records based on Lisiecki and Raymo (2004) and Westerhold et al. (2020) (Figure 15), we probabilistically assess these records together. This involves conversion of each δ_c record 5,000 times in Monte Carlo style into sea level with the mean regression, while using prediction intervals as if they (in the conventional sense) characterize true random noise. Similar to the procedure in section 4, the joint 10,000 sea-level record iterations are used to determine the median z_{SL} and its 0.5th and 99.5th percentiles (estimated by bootstrapping

with replacement), to provide an overall sea-level median with a 99% probability interval for the median (Figure 15a). The process model approach next provides the joint δ_w variations (Figure 15c), which, combined with the original δ_c record, yield the joint median deep-sea temperature record and its 99% probability interval (Figure 15b).

Because questions have been raised regarding the Lisiecki and Raymo (2004) chronology (Wilkins et al., 2017), we have also turned the chronological fine-tuning procedure around, using the same tie points to fine-tune the Lisiecki and Raymo (2004) chronology to that of Westerhold et al. (2020) (Supplementary Figure S2). This reproduces Figure 15 with an alternative chronology, but the differences are almost imperceptible at the scale plotted, except for the emergence of small offsets with the other records presented, which largely used the Lisiecki and Raymo (2004) chronology. Both chronological options are made available in the datasets for this study, but for the sake of comparisons with previous work, we continue with the version that uses fine-tuning of Westerhold et al. (2020) to Lisiecki and Raymo (2004) between 792 ka and 5.3 Ma (i.e., the configuration shown in Figure 15).

Our synthesis sea-level record from the process modeling approach is compared in Figure 15a with the inverse modeling approach of Berends et al. (2021a), and Mallorcan and Patagonian GMSL estimates (Dumitru et al., 2019, 2021; Rovere et al., 2020). Also shown is the *a-priori* assumption-based sea-level reconstruction of Hansen et al. (2013; section 3.3). The latter reconstruction is shown throughout the last 40 million years in Figures 16a, 16b, and the assumption behind this reconstruction is illustrated in Figure 16d. For sea level, the Hansen et al. (2013) reconstruction is similar to our process model synthesis, albeit slightly displaced to lower values. The stepped navy-blue dotted lines in Figures 15a and 15b are evaluated in section 6.4.

Our Plio-Pleistocene deep-sea temperature synthesis is compared in Figure 15b with Antarctic temperature variations (scaled 1:4), the noble gas estimate of LGM global ocean cooling relative to present (Bereiter et al., 2018), and deep-sea temperature changes following the Hansen et al. (2013) approach. The latter record has a less convincing Late Pleistocene structure of generally cold glacials that are punctuated sharply by warmer conditions associated only with peak interglacials. It is also displaced to high values relative to the other methods.

Our process model-based synthesis median δ_w record is compared in [Figure 15c](#) with a δ_w reconstruction from Mg/Ca-paleothermometry-based δ_c correction in the SW Pacific ([Elderfield et al. 2012](#)) and a multi-record δ_w stack from Mg/Ca-paleothermometry-based δ_c correction ([Ford and Raymo, 2019](#)). These records generally agree well, although those from Mg/Ca-based δ_c correction are considerably noisier than our process model-based synthesis δ_w record. Also, the Mg/Ca-derived δ_w records seem to have roughly 25% larger amplitudes of variability (although it is within reported uncertainties; [Ford and Raymo, 2019](#)). This suggests that Mg/Ca temperature variations used by [Ford and Raymo \(2019\)](#) may have been ~25% smaller than estimated from process modeling (but within uncertainties), and highlights that environmental factors other than deep-sea temperature may be contributing to the excessive variability reconstructed by [Jakob et al. \(2020\)](#) ([section 5.1](#); [Figures 11, 14](#)).

5.3. Deeper-time comparisons and sensitivity tests

Comparison between records before 5.3 Ma requires parallel evaluation of influences of latent (unknown) parameters in our process modeling. Such concerns are especially relevant before the end of the Middle Miocene cooling at ~13 Ma. Key uncertainties to consider were discussed in [section 4](#), and could cause: (a) different shapes of the projected $\Delta\delta_c:\Delta z_{SL}$ relationship from that in [Figure 6](#); and (b) different Rayleigh distillation of precipitation over the AIS during past warm periods. We assess these possibilities in [Figure 16](#). Our main scenario follows the regression determined in [Figure 6](#) (black in [Figure 16d](#)). In light blue is sensitivity test *i* with a smoothly disturbed $\Delta\delta_c:\Delta z_{SL}$ relationship ([Figure 16d](#)) and no change in Rayleigh distillation of Antarctic precipitation; i.e., the AIS is modeled continuously as a “cold” ice sheet. The smooth $\Delta\delta_c:\Delta z_{SL}$ relationship is set so that it reaches a similar $\Delta\delta_c:\Delta z_{SL}$ slope for the peak AIS growth phase as it did later in the peak LIS+EIS growth phase ([Figure 16d](#)). In sensitivity test *ii* (pink), the same smoothly disturbed $\Delta\delta_c:\Delta z_{SL}$ relationship is used ([Figure 16d](#)) along with a change in Rayleigh distillation of Antarctic precipitation; i.e., AIS is modeled continuously as a “warm” ice sheet, similar to the Plio-Pleistocene LIS or EIS. Changes in these sensitivity tests affect the proportional $\Delta\delta_w$ and $\Delta\delta_{(TW)}$ contributions to $\Delta\delta_c$ non-linearly ([Figure 16e](#)). The $\Delta\delta_w$ versus $\Delta\delta_{(TW)}$ influences proposed by [Hansen et al. \(2013\)](#) are intermediate (cyan) to our scenarios ([Figure 16d](#)). Note that this is not the record of [Hansen et al. \(2013\)](#); rather, it is our calculation in which the ice-volume versus deep-sea

temperature proportionalities proposed by Hansen et al. (2013; section 3.3) are applied to the Westerhold et al. (2020) δ_c record, expressed relative to present (0 ka). We compare these results with those of de Boer et al. (2010), Miller et al. (2020), and the GMSL benchmarks of Dumitru et al. (2019, 2021) and Rovere et al. (2020). In addition, we add comparisons with sediment-sequence based sea-level variability (partly corrected to approximate GMSL; Kominz et al., 2016); with $\Delta\delta_c$, ΔT_w (Mg/Ca-based), and $\Delta\delta_w$ between ~ 20 and ~ 34 Ma (Lear et al., 2004); and with $\Delta\delta_c$, ΔT_w (both Mg/Ca and Δ_{47} -based), and $\Delta\delta_w$ between ~ 12 and ~ 16 Ma (Modestou et al., 2020).

Before discussing this comparison, we assess the implications and realism of our perturbed process model sensitivity tests (Figure 17). This assessment highlights the fundamental drivers of the $\Delta\delta_c$: Δz_{SL} relationship shape. Two plots of $\Delta\delta_w$ versus Δz_{SL} (Figure 17a) are obtained from the process modeled V_{ice} and δ_{ice} changes; one with “cold” AIS Rayleigh distillation (more fractionated; blue) and the other with “warm” AIS Rayleigh distillation (less fractionated; pink). These modeled $\Delta\delta_w$ versus Δz_{SL} plots are independent of deep-sea temperature. A theoretical deep-sea temperature curve is also shown in Figure 17a (plotted as $\Delta\delta_{(Tw)}$, which is $\Delta T_w/-4$). This is constrained by three “knowns”: (1) a full glacial lower limit/asymptote at ~ 3 °C below the present-day mean deep-sea temperature; (2) a present-day deep-sea temperature anomaly of 0 °C, relative to present; and (3) an asymptote near the ice-free sea-level limit (65.1 m) above which there is no ice-volume contribution to deep-sea oxygen isotope change. From these constraints, the $\Delta\delta_{(Tw)}$ component is highly non-linear and follows a similar path to the simple function drawn. Combining the blue and pink $\Delta\delta_w$ curves with the $\Delta\delta_{(Tw)}$ curve gives the blue and pink relationships in Figure 17b, which are compared with our main-scenario $\Delta\delta_c$: Δz_{SL} regression (gray). The overall convex $\Delta\delta_c$: Δz_{SL} relationship shape is robust; deviations fall well within the main scenario prediction intervals (Figure 6b) and range of alternative regressions considered by Rohling et al. (2021; Figure 6a). However, the blue and pink data clouds in Figure 17b are from a schematic theoretical $\Delta\delta_{(Tw)}$ relationship, so it is useful to compare the theoretical $\Delta\delta_{(Tw)}$ relationship with those implied by comparing $\Delta\delta_w$ from our process model runs with $\Delta\delta_c$ (Figure 17c), where sensitivity tests (blue and pink) and main-case T_w results (same as the blue case) are compared with theoretical temperatures from Figure 17a. The model results have more restricted asymptoting behavior than the simple theoretical curve, with average deviations

< 1 °C. We conclude that our convex $\Delta\delta_c:\Delta z_{SL}$ regression is robust within the uncertainties indicated in Figure 6, while the $\Delta\delta_c:\Delta z_{SL}$ perturbations imposed in our sensitivity tests are drastic but potentially feasible (especially sensitivity test *i*; Figure 16d blue).

When comparing records in Figure 16, the Hansen et al. (2013) results are similar to our process model main scenario at sea levels up to about +10 m (Figures 16a, 16d). It is only beyond ~13 Ma that the Hansen et al. (2013) values diverge from our scenarios and fall between our main case and the sensitivity tests (i.e., the cyan and blue lines separate). The inverse modeling approach of de Boer et al. (2010) infers a much smaller amplitude variability and lower values between ~3 and ~13 Ma than the Hansen et al. (2013) method and either of our process model scenarios (especially beyond ~10 Ma), and the younger part of this flat segment in the de Boer et al. (2010) reconstruction is also incompatible with the Pliocene GMSL benchmarks of Dumitru et al. (2019, 2021) and Rovere et al. (2020).

Between ~13 and ~34 Ma (the latter marks the EOT), the de Boer et al. (2010) sea-level reconstruction has larger-amplitude variability than our various process model scenarios or the Hansen et al. (2013) record, but smaller amplitudes than the Miller et al. (2020) reconstruction (Figure 16a). The New Jersey sediment-sequence based reconstruction of Kominz et al. (2016) partially overlaps the de Boer et al. (2010) record, the Hansen et al. (2013) record, and our process model sensitivity test *i* between ~17 and ~21 Ma, but diverges from these records in younger intervals (except for a brief overlap at ~13 Ma). Conversely, the Miller et al. (2020) sea-level record has some consistency with the Kominz et al. (2016) data between ~11 and ~17 Ma, but diverges from it in the older segment (Figure 16a). The Kominz et al. (2016) record has been subject to large corrections that might require more comprehensive independent validation.

We have proposed that the difference factor (δT_{NH}) used by de Boer et al. (2010) to tune AIS volume changes to achieve a strong EAIS volume increase at the EOT may have been too strong (Rohling et al., 2021). This would result in Antarctic responses that are too strong from the EOT onward, culminating in a “full” AIS in which no further ice-volume changes could occur from ~13 Ma. This, in turn, would cause sea-level simulations to flatten into a plateau; a tendency that is broken only at ~3 Ma when Northern Hemisphere ice sheets started to develop. A less extreme δT_{NH} value would allow more ice-volume (sea-level) variability between ~13 and ~3 Ma, which would improve agreement with various other

methods. A lower δT_{NH} would also produce a more modest EOT sea-level change, and more muted sea-level variations until ~ 13 Ma. Neither our process model sensitivity tests nor the Hansen et al. (2013) method achieve quite as large an EOT sea-level drop as suggested by de Boer et al. (2010); we consider the large drop in the Miller et al. (2020) reconstruction to be questionable (see below). We emphasize that subsequent ice-sheet modeling advances have produced greater AIS variability than de Boer et al. (2010) during the Miocene and Pliocene (e.g., Pollard et al., 2015; Gasson et al., 2016), which suggests that the δT_{NH} parameter may not have been the (only) critical factor. The EOT conundrum is further explored in [section 6.2](#).

Support for the large-amplitude and low sea-level values before ~ 4.5 Ma in the Miller et al. (2020) record (largely between -50 and $+20$ m) is lacking from other records ([Figures 14, 16](#)). The anomalous pattern in this record has a potentially straightforward explanation. We converted the δ_c , sea-level, and δ_w values of Miller et al. (2020) into anomalies relative to present-day (0 ka) ([Figures 16a, 16c](#)) to plot versus other records, which involves backing out the deep-sea temperature record in values relative to present ([Figure 16b](#)). As Miller et al. (2020) discuss, their deep-sea temperature record is highly smoothed, which allows only million-year timescale comparisons. However, the backed-out T_w record is not only smoothed, but also offset from other T_w records to generally high values, with considerable temporal discrepancies that imply anti-phased Myr-scale trends in several cases ([Figure 16b](#)). We suggest that use of this record together with a detailed δ_c record—which is similar to the Westerhold et al (2020) δ_c record ([Figure 16c](#))—caused a general shift in calculated δ_w toward more positive values (larger ice volumes), and that temporal T_w discrepancies produced exaggerated Myr-scale “cycles”.

The δ_c record (purple) of Lear et al. (2004) with Mg/Ca-based temperatures (red) between ~ 34 and ~ 19 Ma is shown in [Figures 16c and 16b](#), respectively. This record extends through the EOT, but the authors expressed reservations about the data across the EOT; we here use only the upper portion. The two records allow calculation of a δ_w record ([Figure 16c](#), brown). Overall, these three records compare well with our main-scenario results or sensitivity test *i* (blue), although agreement is less convincing between ~ 19 and ~ 23 Ma. In that interval, T_w is elevated (yet still consistent with our sensitivity test *i*), but there is a δ_c offset relative to our input-record of Westerhold et al. (2020) ([Figure 16c](#), purple versus

red). If adjusted, agreement of the [Lear et al. \(2004\)](#) δ_w values with our records in the ~23 to ~34 Ma interval would continue through the ~19 to ~23 Ma interval. This suggests that a more realistic range to consider for our process model results through the ~19 to ~34 Ma interval is bounded by the main scenario (gray) and sensitivity test *i* (blue). This range encompasses the intermediate [Hansen et al. \(2013\)](#) scenario, but is narrower than the full variability of [de Boer et al. \(2010\)](#). Finally, we note that the [Lear et al. \(2004\)](#) δ_w reconstruction differs substantially from the record of [Miller et al. \(2020\)](#) ([Figure 16c](#)).

The Middle Miocene Climate Optimum (MCO; ~14.5 to ~17 Ma) was characterized by high sea levels and high deep-sea temperatures, and ended in global cooling across the Middle Miocene Climate Transition (MMCT; ~12 to ~14.5 Ma) ([Figures 5, 16](#)) ([Steinthorsdottir et al., 2021](#)). Our process modeled scenarios suggest ~2 to 2.5 °C cooling, or even 3 °C cooling in sensitivity test *ii* ([Figure 16b](#)), along with 0.35 ± 0.1 ‰ δ_w change. Mg/Ca-based studies instead suggest a 1.5 ± 0.5 °C cooling, and a δ_w change of 0.53 ± 0.13 ‰ ([Mudelsee et al., 2014](#)). This small Mg/Ca-based temperature change is not well supported by independent paleothermometry. [Modestou et al. \(2020\)](#) measured deep-sea δ_c and both Mg/Ca and clumped isotope (Δ_{47}) paleotemperatures from a SE Indian Ocean core across the MMCT. Their δ_c data match closely with the [Westerhold et al. \(2020\)](#) record when aligned at 15 Ma ([Figure 16c](#); blue dots against right-hand y-axis). Their Mg/Ca paleotemperatures ([Figure 16b](#); blue dots and thin blue trend line, versus right-hand y-axis) have a considerably smaller MMCT shift than our process model reconstructions, similar to the aforementioned difference with the [Mudelsee et al. \(2014\)](#) reconstruction. But the Δ_{47} paleotemperatures of [Modestou et al. \(2020\)](#) ([Figure 16b](#); solid blue line versus right-hand y-axis) reveal a much greater MMCT gradient than their Mg/Ca paleotemperatures (reaching ~2.5 °C), even if both methods produce warm absolute values with an 8-11 °C range. For modern global mean deep-sea temperatures of 1-2 °C ([Emery, 2001](#); [Pawlowicz, 2013](#)), this implies 6-10 °C for our T_w comparisons in [Figure 16b](#) (for discussion see [section 6.3](#)). We calculate δ_w changes using their relative Mg/Ca-based temperature changes ([Figure 16c](#); green dots versus right-hand y-axis), and also δ_w changes after (a) adjusting for the gradient difference between Mg/Ca and Δ_{47} paleotemperatures (i.e., using Mg/Ca-based variability with the Δ_{47} -based gradient), and (b) translating this adjusted δ_w record so that it overlaps with the [Modestou et al. \(2020\)](#) δ_c data at the younger end ([Figure 16c](#); black dots versus right-hand

y-axis). This illustrates that—apart from the high absolute temperatures from proxy data at this site—the T_w gradient does not differ much from our process model reconstructions; reasonable agreement is found for relative T_w and δ_w gradients between the [Modestou et al. \(2020\)](#) data and our main scenario and sensitivity test *i* process model results.

6. DISCUSSION

6.1. Uncertainty assessment

Core to the process modeling approach ([Rohling et al., 2021](#)) is the convex $\Delta\delta_c:\Delta z_{SL}$ regression curve with projection to the ice-free state. [Rohling et al. \(2021\)](#) demonstrated that generously different convex projections ([Figure 6a](#)) do not cause major reconstruction uncertainties. We here added probabilistic analyses of individual reconstructions by propagating the influences of wide prediction limits to the regression ([Figure 6b; section 4](#)), which revealed that, for each scenario, the median Δz_{SL} reconstruction is determined within $\pm 2\text{--}3\text{ m}$ ([section 4](#)). This merely marks the window in which the Δz_{SL} median is found, and not the window in which existing or newly added reliable datapoints must fall (the prediction interval, with estimated 95% confidence bounds of on average $\pm 13\text{ m}$; [section 4](#)). Part of the issue is obvious when comparing different medians between the [Lisiecki and Raymo \(2004\)](#) and [Westerhold et al. \(2020\)](#) based records. For a synthesis of these two records, we first probabilistically merged their results ([Figure 15](#)). Second, we also evaluated the robustness of the convex $\Delta\delta_c:\Delta z_{SL}$ regression shape (within the bounds explored in [Figure 6](#)), using sensitivity tests with imposed $\Delta\delta_c:\Delta z_{SL}$ perturbations ([Figure 16d](#)) that remain just within $\pm 1^\circ\text{C}$ of theoretical deep-sea temperature constraints ([section 5.3](#)). Here, $\pm 1^\circ\text{C}$ is a relevant range because it is the total-resolution range limit for current paleotemperature methods, which means that these methods cannot distinguish empirically between our main case or sensitivity tests.

This uncertainty framework can be tested by comparison with independent estimates. All key parameters are interlinked (sea level, ice volume, δ_c , δ_{ice} , δ_w , and T_w), so that change in one necessarily drives change in others. The process model provides mutually consistent solutions across these parameters, and reconstructions can be validated using multiple criteria ([Rohling et al., 2021](#)). Notable validation criteria are the GMSL benchmarks of [Dumitru et al. \(2019, 2021\)](#) and [Rovere et al. \(2020\)](#), and sea-level estimates from the latest-

generation independent (and also internally consistent) inverse modeling approach (Berends et al., 2021a). Additional criteria were used to validate our model-reconstructed sea level, δ_w , and T_w through the Plio-Pleistocene (Figures 9–15; see also Rohling et al. (2021); especially for additional δ_{ice} validations). Our process model-based reconstructions overall agree within uncertainties with most validation criteria. Hence, we propose that our Plio-Pleistocene synthesis reconstruction (Figure 15) provides a useful template for orbital time-scale variability during that interval.

The inverse modeling approach (Bintanja et al., 2005; Bintanja and van de Wal, 2008; de Boer et al., 2013, 2017; Berends et al., 2019, 2021a) also accounts for key parameter interdependences, and its latest generation (Berends et al., 2021a) compares well with our analyses (Figure 11d). In deeper time, beyond ~ 3.3 Ma, however, the earlier version of the inverse modeling method produced a flat and low sea-level “plateau” that extends to ~ 13 Ma (de Boer et al., 2010). This plateau deviates from GMSL benchmarks between ~ 3.3 and ~ 5.5 Ma (Figures 14, 16), and also from the later reconstruction of Berends et al. (2021a). The record also suggests ~ 10 to ~ 15 m_{seq} latest Eocene AIS volume variations. While support exists for the de Boer et al. (2010) record from the Kominz et al. (2016) data between ~ 17 and ~ 21 Ma, this potential corroboration is doubtful because of major discrepancies between these records from ~ 11 to ~ 17 Ma (except for ~ 15 Ma). We attribute this inconsistency to a need for independent validation of the major RSL-to-GMSL corrections in the Kominz et al. (2016) record. Overall, we consider the de Boer et al. (2010) sea-level record to be too sensitive with respect to AIS variations, which affects the entire record before ~ 3.3 Ma. We suggested that de Boer et al. (2010) used too strong a value for their tuning factor (δT_{NH}) that regulates AIS-volume variation amplitudes (section 5.3). δT_{NH} was set to produce a larger sea-level jump at the EOT (~ 34 Ma), but thereafter may have produced large-amplitude AIS variability that culminated in a “fully” glaciated Antarctica by ~ 13 Ma, following which no orbital-scale ice-volume (sea-level) variability occurred until substantial Northern Hemisphere glaciation commenced from ~ 3.3 Ma. However, the choice of δT_{NH} may not have been the sole cause of the 3.3-13 Ma sea-level plateau of de Boer et al. (2010), given that subsequent ice-modeling improvements imply larger AIS ice-volume variability (e.g., Pollard et al., 2015; Gasson et al., 2016). Sea-level results from a more advanced generation of inverse modeling (Berends et al., 2021a) fall closer to the GMSL

benchmarks (Figure 14), and it would be valuable for this generation to be extended beyond its current limit of ~3.6 Ma, including deeper comparison and validation of its other key parameters against independent records.

The Hansen et al. (2013) method does not explicitly consider parameter interdependences, but accounts for them implicitly by setting calculations as a closed sum (similar to our theoretical arguments in Figure 17). However, the two-part linear relationship assumed by Hansen et al. (2013) leads to considerable T_w deviations from more nuanced assessments (Figure 15), and fails to reproduce the well-established T_w signal structure of generally cold glacials with little variability, punctuated by sharply delineated warm peak interglacials (Cutler et al., 2003; Elderfield et al., 2012; Siddall et al., 2010; Bates et al., 2014). Regardless, the Hansen et al. (2013) sea-level record falls between our process model main case and sensitivity tests, so it does not further influence uncertainty assessment.

When interdependences between key parameters (sea level, ice volume, δ_c , δ_{ice} , δ_w , and T_w) are not explicitly accounted for, major anomalies can arise. Inconsistencies between input records in the calculations of Miller et al. (2020) may have caused a shift in their calculated δ_w toward more positive values (low sea levels) and exaggerated Myr-scale “cycles” (section 5.3). This contrasts with the post-EOT results of Lear et al. (2004) (Figure 16c) and the Mg/Ca compilation of O’Brien et al. (2020) shown by Rohling et al. (2021). For example, Miller et al. (2020) infer a very large sea-level (ice-volume) change across the EOT (Figure 16a), but this is due entirely to their δ_c record having the same shift as other δ_c records (Figure 16c), while their highly smoothed paleotemperature record suggests a 1 °C warming across the EOT, in contrast to coolings in other records.

The analyses of Lear et al. (2004) between ~23 and ~34 Ma generally agree with the range of reconstructions from our process model main scenario and sensitivity test *i* (Figures 16b, 16c). As argued in section 5.3, a discrepancy between these records in the ~19 to ~23 Ma interval seems to arise from a δ_c offset relative to our input record of Westerhold et al. (2020) (Figure 16c, purple versus red). If adjusted, the same level of agreement would be seen as in the ~23 to ~34 Ma interval. The Modestou et al. (2020) records from ~12 to ~16 Ma using the Δ_{47} -based MMCT T_w gradient compare reasonably with the range of our process model main case and sensitivity test *i* in terms of relative change, but not with respect to absolute values (section 6.3).

Finally, sensitivity test *ii* (pink in Figure 16) assumes more limited AIS $\delta^{18}\text{O}$ fractionation due to Rayleigh distillation (i.e., relatively “warm” LIS-like behavior as detailed by Rohling et al., 2021), and finds less δ_w change per unit AIS-volume (and sea-level) change. For the same input- δ_c change, this scenario must invoke more T_w change. In consequence, sensitivity test *ii* suggests a larger MMCT temperature shift than even the clumped-isotope record of Modestou et al. (2020) (Figure 16b). Similarly, sensitivity test *ii* causes a more extreme T_w change across the EOT (section 6.2). For these reasons, we do not consider sensitivity test *ii* further.

6.2. The EOT conundrum

The abrupt T_w decrease across the EOT has been estimated at $\sim 2.5^\circ\text{C}$ from Mg/Ca paleothermometry (no uncertainties reported), with a two-stage δ_w shift to more positive values of 0.2 ‰ and then another 0.4 ‰ (Lear et al., 2008). The EOT temperature shift from our process model main case (gray) and sensitivity test *i* (blue) spans $3 \pm 0.5^\circ\text{C}$ (Figure 16b), which is within uncertainties of the deep-sea Mg/Ca paleothermometry method. The total δ_w shift in our main case is only 0.3-0.35 ‰, which is only half of that inferred by Lear et al. (2008). However, the total δ_w shift in sensitivity test *i* is ~ 0.5 ‰, which approximates that inferred by Lear et al. (2008). According to other work, the EOT T_w change may have been even smaller; Gasson et al. (2013) reviewed Eocene to present climate change and stated: “Recent work attempting to correct for the simultaneous influence of changing seawater saturation state on the EOT deep-sea Mg/Ca records implies a deep-sea cooling on the order of 1.5°C , although this estimate will likely be refined as understanding of trace metal proxies advances [Lear et al., 2010; Pusz et al., 2011].” In contrast, modeling studies suggest that the cooling may have been 4°C (Liu et al., 2009). DeConto and Pollard (2003) modeled “glacial inception and early growth of the EAIS using a general circulation model with coupled components for atmosphere, ocean, ice sheet and sediment, and which incorporates paleogeography, greenhouse gas, changing orbital parameters, and varying ocean heat transport.” They found a two-stage change across the EOT with a total sea-level change of ~ 35 to ~ 45 m (for a ~ 0.3 to ~ 0.4 ‰ shift, which they converted linearly using 0.0091 ‰ m^{-1}), measured just before and after the shift in their Figure 2. The simulated 0.3-0.4 ‰ shift of DeConto and Pollard (2003) agrees with our main case (0.3-0.35 ‰) and sensitivity test *i*

(0.5 ‰) (Figure 16c). Similarly, the simulated ~35 to ~45 m EOT sea-level drop of DeConto and Pollard (2003) compares well with the range between our main case (25-30 m) and sensitivity test *i* (~40 m), as well as with the ~45 m estimate of de Boer et al. (2010) (but note that these authors tuned their EOT sea-level amplitude considerably to the DeConto and Pollard (2003) result). Unfortunately, DeConto and Pollard (2003) could not report an EOT T_w change from their model because they used a slab-ocean component, which did not include the deep ocean.

Before presenting further comparisons, we emphasize the caveat that changes in Antarctic topography and bathymetry (Wilson et al., 2012; Paxman et al., 2019; Hochmuth et al., 2020) are not considered here, and may have a substantial bearing on the EOT sea-level amplitude. Notably, a larger Antarctic land area above sea level at the EOT may have caused a larger ice volume increase (sea-level drop) (Wilson et al., 2013).

A multi-proxy study of Alabama shelf deposits led to an interpreted ~55 m total EOT sea-level fall along with a ~0.4 ‰ $\delta^{18}O$ change that added to an earlier 0.5 ‰ step, which reflects a total ~4 °C shallow-water temperature drop (Miller et al., 2008). Miller et al. (2009) revisited these results in a broader context and inferred an initial sea-level fall of ~25 m followed by a ~55-70 m sea-level fall (then inflated to an 82-105 m sea-level fall by isostatic corrections with no details provided) accompanied by ~2 °C cooling. Large 60-70 m RSL changes have also been inferred from marginal marine deposits in NE Italy, but no uncertainties in the microfacies-based sea-level reconstructions were expressed (Houben et al., 2012).

It is striking that the methods in our assessment that explicitly or implicitly account for parameter interdependences produce similar sea-level changes of 25-45 m across the EOT, as illustrated by our main case and sensitivity test *i*, Hansen et al. (2013), de Boer et al. (2010), and the model-based result of De Conto and Pollard (2003). This agreement is also clear in terms of δ_w , which spans a 0.3-0.5 ‰ range among studies. Moreover, the 0.6 ‰ δ_w shift inferred from Mg/Ca-temperature correction of the δ_c change (Lear et al., 2008) is statistically similar to the aforementioned range when accounting for realistic ± 1 to 1.5 °C (1 σ) uncertainties (Lear et al., 2002; Martin et al., 2002; Marchitto & deMenocal, 2003; Marchitto et al., 2007; Yu & Elderfield, 2008; Elderfield et al., 2010; Weldeab et al., 2016; Hasenfratz et al., 2017; Barrientos et al., 2018) in their Mg/Ca-based ~2.5 °C cooling

estimate, which impose as much as ± 0.25 to 0.38 ‰ uncertainty in reconstructed δ_w variations ([section 3.3](#)). [Hutchinson et al. \(2021\)](#) reviewed climate changes across the EOT and inferred that an AIS grew equivalent to 70-110% of its modern volume ($\sim 40\text{-}60 \text{ m}_{\text{seq}}$), although this mainly relies on Mg/Ca-based reconstructions of 0.6 ‰ δ_w change (e.g., [Lear et al., 2008](#)).

The much greater sea-level jumps in various RSL interpretations fall well outside the estimates summarized above, which requires attention in future research. Specific attention is needed on: (1) uncertainty estimates in RSL estimates, and (2) RSL-to-GMSL corrections for tectonic movements, dynamic topography, and GIA ([section 2](#)). [Kominz et al. \(2016\)](#) ([Figure 16](#)) suggested that propagated uncertainties in variability estimates from such RSL records may reach $\pm 10 \text{ m}$ for deposits only half as old as the EOT. Given that the EOT spans up to $\sim 400,000$ years, with two $\sim 40,000$ -year shifts to lower sea level ([Coxall et al., 2005](#)), it is long enough for considerable uncertainty build-up in the relationship between RSL and GMSL change. For example, uplift in shallow-water environments due to isostatic responses to sea-water unloading (GMSL lowering), or longer-term tectonic or dynamic topography uplift, could amplify GMSL lowering in the local RSL signature.

6.3. Middle Miocene changes

With CO_2 levels of $\sim 400\text{-}600 \text{ ppm}$ and global temperatures some $7\text{-}8 \text{ °C}$ warmer than during the Holocene, the MCO is gaining increasing interest as a period for assessing the performance of models that are also used for future climate change projections ([Steinthorsdottir et al., 2021](#)). [Gasson et al. \(2016\)](#) used an isotope-enabled ice-sheet model to investigate Middle Miocene Antarctic ice-sheet variations for warm and cold scenarios, using either modern or an approximate Middle Miocene bed topography. Across the two topographic scenarios, they inferred equilibrium δ_w differences between colder and warmer conditions of $0.52\text{-}0.66 \text{ ‰}$ and sea-level differences amounting to $30\text{-}36 \text{ m}$. In contrast, our process modeled main case and sensitivity test *i* suggest about $0.35 \pm 0.1 \text{ ‰}$ δ_w change for $30\text{-}40 \text{ m}$ of sea-level change across the MMCT ([Figures 16, 18](#)). Mg/Ca-based studies infer a δ_w change of $0.53 \pm 0.12 \text{ ‰}$ across the MMCT, along with $1.5 \pm 0.5 \text{ °C}$ of deep-sea cooling ([Mudelsee et al., 2014](#)). The Mg/Ca-based estimate of MMCT δ_w change seems to agree

more with the [Gasson et al. \(2016\)](#) estimate, but agreement shifts in favour of our smaller process modeled estimate when using the [Modestou et al. \(2020\)](#) temperature gradient from Δ_{47} rather than Mg/Ca ([Figure 16c](#)). Improved deep-water paleothermometry is needed before even considerable changes such as the MMCT deep-sea temperature shift can be resolved at sufficient precision to distinguish between model-based estimates.

It is also intriguing that [Gasson et al. \(2016\)](#) reported an AIS with a volume of 58 to 78 m_{seq} in their cold simulation used to compare with warm MCO scenarios. The largest AIS volume after the MMCT in the process modeling approach is $>50 m_{seq}$ (sea level minimum at ~ 5 m between 8 and 9 Ma in sensitivity test *i*, which is similar to estimates of [de Boer et al. \(2010\)](#); [Figures 16a, 18a](#)). These independent approaches are more supportive of the low-end estimate of [Gasson et al. \(2016\)](#) than of their high-end estimate. These estimates indicate a maximum Miocene AIS volume that was similar to the modern AIS volume. Relative to $\sim 58 m_{seq}$ of modern AIS volume, both our process modeling estimates of 30-40 m sea-level change across the MMCT and the [Gasson et al. \(2016\)](#) estimate of 30-36 m for the Middle Miocene sea-level range suggest periodic loss equivalent to 50-70 % of modern AIS volume during the Middle Miocene. This agrees well with the 30-80 % range summarized by [Gasson et al. \(2016\)](#) from [Miller et al. \(2005\)](#), [Kominz et al. \(2008\)](#), [Shevenell et al. \(2008\)](#), [de Boer et al. \(2010\)](#), [Lear et al. \(2010\)](#), [John et al. \(2011\)](#), [Liebrand et al. \(2011\)](#), and [Holbourn et al. \(2013\)](#). During such major retreat phases, tundra and shrub tundra were established along with woody sub-Antarctic or sub-alpine vegetation and peat lands ([Lewis et al., 2008](#); [Warny et al., 2009](#); [Gasson et al., 2016](#); [Sangiorgi et al., 2018](#); [Steinthorsdottir et al., 2021](#)).

Diverse studies reviewed by [Steinthorsdottir et al. \(2021\)](#) indicate that Middle Miocene global deep-water temperatures were 5-9 °C warmer than today (i.e., $T_w = 5-9$ °C in the terminology used here), at the high end of MCO T_w estimates from the continuous δ_c deconvolution methods (e.g., [Figures 16b, 18b](#)). The deep-sea temperatures of 8-11 °C reported by [Modestou et al. \(2020\)](#) for the deep SE Indian Ocean (i.e., $T_w = 6-10$ °C, given modern deep-sea temperatures of 1-2 °C), are even higher ([Figure 16b](#)). We suggest that two issues call for urgent further investigation, namely: (1) the stark mean MMCT T_w gradient difference reported by [Modestou et al \(2020\)](#) between calibration-sensitive Mg/Ca and more thermodynamically grounded Δ_{47} paleotemperatures; and (2) the high absolute

1538 Middle Miocene global T_w values inferred from proxy data, especially for the deep SE Indian
1539 Ocean.

1540

1541 *6.4. Stepping down into Northern Hemisphere glaciation*

1542 Our Plio-Pleistocene synthesis record ([Figure 15](#); [section 5.2](#)) offers new insights into the
1543 nature of the step-down from a warmer climate state dominated by AIS variations with only
1544 minor (if any) LIS and EIS variations, to an ice-age climate dominated by LIS and EIS
1545 variations with relatively minor additional AIS variations. For illustration, we highlight a
1546 series of visually identified steps in [Figure 15](#) (navy blue dotted line) that demonstrate
1547 different temporal proportionalities of change in sea level and deep-water temperature (all
1548 changes discussed here are relative to present; 0 ka BP). The dotted lines are drawn
1549 between visually detected exceedance points: between 5.8 and 5.55 Ma, glacial sea level
1550 first dropped below 0 m, reaching just below –10 m, with concomitant T_w drops to –1 °C
1551 ([Figures 16, 18](#)). This was the lowest glacial sea level until ~3.3 Ma ([Figure 15](#)). At ~3.3 Ma,
1552 glacial sea level dropped further to roughly –40 m, while T_w plummeted to –2 °C ([Figure 15](#)).
1553 Then followed a two-stage drop between 2.75 and 2.50 Ma following which minima were
1554 reached at around –60 m for sea level and –2.5 °C for T_w . The key point here is not exactly
1555 when which value was exceeded, but that the proportionalities of sea level and deep-water
1556 temperature change were different through time.

1557 Numerous studies have documented evidence for Northern hemisphere ice-sheet expansion
1558 from the late Pliocene and through the Pleistocene (for overviews see [Maslin et al., 1998](#);
1559 [Bailey et al., 2013](#); Table 2 in [Rohling et al., 2014](#); and references therein). While this
1560 widespread evidence is not our focus, we note that the timings of our inferred sea-level
1561 step-downs coincide with key observations of increased glaciation. For example, the
1562 apparent step-downs at 2.7 and 2.5 Ma match the inferred timing of growth phases of
1563 individual ice sheets and/or the sequential development of different ice sheets, based on
1564 direct observational evidence such as ice-rafted debris (IRD) deposition (e.g., [Jansen and](#)
1565 [Sjøholm, 1991](#); [Kleiven et al., 2002](#); [Knies et al., 2009](#); [Naafs et al., 2013](#); [Bailey et al., 2013](#);
1566 [Liu et al., 2018](#); [Blake-Mizen et al 2019](#); [Sánchez-Montes et al., 2020](#)) and subsurface

mapping of glacial erosion and bedforms (e.g., Gebhardt et al., 2014; Rea et al., 2018; Harishidayat et al., 2021).

From ~1.25 to ~0.65 Ma, the MPT involved a transition to longer (~100-kyr) glacial cycles; with a range of hypotheses about the underlying causes that include CO₂ changes, regolith removal, non-linear cryospheric feedbacks, and/or different combinations of these (Shackleton and Opdyke, 1976; Pisias and Moore, 1981; Imbrie et al., 1993; Clark and Pollard, 1998; Berger et al., 1999; Tziperman and Gildor, 2003; Clark et al., 2006; Bintanja and van de Wal, 2008; Raymo and Huybers, 2008; Ganopolski et al., 2011; Tabor and Poulsen, 2016; Chalk et al., 2017; Willeit et al., 2019; Yehudai et al., 2021; Berends et al., 2021b). A major erosion event around the North Atlantic region at ~0.95 to 0.86 Ma (Yehudai et al., 2021) provides support to the hypothesis that regolith removal enabled the LIS and EIS to become more firmly grounded on bedrock rather than on loose “slippery” regolith, so that they could build up to larger sizes and grow/survive over longer, 100-kyr, timescales (Clark and Pollard, 1998). Throughout the MPT, and until the present, glacial T_w minima ranged between –2.5 and –2.9 °C in our synthesis record (Figure 15b). This relatively invariant glacial T_w behavior is similar to that seen in glacial atmospheric CO₂ levels over the same period, dropping by only ~20 ppmv (Yamamoto et al. 2022) to ~40 ppmv (Chalk et al., 2017), which implies a 0.25-0.6 °C global mean cooling when assuming a constant equilibrium climate sensitivity with a central estimate of 0.7 to 0.8 K W⁻¹ m⁻² (e.g., PALAEOSENS, 2012; Sherwood et al., 2020). In contrast, glacial sea-level minima underwent three major steps, to –70 m at ~1.25 Ma, –90 m at ~0.9 Ma, and about –120 m at ~0.65 Ma (Figure 15b). Independent evidence from seismostratigraphic assessment of Red Sea sediments indicates a first lithified “aplanktonic” layer at ~0.65 Ma during the marine isotope stage 16 glaciation (Mitchell et al., 2013). This supports our inference of a major step in glacial sea-level lowering at ~0.65 Ma because such lithified layers, which lack planktonic foraminifera and contain abundant inorganically precipitated aragonite, developed only during extreme sea-level lowstands when Red Sea exchange with the open ocean was restricted severely (e.g., Ku et al., 1969; Milliman et al., 1969; Deuser et al., 1976; Schoell and Risch, 1976; Ivanova, 1985; Halicz and Reiss, 1981; Winter et al., 1983; Reiss and Hottinger, 1984; Locke and Thunell, 1988; Thunell et al., 1988; Almogi-Labin et al., 1991; Rohling, 1994b; Hemleben et al., 1996; Rohling et al., 1998; Fenton et al., 2000).

Our inferred pattern of Plio-Pleistocene glacial T_w change reflects the approximation of a freezing limit for glacial deep-sea temperatures from ~1.25 Ma, and definitely after 0.9 Ma (Figures 17c, 18f). This non-linear, asymptoting glacial temperature behavior implies that a much greater proportion of glacial deep-sea cooling occurred at earlier stages than at later stages. Glacial sea-level minima, in contrast, stepped down more evenly through time. These well-defined step-down patterns of different proportionalities are not reproduced in recent climate model simulations driven by orbital forcing with optimal sub-glacial regolith removal and volcanic outgassing scenarios (Willeit et al., 2019). This suggests that either: (a) deep-water formation changes are too “linear” in their model, and may need to be more sensitive to threshold-style behavior (e.g., related to sea-ice); or (b) another, hitherto unidentified, mechanism may be responsible.

6.5. A 40-Myr synthesis

Based on comparisons presented above, we suggest that our Plio-Pleistocene synthesis reconstruction (Figure 15) provides a useful template for orbital time-scale climate variability in that interval. Beyond ~5.3 Ma, we propose that the range between our process model main case and sensitivity test *i* provides a reasonable template. Our summary synthesis for the entire last 40 Ma is presented in Figure 18. Future work is needed to refine this synthesis, especially in the pre-5.3 Ma interval. Attention is especially needed on: (1) discrepancies with RSL estimates and/or GMSL conversions in Kominz et al. (2008; 2016); (2) the high SE Indian Ocean absolute temperatures of Modestou et al. (2020); (3) the discrepancy with the model results of de Boer et al. (2010) beyond ~3.3 Ma, which may be resolved and/or assessed once the Berends et al. (2021a) method is extended back to ~40 Ma (although this is currently not computationally feasible).

It is important to emphasize that the uncertainty envelopes in Figure 18 do not represent random uncertainties. The two extremes (and all intermediate stages) represent fundamentally different $\Delta\delta_c:\Delta z_{SL}$ relationships governed by the AIS (> 0 m sea level) (Figure 18d). Such fundamentally different relationships depend on different AIS states and their interactions with the wider environment and climate. Hence, the uncertainty band represents the potential range within which structured long-term variability is expected.

The typical time scales of this structured long-term variability can be assessed from the main processes involved. Mean AIS δ_{ice} is one controlling parameter of the $\Delta\delta_c:\Delta z_{SL}$ relationship. Given that the current AIS (~55 m_{seq} volume) contains continuous ice that is up to 1 million years old (EPICA community members, 2004; Bender et al., 2008) with occasional older (~2 million years) segments (Yan et al., 2019), we infer that mean AIS δ_{ice} changes have typical time scales that range from 10^4 to 10^6 years. Another controlling parameter is the solid-Earth response to ice loading, and to large-scale tectonics and dynamic topography, with typical time scales that range from 10^4 to 10^7 years. Hence, one would expect structured “drift” of sea-level, deep-sea temperature, and δ_w records over such timescales within the given uncertainty intervals (for an illustration, see [Supplement section B](#) and [Supplementary Figure S3](#)).

Considering inevitable reconstruction uncertainties, we propose that it will be challenging to differentiate from proxy data where “reality” lies within the uncertainty band of [Figure 18](#). It may be more promising to determine the temporal nature of AIS variability relative to our uncertainty band with AIS modeling using 3D ice models with realistic ice-climate-ocean-topography-lithosphere coupling and with validation through like-for-like comparisons between forward-modeled and observed proxy data. However, this approach is infeasible currently due to computational limitations, as is the case for the method of [Berends et al. \(2021a\)](#). For the foreseeable future, therefore, simplified and/or parameterized approaches will remain useful, such as the process modeling approach used here. However, this approach contains assumptions and caveats that must be investigated and/or improved upon. We highlight a series of these, including at least: (1) more realistic ice-sheet representations that include isostatic adjustments based on ice loading and interactions between bed-friction and ice-sheet aspect ratio; (2) more physics-based rather than pre-defined representations of Rayleigh distillation to improve calculation of δ_{ice} changes; and (3) deeper assessments of potential changes in the relationship between δ_c and sea-level change.

7. CONCLUSIONS

Understanding ice-volume (sea-level) and deep-sea temperature variations over the past 40 million years is essential for many lines of research. Records of stable oxygen isotope ratios ($\delta^{18}\text{O}$) in carbonate of well-preserved deep-sea benthic foraminifera (δ_c) provide critical insight into global ice-volume and deep-sea-temperature variations over long intervals of time. These two properties need to be deconvolved. We compare and contrast records from a range of deconvolution approaches, including (1) direct scaling of δ_c records to sea-level records; (2) statistical deconvolutions of δ_c records; (3) paired δ_c and independent paleothermometry measurements; (4) the marginal sea water residence-time method; (5) statistically generalized sea-level reconstruction from diverse input records; and two hybrid data-modeling philosophies, namely (6) an inverse modeling approach, and (7) a recent process modeling method. We also compare these results with sea-level and deep-sea temperature assessments from independent methods. Throughout, we consider uncertainties and assumptions. We use a slightly updated version of our recent process modeling method as a framework to support comparison between methods because it accounts quantitatively for all major interdependences between changes in sea level, ice volume, ice $\delta^{18}\text{O}$, global mean seawater $\delta^{18}\text{O}$, global mean deep-sea benthic δ_c , and global mean deep-sea temperature. We observe a degree of signal similarity among methods, especially after fine-tuning of different chronologies. More detailed assessment reveals considerable differences that arise from uncertainties and assumptions specific to each approach.

Methods that account quantitatively for parameter interdependences—explicitly or implicitly—tend to have the most agreement, yet offsets remain. We argue that an earlier version of the inverse modelling approach (de Boer et al., 2010) uses a difference factor (δT_{NH}) to tune Antarctic Ice Sheet volume changes that may be too strong. This issue seems to have been largely alleviated in a newer version of this approach (Berends et al., 2021a), although it has yet to be applied to the critical pre-3.6 Ma interval. We also note that the δT_{NH} issue may not be the only reason for this change between the de Boer et al. (2010) and Berends et al. (2021a) reconstructions; improved (3D) representation of ice flow and margin instability, and use of GCM output rather than simple temperature scaling may have had at least as much impact.

Methods based on linear or piece-wise linear relationships between δ_c and sea level (ice volume)—whether analyzed from Pleistocene data or determined theoretically (e.g., [Waelbroeck et al., 2002](#); [Siddall et al., 2010](#); [Hansen et al., 2013](#); [Bates et al., 2014](#))—provide useful approximations for the past ~1-3 million years that were dominated by bi-polar glacial cycles. These methods provide less-well constrained reconstructions in older times, which were dominated by largely uni-polar (Antarctica only) glacial cycles.

Use of Mg/Ca-based or Δ_{47} -based paleothermometry in the deconvolution process produces records that agree with other methods within stated uncertainties, although uncertainties are large due to $\geq \pm 1$ °C (1σ) paleothermometry uncertainties (e.g., [Lear et al., 2004](#); [Elderfield et al., 2012](#); [Ford and Raymo, 2019](#); [Modestou et al., 2020](#); [O’Brien et al., 2020](#)). Mg/Ca temperature variations in some work seem ~25% smaller than estimated from process modeling (but within uncertainties) ([Ford and Raymo, 2019](#)), while other work finds 80% larger amplitudes (e.g., [Jakob et al., 2020](#)) and yet other work reports largely consistent variations (e.g., [Lear et al., 2004](#)). This, combined with a stark long-term gradient difference between calibration-sensitive Mg/Ca and more thermodynamically grounded Δ_{47} paleotemperatures ([Modestou et al., 2020](#)), suggests that other environmental factors beside deep-sea temperature might affect Mg/Ca-based temperature reconstructions.

We find that the Mg/Ca-based paleotemperature record used by [Miller et al. \(2020\)](#) is highly smoothed and offset from other deep-sea temperature change records; it seems biased to high values with considerable temporal discrepancies that imply anti-phased Myr-scale trends in several cases. Use of this record by [Miller et al \(2020\)](#) with their detailed δ_c record has caused a shift in their calculated δ_w (= global mean seawater $\delta^{18}\text{O}$) record toward anomalously positive values that imply exceptionally large ice volumes, and also produces exaggerated Myr-scale “cycles”. There is a need to better understand the high absolute temperatures from both Mg/Ca and Δ_{47} analyses at the SE Indian Ocean site of [Modestou et al. \(2020\)](#). These high values require us to impose a constant mean-shift when compared with other results. High deep-water temperature values are a common feature in Middle Miocene proxy data reconstructions ([Steinthorsdottir et al., 2021](#)), and the discrepancy relative to values from continuous deconvolution methods remains unexplained.

We present new template synthesis records of sea level, global mean seawater $\delta^{18}\text{O}$, and global mean deep-sea temperature changes, relative to present, for the last 5.3 million

years, which offer good agreement with diverse reconstructions from independent methods. We present continuations of these records from 5.3 to 40 million years ago based on the range between our process model main case and sensitivity test *i*. This range is reasonably consistent with other reconstructions, so it offers a useful template to guide further investigations. We emphasize that the uncertainty band does not represent an envelope for random variability. Instead, long-term inertia causes structured “drift” of the sea-level, deep-sea temperature, and δ_c records within the uncertainty band with typical time scales up to 10^7 years. Uncertainties in proxy-based reconstructions make it challenging for such work to differentiate where “reality” lies within the presented uncertainty band. It may be more promising to approach this issue across the entire 40 million years by better quantifying the controlling processes using 3D ice models with realistic ice-climate-ocean-topography-lithosphere coupling, including validation through like-for-like comparison between forward-modeled and observed proxy data. Due to current computational limitations, however, simplified and/or parameterized approaches will be useful, such as the process modeling approach used here. We have indicated several aspects that require improvement to reduce assumptions and caveats in such approaches.

All methods in our assessment that explicitly or implicitly account for parameter interdependences find similar ranges of 25-45 m sea-level change across the EOT (DeConto and Pollard, 2003; de Boer et al., 2010; Hansen et al., 2013; and our main scenario and sensitivity test *i*). This agreement extends to the associated δ_w shift, which spans a 0.3-0.5 ‰ range among the studies. However, RSL interpretations for the EOT infer greater sea-level drops; this discrepancy requires attention in further research. Our assessment flags a specific need for uncertainty estimates in RSL studies and in the required RSL-to-GMSL corrections for tectonic movements, dynamic topography, and GIA.

We observe a pattern of progressive glacial deep-sea temperature lowering through the Plio-Pleistocene that reflects the approach to a freezing limit from ~1.25 Ma, and definitely after 0.9 Ma. This non-linear, asymptoting glacial temperature behavior implies that a greater proportion of glacial deep-sea cooling occurred at earlier stages than at later stages. Glacial sea-level minima, in contrast, stepped down more evenly through time. These well-defined stepped patterns with different temporal proportionalities are not reproduced in recent climate model simulations (e.g., Willeit et al., 2019). This suggests that such

1749 simulations (*a*) may need to pay attention to threshold-style behavior (e.g., related to sea
1750 ice); or (*b*) may be missing hitherto unidentified driving processes.

1751

Acknowledgements

This study was supported by Australian Research Council Discovery Project DP200101157 (E.J.R., G.L.F., and D.H.) and SR200100008, the ARC Australian Centre for Excellence in Antarctic Science (E.J.R. and D.H.). We thank Brad Opdyke for critical discussions. R scripts for the process model are available via links listed following reference [Rohling et al. \(2021\)](#) at <http://www.highstand.org/erohling/ejrhme.htm#2021>

Data Availability Statement

New data from the process model and sensitivity tests are given in the **Excel “Data summary sheet Rohling et al.xlsx” included with this submission**, and will be archived upon acceptance at both <http://www.highstand.org/erohling/ejrhme.htm> and at the NOAA National Centres for Environmental Information Paleoclimatology collection (<https://www.ncei.noaa.gov/products/paleoclimatology>). Replotted datasets from previous publications can be obtained directly from their archived locations using the references provided.

Table 1. Age tie-points used in this study for chronological fine-tuning of the [Westerhold et al \(2020\)](#) and [Lisiecki and Raymo \(2005\)](#) based records, as discussed in the main text.

Westerhold et al. (2020)			Lisiecki and Raymo (2005)		
Original age (ka)	Tuned age (ka)	Tuned–Orig.	Original age (ka)	Tuned age (ka)	Tuned–Orig.
0.0	0.0	0.0	0.0	0.0	0.0
-7.0	-9.3	-2.3	-14.0	-9.2	4.8
-12.0	-14.3	-2.3	-20.0	-14.9	5.1
-25.0	-29.6	-4.6	-29.0	-31.8	-2.8
-58.0	-62.3	-4.3	-40.0	-36.0	4.0
-69.0	-71.4	-2.4	-48.0	-44.8	3.2
-122.0	-116.5	5.5	-58.0	-60.4	-2.4
-130.0	-129.5	0.5	-72.0	-71.8	0.3
-133.0	-136.8	-3.8	-88.0	-88.1	-0.1
-168.0	-174.0	-6.0	-94.0	-97.3	-3.3
-223.0	-220.0	3.0	-106.0	-107.5	-1.5
-299.0	-300.4	-1.4	-134.0	-135.1	-1.1
-340.0	-336.5	3.5	-166.0	-165.9	0.1
-412.0	-413.2	-1.2	-201.0	-198.0	3.0
-424.0	-437.0	-13.0	-222.0	-220.8	1.2
-488.0	-487.0	1.0	-241.0	-240.0	1.0
-556.0	-555.5	0.5	-254.0	-250.6	3.4
-566.0	-560.0	6.0	-297.0	-298.9	-1.9
-578.0	-577.6	0.4	-330.0	-329.8	0.3
-632.0	-632.0	0.0	-350.0	-345.4	4.6
-713.0	-710.0	3.0	-362.0	-357.3	4.8
-792.0	-792.0	0.0	-411.0	-406.0	5.0
-1782.0	-1782.0	0.0	-435.0	-430.0	5.0
-1840.0	-1863.0	-23.0	-445.0	-443.9	1.1
-1899.0	-1899.0	0.0	-488.0	-479.0	9.0
-1989.0	-1989.0	0.0	-538.0	-527.0	11.0
-2024.0	-2009.0	15.0	-573.0	-556.2	16.8
-2038.0	-2038.0	0.0	-580.0	-574.5	5.5
-3047.0	-3047.0	0.0	-699.0	-695.0	4.0
-3139.0	-3107.0	32.0	-713.0	-717.2	-4.2
-3249.0	-3249.0	0.0	-734.0	-738.0	-4.0
-3321.0	-3310.0	11.0	-799.0	-794.0	5.0
-3871.0	-3878.0	-7.0	-811.0	-811.0	0.0
-3924.0	-3921.2	2.8			
-4136.0	-4136.0	0.0			
-4157.0	-4179.0	-22.0			
-4310.0	-4317.0	-7.0			
-4412.0	-4388.0	24.0			
-4652.0	-4668.0	-16.0			
-4735.0	-4739.0	-4.0			
-4890.0	-4890.0	0.0			
-4935.0	-4949.5	-14.5			
-4989.0	-4988.0	1.0			
-5217.0	-5209.0	8.0			
-5300.0	-5300.0	0.0			

SUPPLEMENT

A. Minor corrections to the process model

In the description of the model in Rohling et al. (2021), minor errors caused small offsets between the ice-volume budget and the amount of sea-level change. These errors have been corrected in the R scripts used in this study.

For their equation (5), Rohling et al. (2021) wrote:

$$V_{AIS_j} = \begin{cases} 57.8 + \frac{-\Delta_{SLj}}{2} & \text{if } 0 < 7.3 + \frac{-\Delta_{SLj}}{2} \leq 7.3 \\ 57.8 - \Delta_{SLj} & \text{if } 7.3 < \Delta_{SLj} \leq 57.8 \\ 0 & \text{if } 57.8 < \Delta_{SLj} \\ V_{AIS_{j-1}} + \frac{-z_{min}}{125} 15 \left(\frac{-\Delta_{SLj}}{z_{min}} \right)^2 & \text{otherwise.} \end{cases}$$

This is corrected here to:

$$V_{AIS_j} = \begin{cases} 57.8 + \frac{-\Delta_{SLj}}{2} & \text{if } 0 < 7.3 + \frac{-\Delta_{SLj}}{2} \leq 7.3 \\ 65.1 - \Delta_{SLj} & \text{if } (2 \times 7.3) < \Delta_{SLj} \leq 65.1 \\ 0 & \text{if } 65.1 < \Delta_{SLj} \\ 57.8 + \frac{-z_{min}}{125} 15 \left(\frac{-\Delta_{SLj}}{z_{min}} \right)^2 & \text{otherwise.} \end{cases}$$

For their equation (6), Rohling et al. (2021) wrote:

$$V_{GrIS_j} = \begin{cases} 7.3 + \frac{-\Delta_{SLj}}{2} & \text{if } 0 < 7.3 + \frac{-\Delta_{SLj}}{2} \leq 7.3 \\ 0 & \text{if } 7.3 + \frac{-\Delta_{SLj}}{2} \leq 0 \\ V_{GrIS_{j-1}} + \left(\frac{-z_{min}}{125} 5 \frac{-\Delta_{SLj}}{z_{min}} \right) & \text{otherwise.} \end{cases}$$

This is corrected here to:

$$V_{GrIS_j} = \begin{cases} 7.3 + \frac{-\Delta_{SLj}}{2} & \text{if } 0 < 7.3 + \frac{-\Delta_{SLj}}{2} \leq 7.3 \\ 0 & \text{if } 7.3 + \frac{-\Delta_{SLj}}{2} \leq 0 \\ 7.3 + \left(\frac{-z_{min}}{125} 5 \frac{-\Delta_{SLj}}{z_{min}} \right) & \text{otherwise.} \end{cases}$$

B. Illustration of long-term controls on sampling the sea-level uncertainty envelope

In the following, we provide an illustrative example (not a precise sea-level reconstruction) of the impacts of long-term (up to 10^7 -year) inertia in AIS state variations on a resultant sea-level realization within the uncertainty envelope between our main scenario and sensitivity test i (i.e., the blue interval in Figure 18a). For this illustration, we identify order- 10^7 -year variability in the main-scenario sea-level record using a cubic smoothing spline from the

base-R function *smooth.spline*(t, z_{SL}, df) with $df = 9$ (Figure S3). We then determine the signs of the time derivatives of the spline, which we use to select which sea-level increment to use per kilo-year time step: when the spline value is >0 m with a derivative <0 m ky^{-1} , we obtain the sea-level increment for that time step from the perturbed $\Delta\delta_c:\Delta z_{SL}$ relationship (blue in Figure 18d); in all other cases, we obtain the sea-level increment for that time step from the main-scenario $\Delta\delta_c:\Delta z_{SL}$ relationship (gray in Figure 18d). Thus, we use the spline to approximate long-term inertia in AIS state variations when sampling through the uncertainty interval. Then, we start with an initial sea level of 65.1 m at 40 Ma, and for each time-step add selected sea-level increments to build a cumulative record from 40 Ma to present. This results in the sea-level record plotted in Figure S3a (black) against a background (blue) of the range between our main-scenario and sensitivity test i . This illustrates how the structure of variations within the uncertainty range is a function of long-term AIS “inertia”. In Figure S3b, we show how taking long-term inertia into account complicates $\Delta\delta_c:\Delta z_{SL}$. This is a purely hypothetical illustration of the nature of uncertainties represented by the blue band. These uncertainties are not random; instead, any record plotted through this uncertainty space will be organized through time.

REFERENCES

- Abbate, E., & Sagri, M. (2012). Early to Middle Pleistocene *Homo* dispersals from Africa to Eurasia: Geological, climatic and environmental constraints. *Quaternary International*, 267, 3–19.
- Abdul, N. A., Mortlock, R. A., Wright, J. D., & Fairbanks, R. G. (2016). Younger Dryas sea level and meltwater pulse 1B recorded in Barbados reef crest coral *Acropora palmata*. *Paleoceanography*, 31, 330–344.
- Adeleye, M. A., Haberle, S. G., McWethy, D., Connor, S. E., & Stevenson, J. (2021). Environmental change during the last glacial on an ancient land bridge of southeast Australia. *Journal of Biogeography*, 48, 2946–2960.
- Adkins, J. F., McIntyre, K., & Schrag, D. P. (2002). The salinity, temperature, and $\delta^{18}\text{O}$ of the glacial deep ocean. *Science*, 298, 1769–1773.
- Aharon, P. (1983). 140,000-yr isotope climatic record from raised coral reef in New Guinea. *Nature*, 304, 720–723.
- Ahn, S., Khider, D., Lisiecki, L. E., & Lawrence, C. E. (2017). A probabilistic Pliocene–Pleistocene stack of benthic $\delta^{18}\text{O}$ using a profile hidden Markov model. *Dynamics and Statistics of the Climate System*, 2, dzx002.
- Almogi-Labin, A., Hemleben, C., Meischner, D., & Erlenkeuser, H. (1991). Paleoenvironmental events during the last 13,000 years in the central Red Sea as recorded by pteropoda. *Paleoceanography* 6, 83–98.
- Amies, J. D., Rohling, E. J., Grant, K. M., Rodríguez-Sanz, L., & Marino, G. (2019). Quantification of African monsoon runoff during last interglacial sapropel S5. *Paleoceanography and Paleoclimatology*, 34, 1487–1516.
- Andersen, M. B., Stirling, C., Potter, E.-K., Halliday, A. N., Blake, S. G., McCulloch, M. T., Ayling, B. F., & O’Leary, M. (2008). High-precision U-series measurements of more than 500,000 year old fossil corals. *Earth and Planetary Science Letters*, 265, 229–245.
- Andersen, M. B., Stirling, C., Potter, E.-K., Halliday, A. N., Blake, S. G., McCulloch, M. T., Ayling, B. F., & O’Leary, M. (2010). The timing of sea-level high-stands during Marine Isotope Stages 7.5 and 9: Constraints from the uranium-series dating of fossil corals from Henderson Island. *Geochimica et Cosmochimica Acta*, 74, 3598–3620.
- Anderson, H. J., Pedro, J. B., Bostock, H. C., Chase, Z., & Noble, T. L. (2021). Compiled Southern Ocean sea surface temperatures correlate with Antarctic Isotope Maxima. *Quaternary Science Reviews*, 255, 106821.
- Antonioli, F., Anzidei, M., Lambeck, K., Auriemma, R., Gaddi, D., Furlani, S., Orrù, P., Solinas, E., Gaspari, A., Karinja, S., Kovačić, V., & Surace, L. (2007). Sea level change during Holocene from Sardinia and northeastern Adriatic (central Mediterranean Sea) from archaeological and geomorphological data. *Quaternary Science Reviews*, 26, 2463–2486.
- Antonioli, F., Bard, E., Potter, E.-K., Silenzi, S., & Imbrota, S. (2004). 215-ka History of sea-level oscillations from marine and continental layers in Argenterola Cave speleothems (Italy). *Global and Planetary Change*, 43, 57–78.
- Armitage, S. J., Jasim, S. A., Marks, A. E., Parker, A. G., Usik, V. I., & Uerpmann, H. P. (2011). The southern route “out of Africa”: Evidence for an early expansion of modern humans into Arabia. *Science*, 331, 453–456.
- Austermann, J., Mitrovica, J. X., Huybers, P., & Rovere, A. (2017). Detection of a dynamic topography signal in last interglacial sea-level records. *Science Advances*, 3, e1700457.

- Ayling, B. F., McCulloch, M. T., Gagan, M. K., Stirling, C. H., Andersen, M. B., & Blake, S. G. (2006). Sr/Ca and $\delta^{18}\text{O}$ seasonality in a *Porites* coral from the MIS 9 (339–303 ka) interglacial. *Earth and Planetary Science Letters*, 248, 462–475.
- Bailey, G. (2010). The Red Sea, coastal landscapes, and hominin dispersals. In: *The evolution of human populations in Arabia* (pp. 15–37). Springer, Dordrecht.
- Bailey, I., Hole, G. M., Foster, G. L., Wilson, P. A., Storey, C. D., Trueman, C. N., & Raymo, M. E. (2013). An alternative suggestion for the Pliocene onset of major Northern Hemisphere glaciation based on the geochemical provenance of North Atlantic Ocean ice-rafted debris. *Quaternary Science Reviews*, 75, 181–194.
- Bamber, J. L., Ekholm, S., & Krabill, W. B. (2001). A new, high-resolution digital elevation model of Greenland fully validated with airborne laser altimeter data. *Journal of Geophysical Research*, 106, 6733–6745.
- Bamber, J. L., Oppenheimer, M., Kopp, R. E., Aspinall, W., & Cooke, R. M. (2019). Ice sheet contributions to future sea level rise from structured expert judgement. *Proceedings of the National Academy of Sciences of the USA*, 116, 11195–11200.
- Bard, E., Antonioli, F., & Silenzi, S. (2002). Sea level during the penultimate interglacial period based on a submerged stalagmite from Argenterola Cave, Italy. *Earth and Planetary Science Letters*, 196, 135–146.
- Bard, E., Fairbanks, R. G., Hamelin, B., Zindler, A., & Hoang, C. T. (1991). Uranium-234 anomalies in corals older than 150,000 years. *Geochimica et Cosmochimica Acta*, 55, 2385–2390.
- Bard, E., Hamelin, B., & Fairbanks, R. G. (1990a). U-Th ages obtained by mass spectrometry in corals from Barbados: sea level during the past 130000 years. *Nature*, 346, 456–458.
- Bard, E., Hamelin, B., Fairbanks, R. G., & Zindler, A. (1990b). Calibration of the ^{14}C timescale over the past 30000 years using mass spectrometric U-Th ages from Barbados corals. *Nature*, 345, 405–410.
- Bard, E., Hamelin, B., Fairbanks, R. G., Zindler, A., Arnold, M., & Mathieu, G. (1990c). U/Th and ^{14}C ages of corals from Barbados and their use for calibrating the ^{14}C timescale beyond 9000 years BP. *Nuclear Instruments and Methods B*, 52, 461–468.
- Bard, E., Hamelin, B., & Delanghe-Sabatier, D. (2010). Deglacial Meltwater Pulse 1B and Younger Dryas sea levels revisited with boreholes at Tahiti. *Science*, 327, 1235–1237.
- Bard, E., Hamelin, B., Arnold, M., Montaggioni, L., Cabioch, G., Faure, G., & Rougerie, F. (1996a). Deglacial sea-level record from Tahiti corals and the timing of global meltwater discharge. *Nature*, 382, 241–244.
- Bard, E., Jouannic, C., Hamelin, B., Pirazzoli, P., Arnold, M., Faure, G., & Sumosusastro, P. (1996b). Pleistocene sea levels and tectonic uplift based on dating of corals from Sumba Island, Indonesia. *Geophysical Research Letters*, 23, 1473–1476.
- Barrientos, N., Lear, C. H., Jakobsson, M., Stranne, C., O'Regan, M., Cronin, T. M., Gukov, A.Y., & Coxall, H. K. (2018). Arctic Ocean benthic foraminifera Mg/Ca ratios and global Mg/Ca-temperature calibrations: New constraints at low temperatures. *Geochimica et Cosmochimica Acta*, 236, 240–259.
- Barry, S., Cowell, P. J., & Woodroffe, C. D. (2008). Growth-limiting size of atoll-islets: Morphodynamics in nature. *Marine Geology*, 247, 159–177.
- Bassett, S. E., Milne, G. A., Mitrovica, J. X., & Clark, P. U. (2005). Ice sheet and solid earth influences on far-field sea-level histories. *Science*, 309, 925–928.

- Bassinot, F., Labeyrie, L., Vincent, E., Quidelleur, X., Shackleton, N., & Lancelot, Y. (1994). The astronomical theory of climate and the age of the Brunhes-Matuyama magnetic reversal. *Earth and Planetary Science Letters*, 126, 91–108.
- Bates, S. L., Siddall, M., & Waelbroeck, C. (2014). Hydrographic variations in deep ocean temperature over the mid-Pleistocene transition. *Quaternary Science Reviews*, 88, 147–158.
- Bender, M. L., Barnett, B., Dreyfus, G., Jouzel, J., & Porcelli, D. (2019). The contemporary degassing rate of ^{40}Ar from the solid Earth. *Proceedings of the National Academy of Sciences of the USA*, 105, 8232–8237.
- Bereiter, B., Shackleton, S., Baggenstos, D., Kawamura, K., & Severinghaus, J. (2018). Mean global ocean temperatures during the last glacial transition. *Nature*, 553, 39–44.
- Berends, C. J., de Boer, B., & van de Wal, R. S. W. (2018). Application of HadCM3@Bristolv1.0 simulations of paleoclimate as forcing for an ice-sheet model, ANICE2.1: Set-up and benchmark experiments. *Geoscientific Model Development*, 11, 4657–4675.
- Berends, C. J., de Boer, B., Dolan, A. M., Hill, D. J., & van de Wal, R. S. W. (2019). Modelling ice sheet evolution and atmospheric CO_2 during the Late Pliocene. *Climate of the Past*, 15, 1603–1619.
- Berends, C. J., de Boer, B., & van de Wal, R. S. W. (2021a). Reconstructing the evolution of ice sheets, sea level, and atmospheric CO_2 during the past 3.6 million years. *Climate of the Past*, 17, 361–377.
- Berends, C. J., Köhler, P., Lourens, L. J., & van de Wal, R. S. W. (2021b). On the cause of the Mid-Pleistocene Transition. *Reviews of Geophysics*, 59, e2020RG000727.
- Berger, A. (1978). Long-term variations of caloric insolation resulting from the Earth's orbital elements. *Quaternary Research*, 9, 139–167.
- Berger, A., & Loutre, M. F. (1991). Insolation values for the climate of the last 10 million years. *Quaternary Science Reviews*, 10, 297–317.
- Berger, A., & Loutre, M. F. (1992). Astronomical solutions for paleoclimate studies over the last 3 million years. *Earth and Planetary Science Letters*, 111, 369–382.
- Berger, A., Li, X. S., & Loutre, M. F. (1999). Modelling Northern Hemisphere ice volume over the last 3Ma. *Quaternary Science Reviews*, 18, 1–11.
- Bernasconi, S. M., Schmid, T. W., Grauel, A.-L., & Mutterlose, J. (2011). Clumped-isotope geochemistry of carbonates: A new tool for the reconstruction of temperature and oxygen isotope composition of seawater. *Applied Geochemistry*, 26(Supplement), S279–S280.
- Bintanja, R., & van de Wal, R. S. W. (2008). North American ice-sheet dynamics and the onset of 100,000-year glacial cycles. *Nature*, 454, 869–872.
- Bintanja, R., van de Wal, R. S. W., & Oerlemans, J. (2005). Modelled atmospheric temperatures and global sea level over the past million years. *Nature*, 437, 125–128.
- Biton, E., Gildor, H., & Peltier, W. R. (2008). Red Sea during the Last Glacial Maximum: Implications for sea level reconstruction. *Paleoceanography*, 23, PA1214.
- Blake-Mizen, K., Hatfield, R. G., Stoner, J. S., Carlson, A. E., Xuan, C., Walczak, M., Lawrence, K. T., Channell, J. E. T., & Bailey, I. (2019). Southern Greenland glaciation and Western Boundary Undercurrent evolution recorded on Eirik Drift during the late Pliocene intensification of Northern Hemisphere glaciation. *Quaternary Science Reviews*, 209, 40–51.
- Blanchon, P., & Eisenhauer, A. (2000). Multi-stage reef development on Barbados during the Last Interglaciation. *Quaternary Science Reviews*, 20, 1093–1112.

- Blanchon, P., Eisenhauer, A., Fietzke, J., & Liebetrau, V. (2009). Rapid sea-level rise and reef back-stepping at the close of the last interglacial highstand. *Nature*, *458*, 881–884.
- Blanchon, P., Jones, B., & Ford, D. C. (2002). Discovery of a submerged relic reef and shoreline off Grand Cayman: Further support for an early Holocene jump in sea level. *Sedimentary Geology*, *147*, 253–270.
- Boettner, C., Klinghammer, G., Boers, N., Westerhold, T., & Marwan, N. (2021). Early-warning signals for Cenozoic climate transitions. *Quaternary Science Reviews*, *270*, 107177.
- Braithwaite, C. J. R. (2016). Coral-reef records of Quaternary changes in climate and sea-level. *Earth-Science Reviews*, *156*, 137–154.
- Braun, J. (2010). The many surface expressions of mantle dynamics. *Nature Geoscience*, *3*, 825–833.
- Broccoli, A. J. (2000). Tropical cooling at the Last Glacial Maximum: An atmosphere–mixed layer ocean model simulation. *Journal of Climate*, *13*, 951–976.
- Broccoli, A. J., & Manabe, S. (1987). The influence of continental ice, atmospheric CO₂, and land albedo on the climate of the last glacial maximum. *Climate Dynamics*, *1*, 87–99.
- Broecker, W. S. (1975). Floating glacial ice caps in the Arctic Ocean. *Science*, *188*, 1116–1118.
- Bryden, H. L., & Kinder, T. H. (1991). Steady two-layer exchange through the Strait of Gibraltar. *Deep-Sea Research*, *38*, S445–S463.
- Bryden, H. L., Candela, J., & Kinder, T. H. (1994). Exchange through the Strait of Gibraltar. *Progress in Oceanography*, *33*, 201–248.
- Cabioch, G., Banks-Cutler, K. A., Beck, W. J., Burr, G. S., Corrège, T., Edwards, R. L., & Taylor, F. W. (2003). Continuous reef growth during the last 23 cal kyr BP in a tectonically active zone (Vanuatu, SouthWest Pacific). *Quaternary Science Reviews*, *22*, 1771–1786.
- Cabioch, G., Montaggioni, L., Frank, N., Seard, C., Sallé, E., Payri, C., Pelletier, B., & Paterne, M. (2008). Successive reef depositional events along the Marquesas foreslopes (French Polynesia) since 26 ka. *Marine Geology*, *254*, 18–34.
- Camoin, G. F., Colonna, M., Montaggioni, L. F., Casanova, J., Faure, G., & Thomassin, B. A. (1997). Holocene sea level changes and reef development in the southwestern Indian Ocean. *Coral Reefs*, *16*, 247–259.
- Camoin, G. F., Ebren, P., Eisenhauer, A., Bard, E., & Faure, G. (2001). A 300 000-yr coral reef record of sea level changes, Mururoa atoll (Tuamotu archipelago, French Polynesia). *Palaeogeography, Palaeoclimatology, Palaeoecology*, *175*, 325–341.
- Camoin, G. F., Montaggioni, L. F., & Braithwaite, C. J. R. (2004). Late glacial to post glacial sea levels in the Western Indian Ocean. *Marine Geology*, *206*, 119–146.
- Carlson, A. E. (2011). Ice sheets and sea level in Earth's past. *Nature Education Knowledge*, *3*, 3.
- Carlson, A. E., & Clark, P. U. (2012). Ice sheet sources of sea level rise and freshwater discharge during the last deglaciation. *Reviews of Geophysics*, *50*, RG4007
- Chalk, T. B., Hain, M. P., Foster, G. L., Rohling, E. J., Sexton, P. F., Badger, M. P. S., Cherry, S. G., Hasenfratz, A. P., Haug, G. H., Jaccard, S. L., Martínez-García, A., Pälike, H., Pancost, R. D., & Wilson, P. A. (2017). Causes of ice-age intensification across the Mid-Pleistocene Transition. *Proceedings of the National Academy of Sciences of the USA*, *114*, 13114–13119.
- Chappell, J. (2002). Sea-level changes forced ice breakouts in the last glacial cycle: New results from coral terraces. *Quaternary Science Reviews*, *21*, 1229–1240.
- Chappell, J., & Shackleton, N. J. (1986). Oxygen isotopes and sea level. *Nature*, *324*, 137–140.

- Chappell, J., Omura, A., Ezat, T., McCulloch, M., Pandolfi, J., Ota, Y., & Pillans, B. (1996). Reconciliation of late Quaternary sea levels derived from coral terraces at Huon Peninsula with deep-sea oxygen isotope records. *Earth and Planetary Science Letters*, 141, 227–236.
- Chen, J. H., Curran, H. A., White, B., & Wasserburg, G. J. (1991). Precise chronology of the last interglacial period: ^{234}U - ^{230}Th data from fossil coral reefs in the Bahamas. *Geological Society of America Bulletin*, 103, 82–97.
- Chiu, T. C., Fairbanks, R. G., Mortlock, R. A., & Bloom, A. L. (2005). Extending the radiocarbon calibration beyond 26,000 years before present using fossil corals. *Quaternary Science Reviews*, 24, 1797–1808.
- Clark, J. A., Farrell, W. E., & Peltier, W. R. (1978). Global changes in postglacial sea level: A numerical calculation. *Quaternary Research*, 9, 265–287.
- Clark, P. U., & Pollard, D. (1998). Origin of the Middle Pleistocene Transition by ice sheet erosion of regolith. *Paleoceanography*, 13, 1–9.
- Clark, P. U., Archer, D., Pollard, D., Blum, J. D., Rial, J. A., Brovkin, V., Mix, A. C., Piasias, N. G., & Roy, M. (2006). The middle Pleistocene transition: Characteristics, mechanisms, and implications for long-term changes in atmospheric pCO_2 . *Quaternary Science Reviews*, 25, 3150–3184.
- Clark, P. U., Dyke, A., Shakun, J. D., Carlson, A. E., Clark, J., Wohlfarth, B., Mitrovica, J. X., Hostetler, S. W., & McCabe, M. (2009). The last glacial maximum. *Science*, 325, 710–714.
- Clark, P. U., Shakun, J. D., Marcott, S. A., Mix, A. C., Eby, M., Kulp, S., Levermann, A., Milne, G. A., Pfister, P. L., Santer, B. D., Schrag, D. P., Solomon, S., Stocker, T. F., Strauss, B. H., Weaver, A. J., Winkelmann, R., Archer, D., Bard, E., Goldner, A., Lambeck, K., Pierrehumbert, R. T., & Plattner, G.-K. (2016). Consequences of twenty-first-century policy for multi-millennial climate and sea-level change. *Nature Climate Change*, 6, 360–369.
- Coggon, R. M., Teagle, D. A., Smith-Duque, C. E., Alt, J. C., & Cooper, M. J. (2010). Reconstructing past seawater Mg/Ca and Sr/Ca from mid-ocean ridge flank calcium carbonate veins. *Science*, 327, 1114–1117.
- Colleoni, F., De Santis, L., Montoli, E., Olivo, E., Sorlien, C. C., Bart, P. J., Gasson, E. G. W., Bergamasco, A., Sauli, C., Wardell, N., & Prato, S. (2018). Past continental shelf evolution increased Antarctic ice sheet sensitivity to climatic conditions. *Scientific Reports*, 8, 1–12.
- Collins, L. B., Zhao, J. X., & Freeman, H. (2006). A high-precision record of mid-late Holocene sea-level events from emergent coral pavements in the Houtman Abrolhos Islands, southwest Australia. *Quaternary International*, 145, 78–85.
- Colonna, M., Casanova, J., Dullo, W. C., & Camoin, G. (1996). Sea-level changes and $\delta^{18}\text{O}$ record for the past 34,000 yr from Mayotte Reef, Indian Ocean. *Quaternary Research*, 46, 335–339.
- Conrad, C. P. (2013). The solid Earth's influence on sea level. *GSA Bulletin*, 125, 1027–1052.
- Coyne, M. K., Jones, B., & Ford, D. (2007). Highstands during marine isotope stage 5: Evidence from the Ironshore Formation of Grand Cayman, British West Indies. *Quaternary Science Reviews*, 26, 536–559.
- Cramer, B. S., Miller, K. G., Barrett, P. J., & Wright, J. D. (2011). Late Cretaceous-Neogene trends in deep ocean temperature and continental ice volume: Reconciling records of benthic foraminiferal geochemistry ($\delta^{18}\text{O}$ and Mg/Ca) with sea level history. *Journal of Geophysical Research: Oceans*, 116, C12023.
- Creveling, J. R., Mitrovica, J. X., Hay, C. C., Austermann, J., & Kopp, R. E. (2015). Revisiting tectonic corrections applied to Pleistocene sea-level highstands. *Quaternary Science Reviews*, 111, 72–80.

- Cuffey, K. M. (2000). Methodology for use of isotope forcings in ice sheet models. *Geophysical Research Letters*, 27, 3065–3068.
- Cutler, K. B., Edwards, R. L., Taylor, F. W., Cheng, H., Adkins, J., Gallup, C. D., Cutler, P. M., Burr, G. S., & Bloom, A. L. (2003). Rapid sea level fall and deep ocean temperature change since the last interglacial period. *Earth and Planetary Science Letters*, 206, 253–271.
- Cutler, K. B., Gray, S. C., Burr, G. S., Edwards, R. L., Taylor, F. W., Cabioch, G., Beck, J. W., Cheng, H., & Moor, J. (2004). Radiocarbon calibration and comparison to 50 kyr BP with paired ^{14}C and ^{230}Th dating of corals from Vanuatu and Papua New Guinea. *Radiocarbon*, 46, 1127–1160.
- Dabrio, C. J., Zazo, C., Cabero, A., Goy, J. L., Bardají, T., Hillaire-Marcel, C., González-Delgado, J. A., Lario, J., Silva, P. G., Borja, F., & García-Blázquez, A. M. (2011). Millennial/submillennial scale sea-level fluctuations in western Mediterranean during the second highstand of MIS 5e. *Quaternary Science Reviews*, 30, 335–346.
- Dansgaard, W. (1964). Stable isotopes in precipitation. *Tellus*, 16, 436–468.
- de Boer, B., Lourens, L. J., & van de Wal, R. S. W. (2014). Persistent 400,000-year variability of Antarctic ice volume and the carbon cycle is revealed throughout the Plio-Pleistocene, *Nature Communications*, 5, 2999.
- de Boer, B., van de Wal, R. S. W., Bintanja, R., Lourens, L. J., & Tuenner, E. (2010). Cenozoic global ice-volume and temperature simulations with 1-D ice-sheet models forced by benthic $\delta^{18}\text{O}$ records. *Annals of Glaciology*, 51, 23–33.
- de Boer, B., van de Wal, R. S. W., Lourens, L. J., Bintanja, R., & Reerink, T. J. (2013). A continuous simulation of global ice volume over the past 1 million years with 3-D ice-sheet models, *Climate Dynamics*, 41, 1365–1384.
- de Boer, B., Haywood, A. M., Dolan, A. M., Hunter, S. J., & Prescott, C. L. (2017). The transient response of ice volume to orbital forcing during the warm late Pliocene. *Geophysical Research Letters*, 44, 10486–10494.
- Deschamps, P., Durand, N., Bard, E., Hamelin, B., Camoin, G., Thomas, A. L., Henderson, G. M., Okuno, J., & Yokoyama, Y. (2012). Ice-sheet collapse and sea-level rise at the Bølling warming 14600 years age. *Nature*, 483, 559–564.
- DeConto, R. M., & Pollard, D. (2003). Rapid Cenozoic glaciation of Antarctica induced by declining atmospheric CO_2 . *Nature*, 421, 245–249.
- DeConto, R. M., & Pollard, D. (2016). Contribution of Antarctica to past and future sea-level rise. *Nature*, 531, 591–597.
- DeConto, R. M., Pollard, D., Alley, R. B., Vellicogna, I., Gasson, E., Gomez, N., Sadai, S., Condrón, A., Gilford, D. M., Ashe, E. L., Kopp, R. E., Li, D., & Dutton, A. (2021). The Paris Climate Agreement and future sea-level rise from Antarctica. *Nature*, 593, 83–89.
- DeConto, R. M., Pollard, D., Wilson, P. A., Pälike, H., Lear, C. H., & Pagani, M. (2008). Thresholds for Cenozoic bipolar glaciation. *Nature*, 455, 652–656.
- Dendy, S., Austermann, J., Creveling, J. R., & Mitrovica, J. X. (2017). Sensitivity of Last Interglacial sea-level high stands to ice sheet configuration during Marine Isotope Stage 6. *Quaternary Science Reviews*, 171, 234–244.
- Deuser, W. G., Ross, E. H., & Waterman, L. S. (1976). Glacial and pluvial periods: Their relationship revealed by Pleistocene sediments of the Red Sea and Gulf of Aden. *Science*, 191, 1168–1170.

- De Vleeschouwer, D., Vahlenkamp, M., Crucifix, M., & Pälike, H. (2017). Alternating Southern and Northern Hemisphere climate response to astronomical forcing during the past 35 m.y. *Geology*, *45*, 375–378.
- Dia, A. N., Cohen, A. S., O'Nions, R. K., & Jackson, J. A. (1997). Rates of uplift investigated through ^{230}Th dating in the Gulf of Corinth (Greece). *Chemical Geology*, *138*, 171–184.
- Dia, A. N., Cohen, A. S., O'Nions, R. K., & Shackleton, N. J. (1992). Seawater Sr isotope variation over the past 300 kyr and influence of global climate cycles. *Nature*, *356*, 786–788.
- Dorale, J. A., Onac, B. P., Fornós, J. J., Ginés, J., Ginés, A., Tuccimei, P., & Peate, D. W. (2010). Sea-level highstand 81,000 years ago in Mallorca. *Science*, *327*, 860–863.
- Doyle, S. H., Hubbard, A., Van De Wal, R. S., Box, J. E., Van As, D., Scharrer, K., Meierbachtol., T. W., Smeets, P. C. J. P., Harper, J. T., Johansson, E., Mottram, R. H., Mikkelsen, A. B., Wilhelms, F., Patton, H., Christofferson, P., & Hubbard, B. (2015). Amplified melt and flow of the Greenland ice sheet driven by late-summer cyclonic rainfall. *Nature Geoscience*, *8*, 647–653.
- Dumitru, O. A., Austermann, J., Polyak, V. J., Fornós, J. J., Asmerom, Y., Ginés, J., Ginés, A., & Onac, B. P. (2019). Constraints on global mean sea level during Pliocene warmth. *Nature*, *574*, 233–236.
- Dumitru, O. A., Austermann, J., Polyak, V. J., Fornos, J. J., Asmerom, Y., Ginés, J., & Onac, B. P. (2021). Sea-level stands from the Western Mediterranean over the past 6.5 million years. *Scientific Reports*, *11*, 261.
- Duplessy, J. C., Moyes, J., & Pujol, C. (1980). Deep water formation in the North Atlantic Ocean during the last ice age. *Nature*, *286*, 479–481.
- Dutton, A., Webster, J. M., Zwartz, D., Lambeck, K., & Wohlfarth, B. (2015). Tropical tales of polar ice: Evidence of Last Interglacial polar ice sheet retreat recorded by fossil reefs of the granitic Seychelles islands. *Quaternary Science Reviews*, *107*, 182–196.
- Dutton, A., Villa, A., & Chutcharavan, P. M. (2022). Compilation of Last Interglacial (Marine Isotope Stage 5e) sea level indicators in the Bahamas, Turks and Caicos, and the east coast of Florida, USA. *Earth System Science Data Discussion* [preprint], <https://doi.org/10.5194/essd-2021-391>, in review.
- Edwards, R. L., Beck, J. W., Burr, G. S., Donahue, D. J., Chappell, J. M. A., Bloom, A. L., Druffel, E. R. M., & Taylor, F. W. 1993. A large drop in atmospheric $^{14}\text{C}/^{12}\text{C}$ and reduced melting in the Younger Dryas, documented with ^{230}Th ages of corals. *Science*, *260*, 962–967.
- Edwards, R. L., Chen, J. H., Ku, T. L., & Wasserburg, G. J. (1987). Precise timing of the last interglacial period from mass spectrometric determination of thorium-230 in corals. *Science*, *236*, 1547–1553.
- Edwards, R. L., Cheng, H., Murrell, M. T., & Goldstein, S. J. (1997). Protactinium-231 dating of carbonates by thermal ionization mass spectrometry: Implications for Quaternary climate change. *Science*, *276*, 782–786.
- Eiler, J. M. (2007). “Clumped-isotope” geochemistry—The study of naturally-occurring, multiply-substituted isotopologues. *Earth and Planetary Science Letters*, *262*, 309–327.
- Eiler, J.M. (2011). Paleoclimate reconstruction using carbonate clumped isotope thermometry. *Quaternary Science Reviews*, *30*, 3575–3588.
- Eisenhauer, A., Wasserburg, G. J., Chen, J. H., Bonani, G., Collins, L. B., Zhu, Z. R., & Wyrwoll, K. H. (1993). Holocene sea-level determination relative to the Australian continent: U/Th (TIMS) and ^{14}C (AMS) dating of coral cores from the Abrolhos Islands. *Earth and Planetary Science Letters*, *114*, 529–547.

- Eisenhauer, A., Zhu, Z. R., Collins, L. B., Wyrwoll, K. H., & Eichstatter, R. (1996). The Last Interglacial sea level change: New evidence from the Abrolhos islands, West Australia. *Geologische Rundschau*, 85, 606–614.
- Elderfield, H., Bertram, C. J., & Erez, J. (1996). A biomineralization model for the incorporation of trace elements into foraminiferal calcium carbonate. *Earth and Planetary Science Letters*, 142, 409–423.
- Elderfield, H., Ferretti, P., Greaves, M., Crowhurst, S., McCave, I. N., Hodell, D., & Piotrowski, A. M. (2012). Evolution of ocean temperature and ice volume through the Mid-Pleistocene Climate Transition. *Science*, 337, 704–709.
- Elderfield, H., Greaves, M., Barker, S., Hall, I.R., Tripathi, A., Ferretti, P., Crowhurst, S., Booth, L., & Daunt, C. (2010). A record of bottom water temperature and seawater $\delta^{18}\text{O}$ for the Southern Ocean over the past 440 kyr based on Mg/Ca of benthic foraminiferal *Uvigerina* spp. *Quaternary Science Reviews*, 29, 160–169.
- Elias, S. A., Short, S. K., Nelson, C. H., & Birks, H. H. (1996). Life and times of the Bering land bridge. *Nature*, 382, 60–63.
- Emery, W. J., (2001). Water types and water masses. *Encyclopedia of Ocean Sciences*, 4, 3179–3187.
- Emiliani, C. (1955). Pleistocene temperatures. *The Journal of Geology*, 63, 538–577.
- Engelhart, S. E., & Horton, B. P. (2012). Holocene sea level database for the Atlantic coast of the United States. *Quaternary Science Reviews*, 54, 12–25.
- EPICA community members (2004). Eight glacial cycles from an Antarctic ice core. *Nature*, 429, 623–628.
- Epstein, S., Buchsbaum, R., Lowenstam, H. A., & Urey, H. C. (1951). Carbonate-water isotopic temperature scale. *Geological Society of America Bulletin*, 62, 417–426.
- Esat, T. M., McCulloch, M. T., Chappell, J., Pillans, B., & Omura, A. (1999). Rapid fluctuations in sea level recorded at Huon Peninsula during the penultimate deglaciation. *Science*, 283, 197–201.
- Etourneau, J., Schneider, R., Blanz, T., & Martinez, P. (2010). Intensification of the Walker and Hadley atmospheric circulations during the Pliocene–Pleistocene climate transition. *Earth and Planetary Science Letters*, 297, 103–110.
- Evans, D., & Muller, W. (2012). Deep time foraminifera Mg/Ca paleothermometry: Nonlinear correction for secular change in seawater Mg/Ca. *Paleoceanography and Paleoclimatology*, 27, PA4205.
- Evans, D., Sagoo, N., Renema, W., Cotton, L. J., Muller, W. J., Todd, A., Kumar Saraswati, P., Stassen, P., Ziegler, M., Pearson, P. N., Valdes, P. J., & Affek, H. P. (2018). Eocene greenhouse climate revealed by coupled clumped isotope-Mg/Ca thermometry. *Proceedings of the National Academy of Sciences of the USA*, 115, 1174–1179.
- Fairbanks, R. G. (1989). A 17,000 year glacio-eustatic sea level record: Influence of glacial melting rates on the Younger Dryas event and deep-ocean circulation. *Nature*, 342, 637–642.
- Fairbanks, R. G., & Matthews, R. K. (1978). The marine oxygen isotope record in Pleistocene coral, Barbados, West Indies. *Quaternary Research*, 10, 181–196.
- Fairbanks, R. G., Mortlock, R. A., Chiu, T.-C., Cao, L., Kaplan, A., Guilderson, T. P., Fairbanks, T. W., Bloom, A. L., Grootes, P. M., & Nadeau, M.-J. (2005). Radiocarbon calibration curve spanning 0 to 50,000 years BP based on paired $^{230}\text{Th}/^{234}\text{U}/^{238}\text{U}$ and ^{14}C dates on pristine corals. *Quaternary Science Reviews*, 24, 1781–1796.
- Fasullo, J. T., & Trenberth, K. E. (2008). The annual cycle of the energy budget. Part II: Meridional structures and poleward transports. *Journal of Climate*, 21, 2313–2325.

- Fenton, M., Geiselhart, S., Rohling, E. J., & Hemleben, C. (2000). Aplanktonic zones in the Red Sea. *Marine Micropaleontology*, 40, 277–294.
- Fernandes, C., Rohling, E. J., & Siddall, M. (2006). Absence of Quaternary Red Sea land bridges: Biogeographic implications. *Journal of Biogeography*, 33, 961–966.
- Ferrier, K. L., Austermann, J., Mitrovica, J. X., & Pico, T. (2017). Incorporating sediment compaction into a gravitationally self-consistent model for ice age sea-level change. *Geophysical Journal International*, 211, 663–672.
- Fischer, H., Meissner, K. J., Mix, A. C., Abram, N. J., Austermann, J., Brovkin, V., ... & Zhou, L. (2018). Palaeoclimate constraints on the impact of 2 °C anthropogenic warming and beyond. *Nature Geoscience*, 11, 474–485.
- Ford, H. L., & Raymo, M. E. (2019). Regional and global signals in seawater $\delta^{18}\text{O}$ records across the mid-Pleistocene transition. *Geology*, 48, 113–117.
- Foster, G. L., and Rohling, E. J. (2013). Relationship between sea level and climate forcing by CO_2 on geological timescales. *Proceedings of the National Academy of Sciences of the USA*, 110, 1209–1214.
- Frank, N., Turpin, L., Cabioch, G., Blamart, D., Tressens-Fedou, M., Colin, C., & Jean-Baptiste, P. (2006). Open system U-series ages of corals from a subsiding reef in New Caledonia: Implications for sea level changes, and subsidence rate. *Earth and Planetary Science Letters*, 249, 274–289.
- Fruijtier, C., Elliott, T., & Schlager, W. (2000). Mass-spectrometric ^{234}U - ^{230}Th ages from the Key Largo Formation, Florida Keys, United States: Constraints on diagenetic age disturbance. *Geological Society of America Bulletin*, 112, 267–277.
- Galewsky, J., Silver, E. A., Gallup, C. D., Edwards, R. L., & Potts, D. C. (1996). Foredeep tectonics and carbonate platform dynamics in the Huon Gulf, Papua New Guinea. *Geology*, 24, 819–822.
- Gallup, C. D., Cheng, H., Taylor, F. W., & Edwards, R. L. (2002). Direct determination of the timing of sea level change during Termination II. *Science*, 295, 310–313.
- Gallup, C. D., Edwards, R. L., & Johnson, R. (1994). The timing of high sea levels over the past 200,000 years. *Science*, 263, 796–800.
- Ganopolski, A., & Calov, R. (2011). The role of orbital forcing, carbon dioxide and regolith in 100 kyr glacial cycles. *Climate of the Past*, 7, 1415–1425.
- Garlick, G. D. (1974). The stable isotopes of oxygen, carbon, hydrogen in the marine environment. In: Goldberg, E.D. (Ed.), *The Sea*, Vol. 5. John Wiley & Sons, New York, pp. 393–425.
- Gasson, E. (2013). The past relationship between temperature and sea level - from proxy records and ice sheet modeling. PhD thesis, University of Bristol, Bristol, UK, 250 pp.
- Gasson, E., & Kiesling, B. (2020). The Antarctic ice sheet, a paleoclimate perspective. *Oceanography*, 33, 90–100.
- Gasson, E., DeConto, R. M., Pollard, D., & Levy, R. H. (2016). Dynamic Antarctic ice sheet during the early to mid-Miocene. *Proceedings of the National Academy of Sciences of the USA*, 113, 3459–3464.
- Gasson, E., Siddall, M., Lunt, D. J., Rackham, O. J. L., Lear, C. H., & Pollard, D. (2012). Exploring uncertainties in the relationship between temperature, ice volume, and sea level over the past 50 million years, *Reviews of Geophysics*, 50, RG1005.
- Gebhardt, A. C., Geissler, W. H., Matthiessen, J., & Jokat, W. (2014). Changes in current patterns in the Fram Strait at the Pliocene/Pleistocene boundary. *Quaternary Science Reviews*, 92, 179–189.
- Gehrels, W. R. (1994). Determining relative sea-level change from salt-marsh foraminifera and plant zones on the coast of Maine, USA. *Journal of Coastal Research*, 10, 990–1009.

- Gehrels, W. R. (2000). Using foraminiferal transfer functions to produce high-resolution sea-level records from salt-marsh deposits, Maine, USA. *The Holocene*, 10, 367–376.
- Gehrels, W. R., Roe, H. M., & Charman, D. J. (2001). Foraminifera, testate amoebae and diatoms as sea-level indicators in UK saltmarshes: A quantitative multiproxy approach. *Journal of Quaternary Science*, 16, 201–220.
- Gernon, T. M., Hincks, T. K., Merdith, A., Rohling, E. J., Palmer, M. R., Foster, G. L., Bataille, C. P., & Müller, R. D. (2021). Global chemical weathering dominated by continental arcs since the mid-Palaeozoic. *Nature Geoscience*, 14, 690–696.
- Ghosh, P., Adkins, J., Affek, H., Balta, B., Guo, W., Schauble, E. A., Schrag, D., & Eiler, J. M. (2006). ^{13}C – ^{18}O bonds in carbonate minerals: A new kind of paleothermometer. *Geochimica et Cosmochimica Acta*, 70, 1439–1456.
- Gibert, J., Gibert, L., & Iglesias, A. (2003). The Gibraltar strait: A Pleistocene door of Europe? *Human Evolution*, 18, 147–160.
- Goelzer, H., Coulon, V., Pattyn, F., de Boer, B., & van de Wal, R. (2020). Brief communication: On calculating the sea-level contribution in marine ice-sheet models. *The Cryosphere*, 14, 833–840.
- Gomez, N., Mitrovica, J., Huybers, P., & Clark, P. U. (2010a). Sea level as a stabilizing factor for marine-ice-sheet grounding lines. *Nature Geoscience*, 3, 850–853.
- Gomez, N., Mitrovica, J. X., Tamisiea, M. E., & Clark, P. U. (2010b). A new projection of sea level change in response to collapse of marine sectors of the Antarctic Ice Sheet. *Geophysical Journal International*, 180, 623–634.
- Gomez, N., Weber, M. E., Clark, P. U., Mitrovica, J. X., & Han, H. K. (2020). Antarctic ice dynamics amplified by Northern Hemisphere sea-level forcing. *Nature*, 587, 600–604.
- Gornitz, V., Oppenheimer, M., Kopp, R., Orton, P., Buchanan, M., Lin, N., Horton, R., & Bader D. (2019). New York City Panel on Climate Change 2019 Report Chapter 3: Sea Level Rise. *Annals of the New York Academy of Sciences*, 1439, 71–94.
- Graham, A. G. C., Wåhlin, A., Hogan, K. A., Nitsche, F. O., Heywood, K. J., Totten, R. L., Smith, J. A., Hillenbrand, C.-D., Simkins, L. M., Anderson, J. B., Wellner, J. S., & Larter, R. D. (2022). Rapid retreat of Thwaites Glacier in the pre-satellite era. *Nature Geoscience*, <https://doi.org/10.1038/s41561-022-01019-9>.
- Grant, G. R., Naish, T. R., Dunbar, G. B., Stocchi, P., Kominz, M. A., Kamp, P. J. J., Tapia, C. A., McKay, R. M., Levy, R. H., & Patterson, M. O. (2019). The amplitude and origin of sea-level variability during the Pliocene epoch. *Nature*, 574, 237–241.
- Grant, K. M., Amarathunga, U., Amies, J. D., Hu, P. X., Qian, Y., Penny, T., Rodriguez-Sanz, L., Zhao, X., Heslop, D., Liebrand, D., Hennekam, R., Westerhold, T., Gilmore, S., Lourens, L. J., Roberts, A. P., & Rohling, E. J. (2022). Organic carbon burial in Mediterranean sapropels intensified during Green Sahara Periods since 3.2 Myr ago. *Communications Earth and Environment*, 3, 11.
- Grant, K. M., Grimm, R., Mikolajewicz, U., Marino, G., Ziegler, M., & Rohling, E. J. (2016). The timing of Mediterranean sapropel deposition relative to insolation, sea-level and African monsoon changes. *Quaternary Science Reviews*, 140, 125–141.
- Grant, K. M., Rohling, E. J., Bar-Matthews, M., Ayalon, A., Medina-Elizalde, M., Bronk Ramsey, C., Satow, C., & Roberts, A. P. (2012). Rapid coupling between ice volume and polar temperature over the past 150 kyr. *Nature*, 491, 744–747.
- Grant, K. M., Rohling, E. J., Bronk Ramsey, C., Cheng, H., Edwards, R. L., Florindo, F., Heslop, D., Marra, F., Roberts, A. P., Tamisiea, M. E., & Williams, F. (2014). Sea-level variability over five glacial cycles. *Nature Communications*, 5, 5076.

- Grant, K. M., Rohling, E. J., Westerhold, T., Zabel, M., Heslop, D., Konijnendijk, T., & Lourens, L. J. (2017). A 3 million year index for North African humidity/aridity and the implication of potential pan-African Humid periods. *Quaternary Science Reviews*, 171, 100–118.
- Grauel, A.-L., Schmid, T. W., Hu, B., Bergami, C., Capotondi, L., Zhou, L., & Bernasconi, S. M. (2013). Calibration and application of the ‘clumped isotope’ thermometer to foraminifera for high-resolution climate reconstructions. *Geochimica et Cosmochimica Acta*, 108, 125–140.
- Gregory, J. M., Griffies, S. M., Hughes, C. W., Lowe, J. A., Church, J. A., Fukumori, I., Gomez, N., Kopp, R. E., Landerer, F., Le Cozannet, R., Ponte, M., Stammer, D., Tamsiea, M. E., & van de Wal, R. S. W. (2019). Concepts and terminology for sea level: Mean, variability and change, both local and global. *Surveys in Geophysics*, 40, 1251–1289.
- Griffith, E. M., Paytan, A., Caldeira, K., Bullen, T. D., & Thomas, E. (2008). A dynamic marine calcium cycle during the past 28 million years. *Science*, 322, 1671–1674.
- Halicz, E., & Reiss, Z. (1981). Palaeoecological relations of foraminifera in a desert enclosed sea—The Gulf of Aqaba. *Marine Ecology*, 2, 15–34.
- Hallmann, N., Camoin, G. F., Eisenhauer, A., Botella, A., Milne, G. A., Vella, C., Samankassou, E., Pothin, V., Dussouillez, P., Fleury, J., & Fietzke, J. (2018). Ice volume and climate changes from a 6000 year sea-level record in French Polynesia. *Nature Communications*, 9, 285.
- Hamelin, B., Bard, E., Zindler, A., & Fairbanks, R. G. (1991). $^{234}\text{U}/^{238}\text{U}$ mass spectrometry of corals: How accurate is the U–Th age of the last interglacial period? *Earth and Planetary Science Letters*, 106, 169–180.
- Hanebuth, T. J. J., Stattegger, K., & Grootes, P. M. (2000). Rapid flooding of the Sunda shelf: a late glacial sea level record. *Science*, 288, 1033–1035.
- Hanebuth, T. J. J., Stattegger, K., & Bojanowski, A. (2009). Termination of the Last Glacial Maximum sea-level lowstand: The Sunda-Shelf data revisited. *Global and Planetary Change*, 66, 76–84.
- Hansen, J., Sato, M., Kharecha, P., Russell, G., Lea, D. W., & Siddall, M. (2007). Climate change and trace gases. *Philosophical Transactions of the Royal Society A*, 365, 1925–1954.
- Hansen, J., Sato, M., Kharecha, P., Beerling, D., Berner, R., Masson-Delmotte, V., Pagani, M., Raymo, M., Royer, D. L., & Zachos J. C. (2008). Target atmospheric CO₂: Where should humanity aim? *Open Atmospheric Science Journal*, 2, 217–231.
- Hansen, J., Sato, M., Russell, G., & Kharecha, P. (2013). Climate sensitivity, sea level and atmospheric carbon dioxide. *Philosophical Transactions of the Royal Society A*, 371, 20120294.
- Harishidayat, D., Johansen, S. E., Batchelor, C., Omosanya, K. O., & Ottaviani, L. (2021). Pliocene–Pleistocene glacimarine shelf to slope processes in the south-western Barents Sea. *Basin Research*, 33, 1315–1336.
- Harmon, R. S., & Schwarcz, H. P. (1981). Changes of ^2H and ^{18}O enrichment of meteoric water and Pleistocene glaciation. *Nature*, 290, 125–128.
- Harwood, D. M., & Webb, P. N. (1990). Early Pliocene glaciation of the Antarctic ice sheet and late Pliocene onset of bipolar glaciation. *Eos (Transactions, American Geophysical Union)*, 71, 538–539.
- Hasenfratz, A. P., Jaccard, S. L., Martínez-García, A., Sigman, D. M., Hodell, D. A., Vance, D., Bernasconi, S. M., Kleiven, H., Haumann, F. A., & Haug, G. H. (2019). The residence time of Southern Ocean surface waters and the 100,000-year ice age cycle. *Science*, 363, 1080–1084.
- Hasenfratz, A. P., Schiebel, R., Thornalley, D. J., Schönfeld, J., Jaccard, S. L., Martínez-García, A., Holbourn, A., Jennings, A. E., Kuhnt, W., Lear, C. H., Marchitto, T. M., Quillmann, U., Rosenthal, Y.,

- Yu, J., & Haug, G. H. (2017). Mg/Ca-temperature calibration for the benthic foraminifera *Melonis barleeanum* and *Melonis pompilioides*. *Geochimica et Cosmochimica Acta*, 217, 365–383.
- Hays, J. D., Imbrie, J., & Shackleton, N. J. (1976). Variations in the Earth's orbit: pacemaker of the ice ages. *Science*, 194, 1121–1132.
- Hearty P. J. (2002). The Ka'ena Highstand of O'ahu, Hawai'i: Further evidence of Antarctic ice collapse during the Middle Pleistocene. *Pacific Science*, 56, 65–81.
- Hearty, P. J., Hollin, J. T., Neumann, A. C., O'Leary, M. J., & McCulloch, M. (2007). Global sea-level fluctuations during the Last Interglaciation (MIS 5e). *Quaternary Science Reviews*, 26, 2090–2112.
- Hearty, P. J., Kindler, P., Cheng, H., & Edwards, R. L. (1999). A +20 m middle Pleistocene sea-level highstand (Bermuda and the Bahamas) due to partial collapse of Antarctic ice. *Geology*, 27, 375–378.
- Hemleben, C., Meischner, D., Zahn, R., Almogi-Labin, A., Erlenkeuser, H., & Hiller, B. (1996). Three hundred eighty thousand year long stable isotope and faunal records from the Red Sea: Influence of global sea level change on hydrography. *Paleoceanography*, 11, 147–156.
- Hibbert, F. D., Rohling, E. J., Dutton, A., Williams, F. H., Cutcharavan, P. H., Zhao, C., & Tamsiea, M. A. (2016). Corals as indicators of past sea-level change: a global repository of U-series dated benchmarks. *Quaternary Science Reviews*, 145, 1–56.
- Hibbert, F. D., Williams, F. H., Fallon, S., & Rohling, E.J. (2018). Last deglacial sea level: A database of biological and geomorphological sea-level markers. *Scientific Data*, 5, 180088,
- Hieronymus, M. (2019). An update on the thermosteric sea level rise commitment to global warming. *Environmental Research Letters*, 14, 054018.
- Hill, J., Avdis, A., Bailey, G., & Lambeck, K. (2022). Sea-level change, palaeotidal modelling and hominin dispersals: The case of the southern Red Sea. *Quaternary Science Reviews*, 293, 107719.
- Hochmuth, K., Gohl, K., Leitchenkov, G., Sauermilch, I., Whittaker, J. M., Uenzelmann-Neben, G., Davy, B., & De Santis, L. (2020). The evolving paleobathymetry of the circum-Antarctic Southern Ocean since 34 Ma: A key to understanding past cryosphere-ocean developments. *Geochemistry, Geophysics, Geosystems*, 21, e2020GC009122.
- Holbourn, A., Kuhnt, W., Clemens, S., Prell, W., & Andersen, N. (2013). Middle to late Miocene stepwise climate cooling: Evidence from a high-resolution deep water isotope curve spanning 8 million years. *Paleoceanography*, 28, 688–699.
- Hölzchen, E., Hertler, C., Willmes, C., Anwar, I. P., Mateos, A., Rodríguez, J., Berndt, J. O., & Timm, I. J. (2022). Estimating crossing success of human agents across sea straits out of Africa in the Late Pleistocene. *Palaeogeography, Palaeoclimatology, Palaeoecology*, 590, 110845.
- Houben, A. J. P., van Mourik, C. A., Montanari, A., Coccioni, R., & Brinkhuis, H. (2012). The Eocene–Oligocene transition: Changes in sea level, temperature or both? *Palaeogeography, Palaeoclimatology, Palaeoecology*, 335–336, 75–83.
- Hu, B., Radke, J., Schlüter, H.-J., Heine, F. T., Zhou, L., & Bernasconi, S. M. (2014). A modified procedure for gas-source isotope ratio mass spectrometry: The long-integration dual-inlet (LIDI) methodology and implications for clumped isotope measurements. *Rapid Communications in Mass Spectrometry*, 28, 1413–1425.
- Hutchinson, D. K., Coxall, H. K., Lunt, D. J., Steinthorsdottir, M., de Boer, A. M., Baatsen, M., von der Heydt, A., Huber, M., Kennedy-Asser, A. T., Kunzmann, L., Ladant, J.-B., Lear, C. H., Moraweck, K., Pearson, P. N., Piga, E., Pound, M. J., Salzmann, U., Scher, H. D., Sijp, W. P., Śliwińska, K. K., Wilson, P. A., & Zhang, Z. (2021). The Eocene–Oligocene transition: A review of marine and terrestrial proxy data, models and model–data comparisons. *Climate of the Past*, 17, 269–315.

- Huybrechts, P. (1993). Glaciological modelling of the Late Cenozoic East Antarctic ice sheet: stability or dynamism? *Geografiska Annaler: Series A, Physical Geography*, 75, 221–238.
- Imbrie, J., & Imbrie, J.Z. (1980). Modeling the climatic response to orbital variations. *Science*, 207, 942–953.
- Imbrie, J., Boyle, E. A., Clemens, S. C., Duffy, A., Howard, W. R., Kukla, G., Kutzbach, J., Martinson, D. G., McIntyre, A., Mix, A. C., Molino, B., Morley, J. J., Peterson, L. C., Pisias, N. G., Prell, W. L., Raymo, M., Shackleton, N. J., & Toggweiler, J. R. (1992). On the structure and origin of major glaciation cycles 1. Linear responses to Milankovitch forcing. *Paleoceanography and Paleoclimatology*, 7, 701–738.
- Imbrie, J., Boyle, E. A., Clemens, S. C., Duffy, A., Howard, W. R., Kukla, G., Kutzbach, J., Martinson, D. G., McIntyre, A., Mix, A. C., Molino, B., Morley, J. J., Peterson, L. C., Pisias, N. G., Prell, W. L., Raymo, M. E., Shackleton, N. J., and Toggweiler, J. R. (1993). On the structure and origin of major glaciation cycles. 2. The 100,000-year cycle. *Paleoceanography*, 8, 699–735.
- Imbrie, J., Shackleton, N. J., Pisias, N. G., Morley, J. J., Prell, W. L., Martinson, D. G., Hays, J. D., McIntyre, A., & Mix, A. C. (1984). The orbital theory of Pleistocene climate: Support from a revised chronology of the marine $\delta^{18}\text{O}$ record. In: Berger, A., Imbrie, J., Hays, J., Kukla, G., Saltzman, B. (Eds.), *Milankovitch and climate: Understanding the response to astronomical forcing*. D.Reidel, Hingham, Massachusetts, USA, pp. 269–305.
- Ishiwa, T., Yokoyama, Y., Miyairi, Y., Obrochta, S., Sasaki, T., Kitamura, A., Suzuki, A., Ikehara, M., Ikehara, K., Kimoto, K., Bourget, J., & Matsuzaki, H. (2016). Reappraisal of sea-level lowstand during the Last Glacial Maximum observed in the Bonaparte Gulf sediments, northwestern Australia. *Quaternary International*, 397, 373–379.
- Ishiwa, T., Yokoyama, Y., Okuno, J., Obrochta, S., Uehara, K., Ikehara, M., & Miyairi, Y. (2019). A sea-level plateau preceding Marine Isotope Stage 2 minima revealed by Australian sediments. *Scientific Reports*, 9, 6449.
- Israelson, C., & Wohlfarth, B. (1999). Timing of the Last Interglacial high sea level on the Seychelles Islands, Indian Ocean. *Quaternary Research*, 51, 306–316.
- Ivanova, E. V. (1985). Late Quaternary biostratigraphy and palaeo-temperatures of the Red Sea and Gulf of Aden based on planktonic foraminifera and pteropods. *Marine Micropaleontology*, 9, 335–364.
- Jakob, K. A., Wilson, P. A., Pross, J., Ezard, T. H. G., Fiebig, J., Repschläger, J., & Friedrich, O. (2020). A new sea-level record for the Neogene/Quaternary boundary reveals transition to a more stable East Antarctic Ice Sheet. *Proceedings of the National Academy of Sciences of the USA*, 117, 30980–30987.
- Jakobsson, M., Nilsson, J., Anderson, L., Backman, J., Björk, G., Cronin, T. M., Kirchner, N., Koshurnikov, A., Mayer, L., Noormets, R., & O'Regan, M. (2016). Evidence for an ice shelf covering the central Arctic Ocean during the penultimate glaciation. *Nature Communications*, 7, 10365.
- Jakobsson, M., Nilsson, J., O'Regan, M., Backman, J., Löwemark, L., Dowdeswell, J. A., Mayer, L., Polyak, L., Colleoni, F., Anderson, L. G., & Björk, G. (2010). An Arctic Ocean ice shelf during MIS 6 constrained by new geophysical and geological data. *Quaternary Science Reviews*, 29, 3505–3517.
- Jakobsson, M., Polyak, L., Edwards, M., Kleman, J., & Coakley, B. (2008). Glacial geo-morphology of the Central Arctic Ocean: The Chukchi borderland and the Lomonosov Ridge. *Earth Surface Processes and Landforms*, 33, 526–545.
- Jansen, E., & Sjøholm, J. (1991). Reconstruction of glaciation over the past 6 Myr from ice-borne deposits in the Norwegian Sea. *Nature*, 349, 600–603.
- John, C. M., Karner, G. D., Browning, E., Leckie, R. M., Mateo, Z., Carson, B., & Lowery, C. (2011). Timing and magnitude of Miocene eustasy derived from the mixed siliciclastic-carbonate

stratigraphic record of the northeastern Australian margin. *Earth and Planetary Science Letters*, 304, 455–467.

Jouzel, J., Masson-Delmotte, V., Cattani, O., Dreyfus, G., Falourd, S., Hoffmann, G., Minster, B., Nouet, J., Barnola, J. M., Chappellaz, J., Fischer, H., Gallet, J. C., Johnsen, S., Leuenberger, M., Loulergue, L., Luethi, D., Oerter, H., Parrenin, F., Raisbeck, G., Raynaud, D., Schwander, J., Spahni, R., Souchez, R., Selmo, E., Schilt, A., Steffensen, J. P., Stenni, B., Stauffer, B., Stocker, T. F., Tison, J. L., Werner, M., & Wolff, E. W. (2007). Orbital and millennial Antarctic climate variability over the past 800,000 years. *Science*, 317, 793–796.

Karner, D. B., Levine, J., Medeiros, B. P., & Muller, R. A. (2002). Constructing a stacked benthic $\delta^{18}\text{O}$ record. *Paleoceanography*, 17, 1030.

Katz, M. E., Miller, K. G., Wright, J. D., Wade, B. S., Browning, J. V., Cramer, B. S., & Rosenthal, Y. (2008). Stepwise transition from the Eocene greenhouse to the Oligocene icehouse. *Nature Geoscience*, 1, 329–334.

Kemp, A., Horton, B. P., Donnelly, J. P., Mann, M. E., Vermeer, M., & Rahmstorf, S. (2011). Climate related sea-level variations over the past two millennia. *Proceedings of the National Academy of Sciences of the USA*, 108, 11017–11022.

Kennedy, D. M., Marsters, T. H., Woods, J. L. D., & Woodroffe, C. D. (2012). Shore platform development on an uplifting limestone island over multiple sea-level cycles, Niue, South Pacific. *Geomorphology*, 141–142, 170–182.

Kennett, J. P. (1977). Cenozoic evolution of Antarctic glaciations, the circum-Antarctic ocean and their impact on global paleoceanography. *Journal of Geophysical Research*, 82, 3843–3860.

Khan, N. S., Ashe, E., Horton, B. P., Dutton, A., Kopp, R. E., Brocard, G., Engelhart, S. E., Hill, D. F., Peltier, W. R., Vane, C. H., & Scatena, F. N. (2017). Drivers of Holocene sea-level change in the Caribbean. *Quaternary Science Reviews*, 155, 13–36.

Khazendar, A., Fenty, I. G., Carroll, D., Gardner, A., Lee, C. M., Fukumori, I., Wang, O., Zhang, H., Seroussi, H., Moller, D., Noël, B. P. Y., van den Broeke, M. R., Dinardo, S., & Willis, J. (2019a). Interruption of two decades of Jakobshavn Isbrae acceleration and thinning as regional ocean cools. *Nature Geoscience*, 12, 277–283.

Khazendar, A., Fenty, I. G., Carroll, D., Gardner, A., Lee, C. M., Fukumori, I., Wang, O., Zhang, H., Seroussi, H., Moller, D., Noël, B. P. Y., van den Broeke, M. R., Dinardo, S., & Willis, J. (2019b). Author Correction: Interruption of two decades of Jakobshavn Isbrae acceleration and thinning as regional ocean cools. *Nature Geoscience*, 12, 493–493.

Kienast, M., Hanebuth, T. J. J., Pelejero, C., & Steinke, S. (2003). Synchronicity of meltwater pulse 1a and the Bølling warming: New evidence from the South China Sea. *Geology*, 31, 67–70.

Kim, S. T., & O'Neil, J. R. (1997). Equilibrium and nonequilibrium oxygen isotope effects in synthetic calcites. *Geochimica et Cosmochimica Acta*, 61, 3461–3475.

Kleiven, H. F., Jansen, E., Fronval, T., & Smith, T. M. (2002). Intensification of Northern Hemisphere glaciations in the circum Atlantic region (3.5–2.4 Ma)—ice-rafted detritus evidence. *Palaeogeography, Palaeoclimatology, Palaeoecology*, 184, 213–223.

Knies, J., Matthiessen, J., Vogt, C., Laberg, J. S., Hjelstuen, B. O., Smelror, M., Larsen, E., Andreassen, K., Eidvin, T., & Vorren, T. O. (2009). The Plio-Pleistocene glaciation of the Barents Sea–Svalbard region: A new model based on revised chronostratigraphy. *Quaternary Science Reviews*, 28, 812–829.

- Köhler, P., Bintanja, R., Fischer, H., Joos, F., Knutti, R., Lohmann, G., & Masson-Delmotte, V. (2010). What caused Earth's temperature variations during the last 800 000 years? Data-based evidence on radiative forcing and constraints on climate sensitivity. *Quaternary Science Reviews*, 29, 129–145.
- Kominz, M. A., Browning, J. V., Miller, K. G., Sugarman, P. J., Mizintseva, S., & Scotese, C. R. (2008). Late Cretaceous to Miocene sea-level estimates from the New Jersey and Delaware coastal plain coreholes: An error analysis. *Basin Research*, 20, 211–226.
- Kominz, M. A., Miller, K. G., Browning, J. V., Katz, M. E., & Mountain, G. S. (2016). Miocene relative sea level on the New Jersey shallow continental shelf and coastal plain derived from one-dimensional backstripping: A case for both eustasy and epeirogeny. *Geosphere*, 12, 1437–1456.
- Konijnendijk, T., Ziegler, M., & Lourens, L. (2014). Chronological constraints on Pleistocene sapropel depositions from high-resolution geochemical records of ODP sites 967 and 968. *Newsletters on Stratigraphy*, 47, 263–282.
- Kopp, R. E., Simons, F. J., Mitrovica, J. X., Maloof, A. C., & Oppenheimer, M. (2009). Probabilistic assessment of sea level during the last interglacial stage. *Nature*, 462, 863–867.
- Ku, T. L., Thurber, D. L., & Mathieu, G. G. (1969). Radiocarbon chronology of Red Sea sediments. In: Degens, E. T., & Ross, D. A. (Eds.). *Hot Brines and Recent Heavy Metal Deposits in the Red Sea*, Springer, Berlin, pp. 348–359.
- Kuchar, J., Milne, G. A., Hill, A., Tarasov, L., & Nordman, M. (2020). An investigation into the sensitivity of postglacial decay times to uncertainty in the adopted ice history. *Geophysical Journal International*, 220, 1172–1186.
- Labeyrie, L. D., Duplessy, J. C., & Blanc, P. L. (1987). Variations in the mode of formation and temperature of oceanic deep waters over the past 125,000 years. *Nature*, 327, 477–482.
- Lambeck, K., & Chappell, J. (2001). Sea level change through the Last Glacial cycle. *Science*, 292, 679–686.
- Lambeck, K., Purcell, A., Flemming, N. C., Vita-Finzi, C., Alskarekh, A. M., & Bailey, G. N. (2011). Sea level and shoreline reconstructions for the Red Sea: Isostatic and tectonic considerations and implications for hominin migration out of Africa. *Quaternary Science Reviews*, 30, 3542–3574.
- Lambeck, K., Rouby, H., Purcell, A., Sun, Y., & Sambridge, M. (2014). Sea level and global ice volumes from the Last Glacial maximum to the Holocene. *Proceedings of the National Academy of Sciences of the USA*, 111, 15296–15303.
- Larrasoaña, J. C., Roberts, A. P., & Rohling, E. J. (2013). Dynamics of green Sahara periods and their role in hominin evolution. *PLoS ONE*, 8, e76514.
- Laskar, J., Joutel, F., & Boudin, F. (1993). Orbital, precessional and insolation quantities for the Earth from –20 Myr to +10 Myr. *Astronomy and Astrophysics*, 270, 522–533.
- Laskar, J., Fienga, A., Gastineau, M., & Manche, H. (2011). La2010: A new orbital solution for the long-term motion of the Earth. *Astronomy and Astrophysics*, 532, A89.
- Laskar, J., Robutel, P., Joutel, F., Gastineau, M., Correia, A. C. M., & Levrard, B. (2004). A long-term numerical solution for the insolation quantities of the Earth. *Astronomy and Astrophysics*, 428, 261–285.
- Lawrence, K. T., Liu, Z., & Herbert, T. D. (2006). Evolution of the eastern tropical Pacific through Plio-Pleistocene glaciation. *Science*, 312, 79–83.
- Lear, C. H., Anand, P., Blenkinsop, T., Foster, G. L., Gagen, M., Hoogakker, B., Larter, R. D., Lunt, D. J., McCave, I. N., McClymont, E., Pancost, R. D., Rickaby, R. E. M., Schultz, D. M., Summerhayes, C., Williams, C. J. R., & Zalasiewicz, J. (2021). Geological Society of London Scientific Statement: What

the geological record tells us about our present and future climate. *Journal of the Geological Society*, 178, jgs2020-239.

Lear, C. H., Bailey, T. R., Pearson, P. N., Coxall, H. K., & Rosenthal, Y. (2008). Cooling and ice growth across the Eocene-Oligocene transition. *Geology*, 36, 251–254.

Lear, C. H., Mawbey, E., & Rosenthal, Y. (2010). Cenozoic benthic foraminiferal Mg/Ca and Li/Ca records: Toward unlocking temperatures and saturation states. *Paleoceanography*, 25, PA4215.

Lear, C. H., Rosenthal, Y., Coxall, H. K., & Wilson, P. A. (2004). Late Eocene to early Miocene ice sheet dynamics and the global carbon cycle. *Paleoceanography*, 19, PA4015.

Lear, C. H., Rosenthal, Y., & Slowey, N. (2002). Benthic foraminiferal Mg/Ca-paleothermometry: A revised core-top calibration. *Geochimica et Cosmochimica Acta*, 66(19), 3375–3387.

Lebrato, M., Garbe-Schönberg, D., Müller, M. N., Blanco-Ameijeiras, S., Feely, R. A., Lorenzoni, L., Molinero, J.-C., Bremer, K., Jones, D. O. B., Iglesias-Rodriguez, D., Greeley, D., Lamare, M. D., Paulmier, A., Graco, M., Cartes, J., Barcelos e Ramos, J., de Lara, A., Sanchez-Leal, R., Jimenez, P., Paparazzo, F. E., Hartman, S. E., Westernströer, U., Küter, M., Benavides, R., da Silva, A. F., Bell, S., Payne, C., Olafsdottir, S., Robinson, K., Jantunen, L. M., Korablev, A., Webster, R. J., Jones, E. M., Gilg, O., Bailly du Bois, P., Beldowski, J., Ashjian, C., Yahia, N. D., Twining, B., Chen, X.-G., Tseng, L.-C., Hwang, J.-S., Dahms, H.-U., & Oschlies, A. (2020). Global variability in seawater Mg:Ca and Sr:Ca ratios in the modern ocean. *Proceedings of the National Academy of Sciences of the USA*, 117, 22281–22292.

Lee, G. E., Condamine, F. L., Bechteler, J., Pérez-Escobar, O. A., Scheben, A., Schäfer-Verwimp, A., Pócs, T., & Heinrichs, J. (2020). An ancient tropical origin, dispersals via land bridges and Miocene diversification explain the subcosmopolitan disjunctions of the liverwort genus *Lejeunea*. *Scientific Reports*, 10, 14123.

Lee, K. E., Clemens, S. C., Kubota, Y., Timmermann, A., Holbourn, A., Yeh, S.-W., Bae, S. W., & Ko, T. W. (2021). Roles of insolation forcing and CO₂ forcing on Late Pleistocene seasonal sea surface temperatures. *Nature Communications*, 12, 5742.

Leonard, N. D., Zhao, J. X., Welsh, K. J., Feng, Y. X., Smithers, S. G., Pandolfi, J. M., & Clark, T. R. (2016). Holocene sea level instability in the southern Great Barrier Reef, Australia: high-precision U–Th dating of fossil microatolls. *Coral Reefs*, 35, 625–639.

Levermann, A., & Winkelmann, R. (2016). A simple equation for the melt elevation feedback of ice sheets. *The Cryosphere*, 10, 1799–1807.

Lewis, A. R., Marchant, D. R., Ashworth, A. C., Hedenäs, L., Hemming, S. R., Johnson, J. V., Leng, M. J., Machlus, M. L., Newton, A. E., Raine, J. I., Willenbring, J. K., Williams, M., & Wolfe, A. P. (2008). Mid-Miocene cooling and the extinction of tundra in continental Antarctica. *Proceedings of the National Academy of Sciences of the USA*, 105, 10676–10680.

Lewis, S. E., Sloss, C. R., Murray-Wallace, C. V., Woodroffe, C. D., & Smithers, S. G. (2013). Post-glacial sea-level changes around the Australian margin: A review. *Quaternary Science Reviews*, 74, 115–138.

Lewis, S. E., Wüst, R. A., Webster, J. M., Shields, G. A., Renema, W., Lough, J. M., & Jacobsen, G. (2012). Development of an inshore fringing coral reef using textural, compositional and stratigraphic data from Magnetic Island, Great Barrier Reef, Australia. *Marine Geology*, 299, 18–32.

Lhomme, N. (2004). Modelling water isotopes in polar ice sheets. Ph.D. thesis, University of British Columbia, Vancouver, B. C., Canada, doi: 10.14288/1.0052371.

Lhomme, N., Clarke, G. K. C., & Ritz, C. (2005). Global budget of water isotopes inferred from polar ice sheets. *Geophysical Research Letters*, 32, L20502.

- Li, L., Li, Q., Tian, J., Wang, P., Wang, H., & Liu, Z. (2011). A 4-Ma record of thermal evolution in the tropical western Pacific and its implications on climate change. *Earth and Planetary Science Letters*, 309, 10–20.
- Liebrand, D., Lourens, L. J., Hodell, D. A., De Boer, B., Van de Wal, R. S. W., & Pälike, H. (2011). Antarctic ice sheet and oceanographic response to eccentricity forcing during the early Miocene. *Climate of the Past*, 7, 869–880.
- Lisiecki, L. E., & Raymo, M. E. (2005). A Pliocene-Pleistocene stack of 57 globally distributed benthic $\delta^{18}\text{O}$ records. *Paleoceanography and Paleoclimatology*, 20, PA1003.
- Liu, Z., & Herbert, T. D. (2004). High-latitude influence on the eastern equatorial Pacific climate in the early Pleistocene epoch. *Nature*, 427, 720–723.
- Liu, J., Fang, N., Wang, F., Yang, F., & Ding, X. (2018). Features of ice-rafted debris (IRD) at IODP site U1312 and their palaeoenvironmental implications during the last 2.6 Myr. *Palaeogeography, Palaeoclimatology, Palaeoecology*, 511, 364–378.
- Liu, Z., Pagani, M., Zinniker, D., DeConto, R. M., Huber, M., Brinkhuis, H., Shah, S. R., Leckie, R. M., & Pearson, A. (2009). Global cooling during the Eocene-Oligocene climate transition. *Science*, 323, 1187–1190.
- Locke, S. M., & Thunell, R. C. (1988). Palaeoceanographic record of the last glacial–interglacial cycle in the Red Sea and Gulf of Aden. *Palaeogeography, Palaeoclimatology, Palaeoecology*, 64, 163–187.
- Lourens, L. J., Antonarakou, A., Hilgen, F. J., van Hoof, A. A. M., Vergnaud-Grazzini, C., & Zachariasse, W. J. (1996). Evaluation of the Plio-Pleistocene astronomical time-scale. *Paleoceanography*, 11, 391–413.
- Lourens, L. J., Wehausen, R., & Brumsack, H. (2001). Geological constraints on tidal dissipation and dynamical ellipticity of the Earth over the past three million years. *Nature*, 409, 1029–1033.
- Loutre, M. F., Paillard, D., Vimeux, F., & Cortijo, E. (2004). Does mean annual insolation have the potential to change the climate? *Earth and Planetary Science Letters*, 221, 1–14.
- Ludwig, K. R., Muhs, D. R., Simmons, K. R., Halley, R. B., & Shinn, E. A. (1996). Sea-level records at ~80 ka from tectonically stable platforms: Florida and Bermuda. *Geology*, 24, 211–214.
- Lythe, M. B., Vaughan, D. G., & the BEDMAP Consortium. (2001). BEDMAP: A new ice thickness and subglacial topographic model of Antarctica. *Journal of Geophysical Research*, 106, 11335–11351.
- MacFerrin, M., Machguth, H., As, D. V., Charalampidis, C., Stevens, C. M., Heilig, A., Vandecrux, B., Langen, P. L., Mottram, R., Fettweis, X., van den Broeke, M. R., Pfeffer, W. T., Moussavi, M. S., & Abdalati, W. (2019). Rapid expansion of Greenland's low-permeability ice slabs. *Nature*, 573, 403–407.
- Machado, L., Harris, D. J., & Salvi, D. (2021). Biogeographic and demographic history of the Mediterranean snakes *Malpolon monspessulanus* and *Hemorrhois hippocrepis* across the Strait of Gibraltar. *BMC Ecology and Evolution*, 21, 1–14.
- Manabe, S., & Broccoli, A. J. (1985). The influence of continental ice sheets on the climate of an ice age. *Journal of Geophysical Research*, 90, 2167–2190.
- Marchitto, T. M., & deMenocal, P. B. (2003). Late Holocene variability of upper North Atlantic Deep Water temperature and salinity. *Geochemistry, Geophysics, Geosystems*, 4, 1100.
- Marchitto, T. M., Bryan, S. P., Curry, W. B., & McCorkle, D. C. (2007). Mg/Ca temperature calibration for the benthic foraminifer *Cibicides pachyderma*. *Paleoceanography*, 22, PA1203.

- Martin, P. A., Lea, D. W., Rosenthal, Y., Shackleton, N. J., Sarnthein, M., & Papenfuss, T. (2002). Quaternary deep sea temperature histories derived from benthic foraminiferal Mg/Ca. *Earth and Planetary Science Letters*, 198, 193–209.
- Martinson, D. G., Pisias, N. G., Hays, J. D., Imbrie, J., Moore, T. C., & Shackleton, N. J. (1987). Age dating and the orbital theory of the ice ages: Development of a high-resolution 0 to 300,000 year chronostratigraphy. *Quaternary Research*, 27, 1–29.
- Maslin, M. A., Li, X. S., Loutre, M. F., & Berger, A. (1998). The contribution of orbital forcing to the progressive intensification of Northern Hemisphere glaciation. *Quaternary Science Reviews*, 17, 411–426.
- Masson-Delmotte, V., Stenni, B., Pol, K., Braconnot, P., Cattani, O., Falourd, S., Kageyama, M., Jouzel, J., Landais, A., Minster, B., Barnola, J. M., Chapellaz, J., Krinner, G., Johnsen, S., Röthlisberger, R., Hansen, J., Mikolajewicz, U., & Otto-Bliesner, B. (2010). EPICA Dome C record of glacial and interglacial intensities. *Quaternary Science Reviews*, 29, 113–128.
- Matthews, R.K. (1984). Oxygen isotope record of ice-volume history: 100 million years of glacio-eustatic sea-level fluctuation. *AAPG Memoir*, 36, <https://doi.org/10.1306/M36440>.
- Matthews, K. J., Maloney, K. T., Zahirovic, S., Williams, S. E., Seton, M., & Müller, R. D. (2016). Global plate boundary evolution and kinematics since the late Paleozoic. *Global and Planetary Change*, 146, 226–250.
- Matthews, R. K., & Poore, R. Z. (1980). Tertiary $\delta^{18}\text{O}$ record and glacio-eustatic sea-level fluctuations. *Geology*, 8, 501–504.
- Matthiessen, S., & Haines, K. (2003). A hydraulic box model study of the Mediterranean response to postglacial sea-level rise. *Paleoceanography*, 18, doi:10.1029/2003PA000880.
- McCrea, J. M. (1950). On the isotopic chemistry of carbonates and a paleotemperature scale. *Journal of Chemical Physics*, 18, 849–857.
- McCulloch, M. T., & Mortimer, G. E. (2008). Applications of the ^{238}U – ^{230}Th decay series to dating of fossil and modern corals using MC-ICPMS. *Australian Journal of Earth Sciences*, 55, 955–965.
- McMurtry, G. M., Campbell, J. F., Fryer, G. J., & Fietzke, J. (2010). Uplift of Oahu, Hawaii, during the past 500 k.y. as recorded by elevated reef deposits. *Geology*, 38, 27–30.
- Meckler, A. N., Ziegler, M., Millán, M. I., Breitenbach, S. F. M., & Bernasconi, S. M. (2014). Long-term performance of the Kiel carbonate device with a new correction scheme for clumped isotope measurements. *Rapid Communications in Mass Spectrometry*, 28, 1705–1715.
- Medina-Elizalde, M. (2013). A global compilation of coral sea-level benchmarks: Implications and new challenges. *Earth and Planetary Science Letters*, 362, 310–318.
- Meinicke, N., Ho, S. L., Hannisdal, B., Nürnberg, D., Tripathi, A. K., Schiebel, R., & Meckler, A. N. (2020). A robust calibration of the clumped isotopes to temperature relationship for foraminifers. *Geochimica et Cosmochimica Acta*, 270, 160–183.
- Meltzner, A. J., Switzer, A. D., Horton, B. P., Ashe, E., Qui, Q., Hill, D. F., Bradley, S. L., Kopp, R. E., Hill, E. M., Majewski, J., Natawidjaj, D. H., & Suwargadi, B. W. (2017). Half-metre sea-level fluctuations on centennial timescales from mid-Holocene corals of Southeast Asia. *Nature Communications*, 8, 14387.
- Mikkelsen, A. B., Hubbard, A., MacFerrin, M., Box, J. E., Doyle, S. H., Fitzpatrick, A., Hasholt, B., Bailey, H. L., Lindbäck, K., & Pettersson, R. (2016). Extraordinary runoff from the Greenland ice sheet in 2012 amplified by hypsometry and depleted firn retention. *The Cryosphere*, 10, 1147–1159.

- Miller, K. G., Browning, J. V., Aubry, M. P., Wade, B. S., Katz, M. E., Kulpecz, A. A., & Wright, J. D. (2008). Eocene–Oligocene global climate and sea level changes: St. Stephens Quarry, Alabama. *Geological Society of America Bulletin*, 120, 34–53.
- Miller, K. G., Browning, J. V., Schmelz, W. J., Kopp, R. E., Mountain, G. S., & Wright, J. D. (2020). Cenozoic sea-level and cryospheric evolution from deep-sea geochemical and continental margin records. *Science Advances*, 6, eaaz1346.
- Miller, K. G., Fairbanks, R. G., & Mountain, G. S. (1987). Tertiary oxygen isotope synthesis, sea level history, and continental margin erosion. *Paleoceanography*, 2, 1–19.
- Miller, K. G., Kominz, M. A., Browning, J. V., Wright, J. D., Mountain, G. S., Katz, M. E., Sugarman, P. J., Cramer, B. S., Christie-Blick, N., & Pekar, S. F. (2005). The Phanerozoic record of global sea-level change. *Science*, 310, 1293–1298.
- Miller, K. G., Mountain, G. S., Wright, J. D., & Browning, J. V. (2011). A 180-million-year record of sea level and ice volume variations from continental margin and deep-sea isotopic records. *Oceanography*, 24, 40–53.
- Miller, K. G., Wright, J. D., Browning, J. V., Kulpecz, A., Kominz, M., Naish, T., Cramer, B. S., Rosenthal, Y., Peltier, W. R., & Sostdian, S. (2012). High tide of the warm Pliocene: Implications of global sea level for Antarctic deglaciation. *Geology*, 40, 407–410.
- Miller, K. G., Wright, J. D., & Fairbanks, R. G. (1991). Unlocking the ice house: Oligocene–Miocene oxygen isotopes, eustasy, and margin erosion. *Journal of Geophysical Research*, 96, 6829–6848.
- Miller, K. G., Wright, J. D., Katz, M. E., Wade, B. S., Browning, J. V., Cramer, B. S., & Rosenthal, Y. (2009). Climate threshold at the Eocene–Oligocene transition: Antarctic ice sheet influence on ocean circulation. *Geological Society of America Special Papers*, 452, 169–178.
- Miller, M. D., Simons, M., Adkins, J. F., & Minson, S. E. (2015). The information content of pore fluid $\delta^{18}\text{O}$ and $[\text{Cl}^-]$. *Journal of Physical Oceanography*, 45, 2070–2094.
- Milliman, J. D., Ross, D. A., & Ku, T. L. (1969). Precipitation and lithification of deep-sea carbonates in the Red Sea. *Journal of Sedimentary Petrology*, 39, 724–736.
- Milne, G. A., & Mitrovica, J. X. (1998). Postglacial sea level change on a rotating Earth. *Geophysical Journal International*, 133, 1–19.
- Milne, G. A., & Mitrovica, J. X. (2008). Searching for eustasy in deglacial sea-level histories. *Quaternary Science Reviews*, 27, 2292–2302.
- Mitchell, N. C., Ligi, M., & Rohling, E. J. (2015). Red Sea isolation history suggested by Plio-Pleistocene seismic reflection sequences. *Earth and Planetary Science Letters*, 430, 387–397.
- Mitrovica, J. X., & Milne, G. A. (2003). On post-glacial sea level: I. General theory. *Geophysical Journal International*, 154, 253–267.
- Mitrovica, J. X., & Peltier, W. R. (1991). On postglacial geoid subsidence over the equatorial oceans. *Journal of Geophysical Research*, 96, 20053–20071.
- Mitrovica, J. X., Austermann, J., Coulson, S., Creveling, J. R., Hoggard, M. J., Jarvis, G. T., & Richards, F. D. (2020). Dynamic topography and ice age paleoclimate. *Annual Review of Earth and Planetary Sciences*, 48, 585–621.
- Mitrovica, J. X., Milne, G. A., & Davis, J. L. (2001). Glacial isostatic adjustment on a rotating earth. *Geophysical Journal International*, 147, 562–578.
- Mix, A. C. (1992). The marine oxygen isotope record: Constraints on timing and extent of ice-growth events (120–65 ka). *Geological Society of America Special Papers*, 270, 19–30.

- Mix, A. C., & Ruddiman, W. F. (1984). Oxygen-isotope analyses and Pleistocene ice volumes. *Quaternary Research*, 21, 1–20.
- Modestou, S. E., Leutert, T. J., Fernandez, A., Lear, C. H., & Meckler, A. N. (2020). Warm middle Miocene Indian Ocean bottom water temperatures: Comparison of clumped isotope and Mg/Ca-based estimates. *Paleoceanography and Paleoclimatology*, 35, e2020PA003927.
- Molina-Venegas, R., Aparicio, A., Lavergne, S., & Arroyo, J. (2015). The building of a biodiversity hotspot across a land-bridge in the Mediterranean. *Proceedings of the Royal Society B*, 282, 20151116.
- Mortlock, R. A., Fairbanks, R. G., Chiu, T. C., & Rubenstone, J. (2005). $^{230}\text{Th}/^{234}\text{U}/^{238}\text{U}$ and $^{231}\text{Pa}/^{235}\text{U}$ ages from a single fossil coral fragment by multi-collector magnetic-sector inductively coupled plasma mass spectrometry. *Geochimica et Cosmochimica Acta*, 69, 649–657.
- Moseley, G. E., Smart, P. L., Richards, D. A., & Hoffmann, D. L. (2013). Speleothem constraints on marine isotope stage (MIS) 5 relative sea levels, Yucatan Peninsula, Mexico. *Journal of Quaternary Science*, 28, 293–300.
- Moucha, R., Forte, A. M., Mitrovica, J. X., Rowley, D. B., Quéré, S., Simmons, N. A., & Grand S. P. (2008). Dynamic topography and long-term sea-level variations: There is no such thing as a stable continental platform. *Earth and Planetary Science Letters*, 271, 101–108.
- Mouginot, J., Rignot, E., Scheuchl, B., Fenty, I., Khazendar, A., Morlighem, M., Buzzi, A., & Paden, J. (2015). Fast retreat of Zachariæ Isstrøm, northeast Greenland. *Science*, 350, 1357–1361.
- Mudelsee, M., Bickert, T., Lear, C. H., & Lohmann, G. (2014). Cenozoic climate changes: A review based on time series analysis of marine benthic $\delta^{18}\text{O}$ records. *Reviews of Geophysics*, 52, 333–374.
- Muhs, D. R., Pandolfi, J. M., Simmons, K. R., & Schumann, R. R. (2012a). Sea-level history of past interglacial periods from uranium-series dating of corals, Curaçao, Leeward Antilles islands. *Quaternary Research*, 78, 157–169.
- Muhs, D. R., Simmons, K. R., Kennedy, G. L., Ludwig, K. R., & Groves, L. T. (2006). A cool eastern Pacific Ocean at the close of the Last Interglacial complex. *Quaternary Science Reviews*, 25, 235–262.
- Muhs, D. R., Simmons, K. R., Kennedy, G. L., & Rockwell, T. K. (2002). The last interglacial period on the Pacific Coast of North America: Timing and paleoclimate. *Geological Society of America Bulletin*, 114, 569–592.
- Muhs, D. R., Simmons, K. R., & Steinke, B. (2002b). Timing and warmth of the Last Interglacial period: New U-series evidence from Hawaii and Bermuda and a new fossil compilation for North America. *Quaternary Science Reviews*, 21, 1355–1383.
- Muhs, D. R., Simmons, K. R., Schumann, R. R., Groves, L. T., Mitrovica, J. X., & Laurel, D. (2012b). Sea-level history during the Last Interglacial complex on San Nicolas Island, California: Implications for glacial isostatic adjustment processes, paleozoogeography and tectonics. *Quaternary Science Reviews*, 37, 1–25.
- Muhs, D. R., Simmons, K. R., Schumann, R. R., & Halley, R. B. (2011). Sea-level history of the past two interglacial periods: New evidence from U-series dating of reef corals from south Florida. *Quaternary Science Reviews*, 30, 570–590.
- Müller, I. A., Fernandez, A., Radke, J., van Dijk, J., Bowen, D., Schwieters, J., & Bernasconi, S.M. (2017). Carbonate clumped isotope analyses with the long-integration dual-inlet (LIDI) workflow: Scratching at the lower sample weight boundaries. *Rapid Communications in Mass Spectrometry*, 31, 1057–1066.
- Multer, H. G., Gischler, E., Lundberg, J., Simmons, K. R., & Shinn, E. A. (2002). Key Largo Limestone revisited: Pleistocene shelf-edge facies, Florida Keys, USA. *Facies*, 46, 229–271.

- Naafs, B. D. A., Hefter, J., & Stein, R. (2013). Millennial-scale ice rafting events and Hudson Strait Heinrich (-like) Events during the late Pliocene and Pleistocene: A review. *Quaternary Science Reviews*, 80, 1–28.
- Naish, T. R., & Wilson, G. S. (2009). Constraints on the amplitude of Mid-Pliocene (3.6–2.4 Ma) eustatic sea-level fluctuations from the New Zealand shallow-marine sediment record. *Philosophical Transactions of the Royal Society A*, 367, 169–187.
- Naish, T., Powell, R., Levy, R., Wilson, G., Scherer, R., Talarico, F., Krissek, L., Niessen, F., Pompilio, M., Wilson, T., Carter, L., DeConto, R. M., Huybers, P., McKay, R. M., Pollard, D., Ross, J., Winter, D., Barrett, P., Browne, G., Cody, R., Cowan, E., Crampton, J., Dunbar, G., Dunbar, N., Florindo, F., Gebhardt, C., Graham, I., Hannah, M., Hansaraj, D., Harwood, D., Helling, D., Henrys, S., Hinnov, L., Kuhn, G., Kyle, P., Laufer, A., Maffioli, P., Magens, D., Mandernack, K., McIntosh, W., Millan, C., Morin, R., Ohneiser, C., Paulsen, T., Persico, D., Raine, I., Reed, J., Riesselman, C. R., Sagnotti, L., Schmitt, D., Sjunneskog, C., Strong, P., Taviani, M., Vogel, S., Wilch, T., & Williams, T. (2009). Obliquity-paced Pliocene West Antarctic ice sheet oscillations. *Nature*, 458, 322–328.
- Nakada, M., & Lambeck, K. (1987). Glacial rebound and relative sea-level variations: A new appraisal. *Geophysical Journal International*, 90, 171–224.
- Nakiblogu, S. M., & Lambeck, K. (1980). Deglaciation effects on the rotation of the Earth. *Geophysical Journal International*, 62, 49–58.
- Naranjo, C., García-Lafuente, J., Sammartino, S., Sánchez-Garrido, J. C., Sánchez-Leal, R., & Jesús Bellanco, M. (2017). Recent changes (2004–2016) of temperature and salinity in the Mediterranean outflow. *Geophysical Research Letters*, 44, 5665–5672.
- Niessen, F., Hong, J. K., Hegewald, A., Matthiessen, J., Stein, R., Kim, H., Kim, S., Jensen, L., Jokat, W., Nam, S. I., & Kang, S. H. (2013). Repeated Pleistocene glaciation of the east Siberian continental margin. *Nature Geoscience*, 6, 842–846.
- O'Brien, C. L., Huber, M., Thomas, E., Pagani, M., Super, J. R., Eldera, L. E., & Hull, P. M. (2020). The enigma of Oligocene climate and global surface temperature evolution. *Proceedings of the National Academy of Sciences of the USA*, 117, 25302–25309.
- Oerlemans, J., & van der Veen, C. J. (1984). *Ice Sheets and Climate*. Reidel, Dordrecht, Netherlands, 217 pp.
- Olausson, E. (1965). Evidence of climatic changes in North Atlantic deep-sea cores, with remarks on isotopic paleotemperature analysis. *Progress in Oceanography*, 3, 221–252.
- O'Leary, M. J., Hearty, P. J., & McCulloch, M. T. (2008a). U-series evidence for widespread reef development in Shark Bay during the last interglacial. *Palaeogeography, Palaeoclimatology, Palaeoecology*, 259, 424–435.
- O'Leary, M. J., Hearty, P. J., & McCulloch, M. T. (2008b). Geomorphic evidence of major sea-level fluctuations during marine isotope substage-5e, Cape Cuvier, Western Australia. *Geomorphology*, 102, 595–602.
- O'Leary, M. J., Hearty, P. J., Thompson, W. G., Raymo, M. E., Mitrovica, J. X., & Webster, J. M. (2013). Ice sheet collapse following a prolonged period of stable sea level during the last interglacial. *Nature Geoscience*, 6, 796–800.
- O'Neil, J. R., Clayton, R. N., & Mayeda, T. K. (1969). Oxygen isotope fractionation on divalent metal carbonates. *Journal of Chemical Physics*, 51, 5547–5558.
- PALAEOSSENS (2012). Making sense of paleoclimate sensitivity. *Nature*, 491, 683–691.
- Pawlowicz, R. (2013) Key physical variables in the ocean: Temperature, salinity, and density. *Nature Education Knowledge*, 4, 13.

- Paxman, G. J. G., Gasson, E. G. W., Jamieson, S. S. R., Bentley, M. J., & Ferraccioli, F. (2020). Long-term increase in Antarctic ice sheet vulnerability driven by bed topography evolution. *Geophysical Research Letters*, 47, e2020GL090003.
- Paxman, G. J., Jamieson, S. S., Hochmuth, K., Gohl, K., Bentley, M. J., Leitchenkov, G., & Ferraccioli, F. (2019). Reconstructions of Antarctic topography since the Eocene–Oligocene boundary. *Palaeogeography, Palaeoclimatology, Palaeoecology*, 535, 109346.
- Peak, B. A., Latychev, K., Hoggard, M. J., & Mitrovica, J. X. (2022). Glacial isostatic adjustment in the Red Sea: Impact of 3-D Earth structure. *Quaternary Science Reviews*, 280, 107415.
- Peltier, W. R. (1988). Global sea level and Earth rotation. *Science*, 240, 895–901.
- Peltier, W.R. (1994). Ice age paleotopography. *Science*, 265, 195–201.
- Peltier, W.R. (1998). Postglacial variations in the level of the sea: Implications for climate dynamics and solid-earth geophysics. *Reviews of Geophysics*, 36, 603–689.
- Peltier, W.R. (2004). Global glacial isostasy and the surface of the ice-age earth: The ICE-5G (VM2) model and GRACE. *Annual Review of Earth and Planetary Science*, 32, 111–149.
- Peltier, W. R., & Fairbanks, R. G. (2006). Global ice volume and Last Glacial Maximum duration from an extended Barbados sea-level record. *Quaternary Science Reviews*, 25, 3322–3337.
- Peltier, W. R., Argus, D. F., & Drummond, R. (2015). Space geodesy constrains ice age terminal deglaciation: The global ICE-6G_C (VM5a) model. *Journal of Geophysical Research: Solid Earth*, 120, 450–487.
- Peral, M., Daëron, M., Blamart, D., Bassinot, F., Dewilde, F., Smialkowski, N., Isguder, G., Bonnin, J., Jorissen, F., Kissel, C., Michel, E., Vázquez Riveiros, N., & Waelbroeck, C. (2018). Updated calibration of the clumped isotope thermometer in planktonic and benthic foraminifera. *Geochimica et Cosmochimica Acta*, 239, 1–16.
- Phillips, T., Rajaram, H., & Steffen, K. (2010). Cryo-hydrologic warming: A potential mechanism for rapid thermal response of ice sheets. *Geophysical Research Letters*, 37, L20503.
- Piasecki, A., Bernasconi, S. M., Grauel, A., Hannisdal, B., Ho, S. L., Leutert, T. J., Marchitto, T., Meinicke, N., Tisserand, A., & Meckler, N. (2019). Application of clumped isotope thermometry to benthic foraminifera. *Geochemistry, Geophysics, Geosystems*, 20, 2082–2090.
- Pisias, N. G., & Moore Jr., T. C. (1981). The evolution of Pleistocene climate: A time series approach. *Earth and Planetary Science Letters*, 52, 450–458.
- Pisias, N. G., Martinson, D. G., Moore, T. C., Shackleton, N. J., Prell, W., Hays, J., & Boden, G. (1984). High resolution stratigraphic correlation of benthic oxygen isotopic records spanning the last 300,000 years. *Marine Geology*, 56, 119–136.
- Pollard, D., DeConto, R. M., & Alley, R. B. (2015). Potential Antarctic Ice Sheet retreat driven by hydrofracturing and ice cliff failure. *Earth and Planetary Science Letters*, 412, 112–121.
- Polyak, L., Edwards, M. H., Coakley, B. J., & Jakobsson, M. (2001). Ice shelves in the Pleistocene Arctic Ocean inferred from glaciogenic deep-sea bedforms. *Nature*, 410, 453–457.
- Potter, E.-K., Esat, T. M., Schellmann, G., Radtke, U., Lambeck, K., & McCulloch, M. T. (2004). Suborbital-period sea-level oscillations during marine isotope substages 5a and 5c. *Earth and Planetary Science Letters*, 225, 191–204.
- Prentice, M. L., & Matthews, R. K. (1988). Cenozoic ice-volume history: development of a composite oxygen isotope record. *Geology*, 16, 963–966.

- Pusz, A. E., Thunell, R. C., & Miller, K. G. (2011). Deep water temperature, carbonate ion, and ice volume changes across the Eocene-Oligocene climate transition. *Paleoceanography*, 26, PA2205.
- Qi, X. S., Yuan, N., Comes, H. P., Shakaguchi, S., & Qiu, Y. (2014). A strong 'filter' effect of the East China Sea land bridge for East Asia's temperate plant species: Inferences from molecular phylogeography and ecological niche modelling of *Platycrater arguta* (Hydrangeaceae). *BMC Evolutionary Biology*, 14, 41.
- Rabineau, M., Berné, S., Olivet, J.L., Aslanian, D., Guillocheau, F., & Joseph, P. (2006). Paleo sea levels reconsidered from direct observation of paleoshoreline position during Glacial Maxima (for the last 500,000 yr). *Earth and Planetary Science Letters*, 252, 119–137.
- Raymo, M. E., & Huybers, P. (2008). Unlocking the mysteries of the ice ages. *Nature*, 451, 284–285.
- Raymo, M. E., Kozdon, R., Evans, D., Lisiecki, L., & Ford, H. L. (2018). The accuracy of mid-Pliocene $\delta^{18}\text{O}$ -based ice volume and sea level reconstructions. *Earth-Science Reviews*, 177, 291–302.
- Raymo, M. E., Mitrovica, J. X., O'Leary, M. J., De Conto, R. M., & Hearty, P.J. (2011). Departures from eustasy in Pliocene sea-level records. *Nature Geoscience*, 4, 328–332.
- Rea, B. R., Newton, A. M., Lamb, R. M., Harding, R., Bigg, G. R., Rose, P., Spagnolo, M., Huuse, M., Cater, J. M., Archer, S., Buckley, F., Halliyeva, M., Huuse, J., Cornwell, D. G., Brocklehurst, S. H., & Howell, J. A. (2018). Extensive marine-terminating ice sheets in Europe from 2.5 million years ago. *Science Advances*, 4, eaar8327.
- Reiss, Z., & Hottinger, L. (1984). The Gulf of Aqaba, ecological micropaleontology. *Ecological Studies*, 50. Springer, Berlin, 354 pp.
- Riker-Coleman, K. E., Gallup, C. D., Wallace, L. M., Webster, J. M., Cheng, H., & Edwards, R. L. (2006). Evidence of Holocene uplift in east New Britain, Papua New Guinea. *Geophysical Research Letters*, 33, L18612.
- Roberts, A. P., Rohling, E. J., Grant, K. M., Larrasoana, J. C., & Liu, Q. (2011). Atmospheric dust variability from Arabia and China over the last 500,000 years. *Quaternary Science Reviews*, 30, 3537–3541.
- Rodrigues, T., Alonso-García, M., Hodell, D. A., Rufino, M., Naughton, F., Grimalt, J. O., Voelker, A. H. L., & Abrantes, F. (2017). A 1-Ma record of sea surface temperature and extreme cooling events in the North Atlantic: A perspective from the Iberian Margin. *Quaternary Science Reviews*, 172, 118–130.
- Rohling, E. J. (1994a). Review and new aspects concerning the formation of Mediterranean sapropels. *Marine Geology*, 122, 1–28.
- Rohling, E.J. (1994b). Glacial conditions in the Red Sea. *Paleoceanography*, 9, 653–660.
- Rohling, E. J. (1999). Environmental controls on Mediterranean salinity and $\delta^{18}\text{O}$. *Paleoceanography*, 14, 706–715.
- Rohling, E. J., & Bigg, G. R. (1998). Paleo-salinity and $\delta^{18}\text{O}$: a critical assessment. *Journal of Geophysical Research*, 103, 1307–1318.
- Rohling, E. J., & Bryden, H. L. (1994). Estimating past changes in the eastern Mediterranean freshwater budget, using reconstructions of sea level and hydrography. *Proceedings of the Koninklijke Nederlandse Akademie van Wetenschappen Serie B*, 97, 201–217.
- Rohling, E. J., & Cooke, S. (1999). Stable oxygen and carbon isotope ratios in foraminiferal carbonate, Chapter 14 in Sen Gupta, B. K. (Ed.) *Modern Foraminifera*, Kluwer Academic, Dordrecht, Netherlands, pp. 239–258.

- Rohling, E. J., Fenton, M., Jorissen, F. J., Bertrand, P., Ganssen, G., & Caulet, J. P. (1998). Magnitudes of sea-level lowstands of the past 500,000 years. *Nature*, 394, 162–165.
- Rohling, E. J., Foster, G. L., Grant, K. M., Marino, G., Roberts, A. P., Tamsiea, M. E., & Williams, F. (2014). Sea-level and deep-sea-temperature variability over the past 5.3 million years. *Nature*, 508, 477–482.
- Rohling, E. J., Grant, K., Bolshaw, M., Roberts, A. P., Siddall, M., Hemleben, Ch., & Kucera, M. (2009). Antarctic temperature and global sea level closely coupled over the past five glacial cycles. *Nature Geoscience*, 2, 500–504.
- Rohling, E. J., Grant, K. M., Roberts, A. P., & Larrasoana, J. C. (2013a). Palaeoclimate variability in the Mediterranean and Red Sea regions during the last 500,000 years: Implications for hominin migrations. *Current Anthropology*, 54, S183–S201.
- Rohling, E. J., Haigh, I. D., Foster, G. L., Roberts, A. P., & Grant, K. M. (2013b). A geological perspective on potential future sea-level rise. *Scientific Reports*, 3, 3461.
- Rohling, E. J., Hibbert, F. D., Grant, K. M., Galaasen, E. V., Irvani, N., Kleiven, H. F., Marino, G., Ninnemann, U., Roberts, A. P., Rosenthal, Y., Schulz, H., Williams, F. H., & Yu, J. (2019). Asynchronous Antarctic and Greenland ice-volume contributions to the last interglacial sea-level highstand. *Nature Communications*, 10, 5040.
- Rohling, E. J., Hibbert, F. D., Williams, F. H., Grant, K. M., Marino, G., Foster, G. L., Hennekam, R., de Lange, G. J., Roberts, A. P., Yu, J., Webster, J. M., & Yokoyama, Y. (2017). Differences between the last two glacial maxima and implications for ice-sheet, $\delta^{18}\text{O}$, and sea-level reconstructions. *Quaternary Science Reviews*, 176, 1–28.
- Rohling, E. J., Marino, G., & Grant, K. M. (2015). Mediterranean climate and oceanography, and the periodic development of anoxic events (sapropels). *Earth-Science Reviews*, 143, 62–97.
- Rohling, E. J., Marsh, R., Wells, N. C., Siddall, M., & Edwards, N. (2004). Similar melt-water contributions to glacial sea-level variability from Antarctic and northern ice sheets. *Nature*, 430, 1016–1021.
- Rohling, E. J., Medina-Elizalde, M., Shepherd, J. G., Siddall, M., & Stanford, J. D. (2012). Sea surface and high-latitude temperature sensitivity to radiative forcing of climate over several glacial cycles. *Journal of Climate*, 25, 1635–1656.
- Rohling, E. J., Marino, G., Foster, G. L., Goodwin, P. A., von der Heydt, A. S., & Köhler, P. (2018). Comparing climate sensitivity, past and present. *Annual Reviews of Marine Science*, 10, 261–288.
- Rohling, E. J., Sprovieri, M., Cane, T. R., Casford, J. S. L., Cooke, S., Bouloubassi, I., Emeis, K. C., Schiebel, R., Hayes, A., Jorissen, F. J., & Kroon, D. (2004). Reconstructing past planktic foraminiferal habitats using stable isotope data: A case history for Mediterranean sapropel S5. *Marine Micropaleontology*, 50, 89–123.
- Rohling, E. J., Yu, J., Heslop, D., Foster, G. L., Opdyke, B., & Roberts, A. P. (2021). Sea-level and deep-sea temperature reconstructions suggest quasi-stable states and critical transitions over the past 40 million years. *Science Advances*, 7, eabf5326.
- Rolland, N. (2013). The Early Pleistocene human dispersals in the Circum-Mediterranean Basin and initial peopling of Europe: Single or multiple pathways? *Quaternary International*, 316, 59–72.
- Rosignol-Strick, M. (1985). Mediterranean Quaternary sapropels, an immediate response of the African monsoon to variations of insolation. *Palaeogeography, Palaeoclimatology, Palaeoecology*, 49, 237–263.
- Rosignol-Strick, M. (1987). Rainy periods and bottom water stagnation initiating brine accumulation and metal concentrations: 1. The Late Quaternary. *Paleoceanography*, 2, 333–360.

- Rossignol-Strick, M. (1983). African monsoons, an immediate climate response to orbital insolation. *Nature*, 30, 446–449.
- Rossignol-Strick, M., Nesteroff, V., Olive, P., & Vergnaud-Grazzini, C. (1982). After the deluge; Mediterranean stagnation and sapropel formation. *Nature*, 295, 105–110.
- Rovere, A., Pappalardo, M., Richiano, S., Aguirre, M., Sandstrom, M. R., Hearty, P. J., Austermann, J., Castellanos, I., & Raymo, M. E. (2020). Higher than present global mean sea level recorded by an Early Pliocene intertidal unit in Patagonia (Argentina). *Communications Earth and Environment*, 1, 68.
- Rovere, A., Raymo, M. E., Mitrovica, J. X., Hearty, P. J., O’Leary, M. J., & Inglis, J. D. (2014). The Mid-Pliocene sea-level conundrum: Glacial isostasy, eustasy and dynamic topography. *Earth and Planetary Science Letters*, 387, 27–33.
- Rowley, D. B., Forte, A. M., Moucha, R., Mitrovica, J. X., Simmons, N. A., Grand, S. P. (2013). Dynamic topography change of the Eastern United States since 3 million years ago. *Science*, 340, 1560–1563.
- Ryb, U., & Eiler, J. M. (2018). Oxygen isotope composition of the Phanerozoic ocean and a possible solution to the dolomite problem. *Proceedings of the National Academy of Sciences of the USA*, 115, 6602–6607.
- Rychert, C. A., Harmon, N., Constable, S., & Wang, S. (2020). The nature of the lithosphere-aesthenosphere boundary. *Journal of Geophysical Research: Solid Earth*, 125, e2018JB016463.
- Sánchez-Montes, M. L., McClymont, E. L., Lloyd, J. M., Müller, J., Cowan, E. A., & Zorzi, C. (2020). Late Pliocene Cordilleran Ice Sheet development with warm northeast Pacific sea surface temperatures. *Climate of the Past*, 16, 299–313.
- Sangiorgi, F., Bijl, P. K., Passchier, S., Salzmann, U., Schouten, S., McKay, R., Cody, R. D., Pross, J., van de Flierdt, T., Bohaty, S. M., Levy, R., Williams, T., Escutia, C., & Brinkhuis, H. (2018). Southern Ocean warming and Wilkes Land ice sheet retreat during the mid-Miocene. *Nature Communications*, 9, 317.
- Satow, C., Tomlinson, E. L., Grant, K. M., Albert, P. G., Smith, V. C., Manning, C. J., Ottoloni, L., Wulf, S., Rohling, E. J., Lowe, J. J., Blockley, S. P., & Menzies, M. A. (2015). A new contribution to the Late Quaternary tephrostratigraphy of the Mediterranean: Aegean Sea core LC21. *Quaternary Science Reviews*, 117, 96–112.
- Sauermilch, I., Whittaker, J. M., Klocker, A., Munday, D. R., Hochmuth, K., Bijl, P. K., & LaCasce, J. H. (2021). Gateway-driven weakening of ocean gyres leads to Southern Ocean cooling. *Nature Communications*, 12, 1–8.
- Schellmann, G., & Radtke, U. (2004). A revised morpho- and chronostratigraphy of the late and middle Pleistocene coral reef terraces on Southern Barbados (West Indies). *Earth-Science Reviews*, 64, 157–187.
- Schmid, T. W., & Bernasconi, S. M. (2010). An automated method for ‘clumped-isotope’ measurements on small carbonate samples. *Rapid Communications in Mass Spectrometry*, 24, 1955–1963.
- Schoell, M., & Risch, H. (1976). Oxygen and carbon isotope analyses on planktonic foraminifera of core VA 01-188 P (Southern Red Sea). *Geologisches Jahrbuch*, D17, 15–32.
- Schrag, D. P., Hampt, G., & Murray, D. W. (1996). Pore fluid constraints on the temperature and oxygen isotopic composition of the glacial ocean. *Science*, 272, 1930–1932.
- Shackleton, N. J. (1967). Oxygen isotope analyses and Pleistocene temperatures reassessed. *Nature*, 215, 15–17.

- Shackleton, N. J. (1987). Oxygen isotopes, ice volume and sea-level. *Quaternary Science Reviews*, 6, 183–190.
- Shackleton, N. J., & Opdyke, N. D. (1973). Oxygen isotope and palaeomagnetic stratigraphy of Equatorial Pacific core V28-238: Oxygen isotope temperatures and ice volumes on a 10^5 year and 10^6 year scale. *Quaternary Research*, 3, 39–55.
- Shackleton, N. J., & Opdyke, N. D. (1976). Oxygen-isotope and paleomagnetic stratigraphy of Pacific core V28-239 Late Pliocene to latest Pleistocene. *Geological Society of America Memoirs*, 145, 449–463.
- Shakun, J. D., Lea, D. W., Lisiecki, L. E., & Raymo, M. E. (2015). An 800-kyr record of global surface ocean $\delta^{18}\text{O}$ and implications for ice volume-temperature coupling. *Earth and Planetary Science Letters*, 426, 58–68.
- Shennan, I., & Horton, B. P. (2002). Holocene land- and sea-level changes in Great Britain. *Journal of Quaternary Science*, 17, 511–526.
- Shennan, I., Long, A. J., & Horton, B. P. (2015). *Handbook of sea-level research*. American Geophysical Union, John Wiley and Sons Ltd., 578 pp.
- Sherman, C. E., Fletcher, C. H., & Rubin, K. H. (1999). Marine and meteoric diagenesis of Pleistocene carbonates from a nearshore submarine terrace, Oahu, Hawaii. *Journal of Sedimentary Research*, 69, 1083–1097.
- Sherwood, S., Webb, M. J., Annan, J. D., Armour, K. C., Forster, P. M., Hargreaves, J. C., Hegerl, G., Klein, S. A., Marvel, K. D., Rohling, E. J., Watanabe, M., Andrews, T., Braconnot, P., Bretherton, C. S., Foster, G. L., Hausfather, Z., von der Heydt, A. S., Knutti, R., Mauritsen, T., Norris, J. R., Proistosescu, C., Rugenstein, M., Schmidt, G. A., Tokarska, K. B., & Zelinka, M. D. (2020). An assessment of Earth's climate sensitivity using multiple lines of evidence. *Reviews of Geophysics*, 58, e2019RG000678.
- Shevenell, A. E., Kennett, J. P., & Lea, D. W. (2008). Middle Miocene ice sheet dynamics, deep-sea temperatures, and carbon cycling: A Southern Ocean perspective. *Geochemistry, Geophysics, Geosystems*, 9, GC001736.
- Siddall, M., Hönisch, B., Waelbroeck, C., & Huybers, P. (2010). Changes in deep Pacific temperature during the mid-Pleistocene transition and Quaternary. *Quaternary Science Reviews*, 29, 170–181.
- Siddall, M., Rohling, E. J., Almogi-Labin, A., Hemleben, Ch., Meischner, D., Schmeltzer, I., & Smeed, D. A. (2003). Sea-level fluctuations during the last glacial cycle. *Nature*, 423, 853–858.
- Siddall, M., Rohling, E. J., & Arz, H.W. (2008a). Convincing evidence for rapid ice sheet growth during the last glacial period, in: Kienast, M., Lynch-Stieglitz, J., Newman, L., & Kiefer, T. (eds.). *PAGES News*, 16, 15–16.
- Siddall, M., Rohling, E. J., Thompson, W. G., & Waelbroeck, C. (2008b). MIS 3 sea-level fluctuations: data synthesis and new outlook. *Reviews of Geophysics*, 46, RG4003.
- Siddall, M., Smeed, D. A., Hemleben, Ch., Rohling, E. J., Schmeltzer, I., & Peltier, W. R. (2004). Understanding the Red Sea response to sea level. *Earth and Planetary Science Letters*, 225, 421–434.
- Siddall, M., Smeed, D., Mathiessen, S., & Rohling, E. J. (2002). Modelling the seasonal cycle of the exchange flow in Bab-el-Mandab (Red Sea). *Deep-Sea Research I*, 49, 1551–1569.
- Sivan D., Sisma-Ventura G., Greenbaum N., Bialik O. M., Williams, F. H., Tamisiea, M. E., Rohling, E. J., Frumkin, A., Avnaim-Katav S., Shtienberg G., & Stein, M. (2016). Eastern Mediterranean sea levels through the last interglacial from a coastal-marine sequence in northern Israel. *Quaternary Science Reviews*, 145, 204–225.

- Sivan, D., Wdowinski, S., Lambach, K., Galili, E., & Raban, A (2001). Holocene sea-level changes along the Mediterranean coast of Israel, based on archaeological observations and numerical model. *Palaeogeography Palaeoclimatology Palaeoecology*, 167, 101–117.
- Sivan, D., Lambeck, K., Toueg, R., Raban, A., Porat, Y., & Shirman, B. (2004). Ancient coastal wells of Caesarea Maritima, Israel, an indicator for sea level changes during the last 2000 years. *Earth and Planetary Science Letters*, 222, 315–330.
- Skinner, L. C., & Shackleton, N. J. (2005). Deconstructing Terminations I and II: revisiting the glacioeustatic paradigm based on deep-water temperature estimates. *Quaternary Science Reviews*, 25, 3312–3321.
- Smeed, D. A. (1997). Seasonal variation of the flow in the strait of Bab al Mandab. *Oceanologica Acta*, 20, 773–781.
- Smeed, D. A. (2000). Hydraulic control of three-layer exchange flows: application to the Bab el Mandab. *Journal of Physical Oceanography*, 30, 2574–2588.
- Sosdian, S., & Rosenthal, Y. (2009). Deep-sea temperature and ice volume changes across the Pliocene-Pleistocene climate transitions. *Science*, 325, 306–310.
- Speed, R. C., & Cheng, H. (2004). Evolution of marine terraces and sea level in the last interglacial, Cave Hill, Barbados. *Geological Society of America Bulletin*, 116, 219–232.
- Spratt, R. M., & Lisiecki, L. E. (2016). A Late Pleistocene sea level stack. *Climate of the Past*, 12, 1079–1092.
- Stanford, J. D., Hemingway, R., Rohling, E. J., Challenor, P.G., Medina-Elizalde, M., & Lester, A. J. (2011). Sea-level probability for the last deglaciation: a statistical analysis of far-field records. *Global and Planetary Change*, 79, 193–203.
- Stap, L. B., Van De Wal, R. S. W., de Boer, B., Bintanja, R., & Lourens, L. J. (2016). The MMCO-EOT conundrum: Same benthic $\delta^{18}\text{O}$, different CO_2 . *Paleoceanography*, 31, 1270–1282.
- Stap, L., van de Wal, R. S. W., de Boer, B., Köhler, P., Hoencamp, J. H., Lohmann, G., Tüenter, E., & Lourens, L. J. (2018). Modeled influence of land ice and CO_2 on polar amplification and paleoclimate sensitivity during the past 5 million years. *Paleoceanography and Paleoclimatology*, 33, 381–394.
- Stein, M., Wasserburg, G. J., Aharon, P., Chen, J. H., Zhu, Z. R., Bloom, A., & Chappell, J. (1993). TIMS U-series dating and stable isotopes of the last interglacial event in Papua New Guinea. *Geochemica et Cosmochemica Acta*, 57, 2541–2554.
- Steinthorsdottir, M., Coxall, H. K., de Boer, A. M., Huber, M., Barbolini, N., Bradshaw, C. D., Burls, N. J., Feakins, S. J., Gasson, E., Henderiks, J., Holbourn, A. E., Kiel, S., Kohn, M. J., Knorr, G., Kürschner, W. M., Lear, C. H., Liebrand, D., Lunt, D. J., Mörs, T., Pearson, P. N., Pound, M. J., Stoll, H., & Strömberg, C. A. E. (2021). The Miocene: The future of the past. *Paleoceanography and Paleoclimatology*, 36, e2020PA004037.
- Stibal, M., Box, J. E., Cameron, K. A., Langen, P. L., Yallop, M. L., Mottram, R. H., Khan, A. L., Molotoch, N. P., Christmas, N. A. M., Calì Quaglia, F., Remias, D., Smeets, C. J. P., van den Broeke, M. R., Ryan, J. C., Hubbard, A., Tranter, M., van As, D., & Ahlstrøm, A. P. (2017). Algae drive enhanced darkening of bare ice on the Greenland ice sheet. *Geophysical Research Letters*, 44, 11463–11471.
- Stirling, C. H. (1996). High-precision U-series dating of corals from Western Australia: Implications for Last Interglacial sea levels. *PhD Thesis*. The Australian National University.
- Stirling, C. H., Esat, T. M., Lambeck, K., & McCulloch, M. T. (1998). Timing and duration of the last interglacial: Evidence for a restricted interval of widespread coral reef growth. *Earth and Planetary Science Letters*, 160, 745–762.

- Stirling, C. H., Esat, T. M., McCulloch, M. T., & Lambeck, K. (1995). High-precision U-series dating of corals from Western Australia and implications for the timing and duration of the Last Interglacial. *Earth and Planetary Science Letters*, 135, 115–130.
- Stirling, C. H., Esat, T. M., Lambeck, K., McCulloch, M. T., Blake, S. G., Lee, D. C., & Halliday, A. N. (2001). Orbital forcing of the marine isotope stage 9 interglacial. *Science*, 291, 290–293.
- Sun, D., Gagan, M. K., Cheng, H., Scott-Gagan, H., Dykoski, C. A., Edwards, R. L., & Su, R. (2005). Seasonal and interannual variability of the Mid-Holocene East Asian monsoon in coral $\delta^{18}\text{O}$ records from the South China Sea. *Earth and Planetary Science Letters*, 237, 69–84.
- Tabor, C. R., & Poulsen, C. J. (2016). Simulating the mid-Pleistocene transition through regolith removal. *Earth and Planetary Science Letters*, 434, 231–240.
- Tamisiea, M. E., & Mitrovica, J. X. (2011). The moving boundaries of sea level change: Understanding the origins of geographic variability. *Oceanography*, 24, 24–39.
- Thomas, A. L., Fujita, K., Iryu, Y., Bard, E., Cabioch, G., Camoin, G., Cole, J. E., Deschamps P., Durand, N., Hamelin, B., Heindel, K., Henderson, G. M., Mason, A. J., Matsuda, H., Menabreaz, L., Omori, A., Quinn, T., Sakai, S., Sato, T., Sugihara, K., Takahashi, Y., Thouveny, N., Tudhope, A. W., Webster, J., Westphal, H., & Yokoyama, Y. (2012). Assessing subsidence rates and paleo water-depths for Tahiti reefs using U-Th chronology of altered corals. *Marine Geology*, 295–298, 86–94.
- Thomas, A. L., Henderson, G. M., Deschamps, P., Yokoyama, Y., Mason, A. J., Bard, E., Hamelin, B., Durand, N., & Camoin, G. (2009). Penultimate deglacial sea-Level timing from Uranium/Thorium dating of Tahitian corals. *Science*, 324, 1186–1189.
- Thompson, W. G., & Goldstein, S. L. (2005). Open-system coral ages reveal persistent suborbital sea-level cycles. *Science*, 308, 401–404.
- Thompson, W. G., Curran, H. A., Wilson, M. A., & White, B. (2011). Sea-level oscillations during the last interglacial highstand recorded by Bahamas corals. *Nature Geoscience*, 4, 684–687.
- Thompson, W. G., Spiegelman, M. W., Goldstein, S. L., & Speed, R. C. (2003). An open-system model for U-series age determinations of fossil corals. *Earth and Planetary Science Letters*, 210, 365–381.
- Thunell, R. C., Locke, S. M., & Williams, D. F. (1988). Glacio-eustatic sea-level control on Red Sea salinity. *Nature*, 334, 601–604.
- Toscano, M., & Lundberg, J. (1998). Early Holocene sea-level record from submerged fossil reefs on the southeast Florida margin. *Geology*, 26, 255–258.
- Truffer, M. & Fahnestock, M. (2007). Climate change: rethinking ice sheet time scales. *Science*, 315, 1508–1510.
- Tziperman, E., & Gildor, H. (2003). On the mid-Pleistocene transition to 100-kyr glacial cycles and the asymmetry between glaciation and deglaciation times. *Paleoceanography*, 18, 1001.
- Uchikawa, J., & Zeebe, R. E. (2010). Examining possible effects of seawater pH decline on foraminiferal stable isotopes during the Paleocene-Eocene Thermal Maximum, *Paleoceanography*, 25, PA2216.
- Umgiesser, G., Anderson, J. B., Artale, V., Breil, M., Gualdi, S., Lionello, P., Marinova, N., Orlic, M., Pirazzoli, P., Rahmstorf, S., Raicich, F., Rohling, E., Tomasin, A., Tsimplis, M., & Vellinga, P. (2011). *From global to regional: Local sea level rise scenarios - focus on the Mediterranean Sea and the Adriatic Sea*. Report of Workshop organized by UNESCO Venice office and ISMAR-CNR, 22-23 November 2010, Venice, Italy, UNESCO (Venice), 28 pp.
- Urey, H. C. (1947). The thermodynamic properties of isotopic substances. *Journal of the Chemical Society*, 1947, 562–581.

- Urey, H. C. (1953). Revised carbonate-water isotopic temperature scale. *Geological Society of America Bulletin*, 64, 1315–1325.
- van As, D., Bech Mikkelsen, A., Holtegaard Nielsen, M., Box, J. E., Claesson Liljedahl, L., Lindbäck, K., Pitcher, L., & Hasholt, B. (2017). Hypsometric amplification and routing moderation of Greenland ice sheet meltwater release. *The Cryosphere*, 11, 1371–1386.
- van de Plassche, O. (1986). *Sea-level research: A manual for the collection and evaluation of data*. Geo Books.
- Veeh, H. H., Veevers, J. J. (1970). Sea level at -175 m off the Great Barrier Reef 13,600 to 17,000 year ago. *Nature*, 226, 536–537.
- Vergnaud-Grazzini, C. (1985). Mediterranean late Cenozoic stable isotope record: stratigraphic and paleoclimatic implications. In: Stanley, D. J., & Wezel, F. C. (Eds.), *Geological Evolution of the Mediterranean Basin*. Springer-Verlag, New York, pp. 413–451.
- Vermeersen, L. L. A., & Schotman, H. H. A. (2009). Constraints on glacial isostatic adjustment from GOCE and sea level data. *Pure and Applied Geophysics*, 166, 1261–1281.
- Vezina, J., Jones, B., & Ford, D. (1999). Sea-level highstands over the last 500,000 years; Evidence from the Ironshore Formation on Grand Cayman, British West Indies. *Journal of Sedimentary Research*, 69, 317–327.
- von der Heydt, A. S., Dijkstra, H. A., van de Wal, R. S. W., Caballero, R., Crucifix, M., Foster, G. L., Huber, M., Köhler, P., Rohling, E. J., Valdes, P. J., Ashwin, P., Bathiany, S., Berends, T., van Bree, L. G. J., Ditlevsen, P., Ghil, M., Haywood, A., Katsav, J., Lohmann, G., Lohmann, J., Lucarini, V., Marzocchi, A., Pälike, H., Ruvalcaba Baroni, I., Simon, D., Sluijs, A., Stap, L. B., Tantet, A., Viebahn, J., & Ziegler, M. (2016). Lessons on climate sensitivity from past climate changes. *Current Climate Change Reports*, 2, 148–158.
- Waelbroeck, C., Labeyrie, L., Michel, E., Duplessy, J. C., McManus, J. F., Lambeck, K., Balbon, E., & Labracherie, M. (2002). Sea-level and deep water temperature changes derived from benthonic foraminifera isotopic records. *Quaternary Science Reviews*, 21, 295–305.
- Wainer, K. A. I., Rowe, M. P., Thomas, A. L., Mason, A. J., Williams, B., Tamsiea, M. E., Williams, F. H., Düsterhus, A., & Henderson, G. M. (2017). Speleothem evidence for MIS 5c and 5a sea level above modern level at Bermuda. *Earth and Planetary Science Letters*, 457, 325–334.
- Walter, R. C., Buffler, R. T., Bruggemann, J. H., Guillaume, M. M., Berhe, S. M., Negassi, B., Libsekal, Y., Cheng, H., Edwards, R. L., Von Cosel, R., & Gagnon, M. (2000). Early human occupation of the Red Sea coast of Eritrea during the last interglacial. *Nature*, 405, 65–69.
- Warny, S., Askin, R., Hannah, M., Mohr, B., Raine, J., Harwood, D., Florindo, F., & the SMS Science Team (2009). Palynomorphs from a sediment core reveal a sudden remarkably warm Antarctica during the middle Miocene. *Geology*, 37, 955–958.
- Webb, P. N., & Harwood, D. (1991). Late Cenozoic glacial history of the Ross embayment, Antarctica. *Quaternary Science Reviews*, 10, 215–223.
- Webster, J. W., Braga, J.-C., Humblet, M., Potts, D. C., Iryu, Y., Yokoyama, Y., Fujita, K., Bourillot, R., Esat, T. M., Fallon, S., Thompson, W. G., Thomas, A. L., Kan, H., McGregor, H. V., Hinestrosa, G., Obrochta, S. P., & Loughheed, B. C. (2018). Response of the Great Barrier Reef to sea-level and environmental changes over the past 30,000 years. *Nature Geoscience*, 11, 426–432.
- Weldeab, S., Arce, A., & Kasten, S. (2016). Mg/Ca- $\Delta\text{CO}_{3\text{porewater}}^{2-}$ -temperature calibration for *Globobulimina* spp.: A sensitive paleothermometer for deep-sea temperature reconstruction. *Earth and Planetary Science Letters*, 438, 95–102.

- Werner, F., & Lange, K. (1975). A bathymetric survey of the sill area between the Red Sea and Gulf of Aden. *Geologisches Jahrbuch*, *D13*, 125–130.
- Westerhold, T., Marwan, N., Drury, A. J., Liebrand, D., Agnini, C., Anagnostou, E., Barnet, J. S. K., Bohaty, S. M., De Vleeschouwer, D., Florindo, F., Frederichs, T., Hodell, D. A., Holbourn, A. E., Kroon, D., Lauretano, V., Littler, K., Lourens, L. J., Lyle, M., Pälike, H., Röhl, U., Tian, J., Wilkens, R. H., Wilson, P. A., & Zachos, J. C. (2020). An astronomically dated record of Earth's climate and its predictability over the last 66 million years. *Science*, *369*, 1383–1387.
- Whitehouse, P. L. (2018). Glacial isostatic adjustment modeling: Historical perspectives, recent advances, and future directions. *Earth Surface Dynamics*, *6*, 401–429.
- Wilkens, R. H., Westerhold, T., Drury, A. J., Lyle, M., Gorgas, T., & Tian, J. (2017). Revisiting the Ceara Rise, equatorial Atlantic Ocean: isotope stratigraphy of ODP Leg 154 from 0 to 5 Ma. *Climate of the Past*, *13*, 779–793.
- Willeit, M., Ganopolski, A., Calov, R., & Brovkin, V. (2019). Mid-Pleistocene transition in glacial cycles explained by declining CO₂ and regolith removal. *Science Advances*, *5*, eaav7337.
- Wilson, D. S., Jamieson, S. S. R., Barrett, P. J., Leitchenkov, G., Gohl, K., & Larter, R. D. (2012). Antarctic topography at the Eocene-Oligocene boundary. *Palaeogeography, Palaeoclimatology, Palaeoecology*, *335*, 24–34.
- Wilson, D. S., Pollard, D., DeConto, R. M., Jamieson, S. S., & Luyendyk, B. P. (2013). Initiation of the West Antarctic Ice Sheet and estimates of total Antarctic ice volume in the earliest Oligocene. *Geophysical Research Letters*, *40*, 4305–4309.
- Wilson, G. S. (1995). The Neogene East Antarctic ice sheet: a dynamic or stable feature? *Quaternary Science Reviews*, *14*, 101–123.
- Winnick, M. J., & Caves, J. K. (2015). Oxygen isotope mass-balance constraints on Pliocene sea level and East Antarctic Ice Sheet stability. *Geology*, *43*, 879–882.
- Winter, A., Almogi-Labin, A., Erez, Y., Halicz, E., Luz, B., & Reiss, Z. (1983). Salinity tolerance of marine organisms deduced from Red Sea Quaternary record. *Marine Geology*, *53*, M17–M22.
- Wood, M., Rignot, E., Fenty, I., An, L., Bjørk, A., van den Broeke, M., Cai, C., Kane, E., Mene-Menlis, D., Millan, R., Morlighem, M., Mouginot, J., Noël, B., Scheuchl, B., Velicogna, I., Willis, J., & Zhang, H. (2021). Ocean forcing drives glacier retreat in Greenland. *Science Advances*, *7*, eaba7282.
- Woodroffe, S. A., & Horton, B.P. (2005). Holocene sea-level changes in the Indo-Pacific. *Journal of Asian Earth Sciences*, *25*, 29–43.
- Woodroffe, C. D., & Webster, J. M. (2014). Coral reefs and sea-level change. *Marine Geology*, *352*, 248–267.
- Yamamoto, M., Clemens, S. C., Seki, O., Tsuchiya, Y., Huang, Y., O'ishi, R., & Abe-Ouchi, A. (2022). Increased interglacial atmospheric CO₂ levels followed the mid-Pleistocene Transition. *Nature Geoscience*, *15*, 307–313.
- Yan, Y., Bender, M. L., Brook, E.J., Clifford, H. M., Kemeny, P. C., Kurbatov, A. V., Mackay, S., Mayewski, P. A., Ng, J., Severinghaus, J. P., & Higgins, J. A. (2019). Two-million-year-old snapshots of atmospheric gases from Antarctic ice. *Nature*, *574*, 663–666.
- Yehudai, M., Kim, J., Pena, L. D., Jaume-Seguí, M., Knudson, K. P., Bolge, L., Malinverno, A., Bickert, T., & Goldstein, S. L. (2021). Evidence for a Northern Hemispheric trigger of the 100,000-y glacial cyclicity. *Proceedings of the National Academy of Sciences of the USA*, *118*, e2020260118.
- Yokoyama, Y., & Purcell, A. (2021). On the geophysical processes impacting palaeo-sea-level observations. *Geoscience Letters*, *8*, 1–19.

- Yokoyama, Y., De Deckker, P., Lambeck, K., Johnston, P., & Fifield, L. K. (2001b). Sea-level at the Last Glacial Maximum: Evidence from northwestern Australia to constrain ice volumes for Oxygen Isotope Stage 2. *Palaeogeography, Palaeoclimatology, Palaeoecology*, 165, 281–297.
- Yokoyama, Y., Esat, T. M., & Lambeck, K. (2001a). Coupled climate and sea-level changes deduced from Huon Peninsula coral terraces of the last ice age. *Earth and Planetary Science Letters*, 193, 579–587.
- Yokoyama, Y., Esat, T. M., Thompson, W. G., Thomas, A. L., Webster, J., Miyairi, Y., Sawada, C., Aze, T., Matsuzaki, H., Okuno, J., Fallon, S., Braga, J.-C., Humblet, M., Iryu, Y., Potts, D., Fujita, K., Suzuki, A., & Kan, H. (2018). Rapid glaciation and a two-step sea level plunge into the last glacial maximum. *Nature*, 559, 603–610.
- Yokoyama, Y., Lambeck, K., DeDeckker, P., Johnston, P., & Fifield, L. K. (2000). Timing of the Last Glacial Maximum from observed sea-level minima. *Nature*, 406, 713–716.
- Yokoyama, Y., Purcell, A. Marshall, J. F., & Lambeck, K. (2006). Sea-level during the early deglaciation period in the Great Barrier Reef, Australia. *Global and Planetary Change*, 53, 147–153.
- Young, A., Flament, N., Maloney, K., Williams, S., Matthews, K., Zahirovic, S., & Müller, R. D. (2019). Global kinematics of tectonic plates and subduction zones since the late Paleozoic era. *Geoscience Frontiers*, 10, 989–1013.
- Yu, J., & Broecker, W. S. (2010). Comment on “Deep-sea temperature and ice volume changes across the Pliocene-Pleistocene climate transitions”. *Science*, 328, 1480.
- Yu, J., & Elderfield, H. (2008). Mg/Ca in the benthic foraminifera *Cibicides wuellerstorfi* and *Cibicides mundulus*: Temperature versus carbonate ion saturation. *Earth and Planetary Science Letters*, 276, 129–139.
- Zachos, J., Pagani, M., Sloan, L., Thomas, E., & Billups, K. (2001). Trends, rhythms, and aberrations in global climate 65 Ma to present. *Science*, 292, 686–693.
- Zachos, J. C., Dickens, G. R., & Zeebe, R. E. (2008). An early Cenozoic perspective on greenhouse warming and carbon-cycle dynamics. *Nature*, 451, 279–283.
- Zazo, C., Goy, J. L., Dabrio, C. J., Soler, V., Hillaire-Marcel, C., Ghaleb, B., González-Delgado, J. A., Bardají, T., & Cabero, A. (2007). Quaternary marine terraces on Sal Island (Cape Verde archipelago). *Quaternary Science Reviews*, 26, 876–893.
- Zhao, J., & Yu, K. (2002). Timing of Holocene sea-level highstands by mass spectrometric U-series ages of a coral reef from Leizhou Peninsula, South China Sea. *Chinese Science Bulletin*, 47, 348–352.
- Zhu, Z. R., Wyrwoll, K. H., Collins, L. B., Chen, J. H., Wasserburg, G. J., & Eisenhauer, A. (1993). High-precision U-series dating of Last Interglacial events by mass spectrometry: Houtman Abrolhos Islands, Western Australia. *Earth and Planetary Science Letters*, 118, 281–293.

Figure 1. Schematic overview of the various contributions to $\Delta\delta_c$; i.e., changes in foraminiferal carbonate $\delta^{18}\text{O}$ (after Rohling and Cooke, 1999). Blue shading denotes processes that change seawater $\delta^{18}\text{O}$ ($\Delta\delta_w$). Red shading denotes $\Delta\delta_{(T_w)}$, the component of δ_c change related to deep-sea temperature (T_w) changes due to temperature-dependent water-to-carbonate oxygen isotope fractionation. Green shading denotes secondary effects that can influence deep-sea benthic $\Delta\delta_c$. Processes in white boxes in the same row affect only planktonic foraminifera or shallow-water benthic foraminifera. Of the relevant (green) secondary effects, the $[\text{CO}_3^{2-}]$ and respiratory CO_2 influences (labeled “1”) can be reasonably limited by analyzing single species per record; i.e., aiming for a single habitat type with no large respiratory CO_2 or $[\text{CO}_3^{2-}]$ variations. Ontogenic (growth-stage) influences (labeled “2”) are commonly limited by analyzing specimens within narrow size ranges.

Figure 2. Schematic representation of hydrological-cycle influences on oxygen isotope ratios (after Rohling and Cooke, 1999). Effects on seawater are indicated in italics. $\delta^{18}\text{O}$ values for precipitation are approximate and for illustrative purposes only. The terms depletion and enrichment refer to ^{18}O abundance changes relative to ^{16}O that cause $\delta^{18}\text{O}$ decrease or increase, respectively.

Figure 3. Variations in mean seafloor spreading rates and seafloor production rates. A. Mean seafloor spreading rates, based on two alternative plate tectonic models (Matthews et al., 2016; and Young et al., 2019). **B.** Global seafloor production rates after Gernon et al. (2021). Main panels on the left are reconstructions for the past 40 million years, and smaller right-hand panels are 40–400 Ma extensions for context. Ages are listed in Ma because of the long-term context. Note that seafloor spreading and production rates since 40 Ma are minor relative to long-term trends. Therefore, ocean crustal production rates are unlikely to have exerted a major influence on sea level over the past 40 million years.

Figure 4. Diagram of the workflow used in the δ_c deconvolution method of Rohling et al. (2021). Equation numbers relate to the equations of Rohling et al. (2021). Equations 5–11 are used to calculate Antarctic Ice Sheet (AIS), Greenland Ice Sheet (GrIS), Laurentide Ice Sheet (LIS), and Eurasian Ice Sheet (EIS) ice-volume variations. Equation 1 is a parameterization of Rayleigh distillation that affects the $\delta^{18}\text{O}$ of precipitation over each ice sheet. Equations 12–14 were used to calculate net mass balance for each ice sheet and its temporal influence on mean ice-sheet $\delta^{18}\text{O}$. Equation 15 determined the impact of each ice sheet’s volume and mean ice-sheet $\delta^{18}\text{O}$ on mean ocean $\delta^{18}\text{O}$. Summing these gives the total global ice sheet impact on mean ocean $\delta^{18}\text{O}$. Finally, differencing between the measured changes in δ_c and δ_w , and dividing the result by $-0.25\text{‰}\text{ }^\circ\text{C}^{-1}$ (Kim and O’Neil, 1997) gives the change in deep-sea temperature.

Figure 5. Introduction of the main parameters through time discussed in this paper (based on Rohling et al., 2021). **A.** Colored arrows denote time-intervals captured in Figures 9 and 12 (dark blue); Figures 10 and 13 (light blue); Figures 11, 14, and 15 (orange); and Figures 16, 18, and S1 (red). **B.** Sea-level change relative to present. **C.** Deep-sea temperature change relative to present. In **B** and **C**, black denotes the median and magenta denotes its 99% probability interval from bootstrap analysis (see details in section 4). **D.** Relationship between deep-sea benthic foraminiferal carbonate $\delta^{18}\text{O}$ change ($\Delta\delta_c$) and sea-level change (Δz_{SL}) from the model underpinning **B** and **C**. **E.** Similar to **D**, but between $\Delta\delta_c$ and mean

seawater $\delta^{18}\text{O}$ change ($\Delta\delta_w$). **F.** Similar to **D**, but between $\Delta\delta_c$ and deep-sea temperature change (ΔT_w).

Figure 6. Regressions between δ_c and sea level with ranges used in sensitivity tests. **A.** The lagged quadratic regression (following [Spratt and Lisiecki, 2016](#)) between the [Lisiecki and Raymo \(2004\)](#) δ_c record and the [Spratt and Lisiecki \(2016\)](#) sea-level record, with alternate extrapolations beyond the data cloud, as used by [Rohling et al. \(2021\)](#). Bold red is the main-scenario regression, which in [Rohling et al. \(2021\)](#) was constrained to ~ 65 m for the ice-free state. Dashed red is the upper 95% bound of the main regression, which tops out at ~ 86 m. Purple is an unconstrained quadratic regression, which peaks at ~ 50 m (see [section 3.7](#)). **B.** Regression underpinning the additional uncertainty analyses presented here. Bold red is the same as in **A**, but now precisely constrained to 65.1 m for the ice-free state. Dashed orange and blue lines indicate functions that approximate the 68% and 95% prediction intervals for the main regression, albeit with an imposed constraint of 65.1 m for the ice-free state (see [section 4](#)).

Figure 7. Key conditions for the marginal-sea sea-level method. **A.** Bathymetric map of the Bab-el Mandab Strait including the shallowest passage at Hanish Sill. **B.** Bathymetric map of the Strait of Gibraltar including the shallowest passage at Camarinal Sill. ES is Espartel Sill, TB is Tarifa Basin, CS is Camarinal Sill (from [Naranjo, C., García-Lafuente, J., Sammartino, S., Sánchez-Garrido, J. C., Sánchez-Leal, R., & Jesús Bellanco, M. \(2017\). Recent changes \(2004–2016\) of temperature and salinity in the Mediterranean outflow. *Geophysical Research Letters*, 44, 5665–5672](#)). **C.** Cross section for Hanish Sill, Bab-el-Mandab Strait, after [Siddall et al. \(2002\)](#). **D.** Cross section for Camarinal Sill, Strait of Gibraltar, after [Bryden and Kinder \(1991\)](#). **E.** Simplified sketch of key factors considered in the marginal-sea method. Model calculations are of evolving seawater $\delta^{18}\text{O}$ and basin salinity; δ_{sw} and S_{sw} . E is evaporation, δ_E is the vapor $\delta^{18}\text{O}$ (a function of δ_{sw} that is calculated with complete fractionation equations, and roughly equal to $\delta_{sw} - 10$ ‰), S_E is vapor salinity ($= 0$), and $P+R$ is precipitation + runoff, with $\delta^{18}\text{O}$ values (δ_{P+R}) that range typically between -12 and 0 ‰ and salinity $S_{P+R} = 0$. Q_{in} is surface inflow flux of open-ocean water with properties δ_{in} (inflow seawater $\delta^{18}\text{O}$) and S_{in} (salinity), Q_{out} is subsurface outflow flux back into the open ocean with properties δ_{sw} (inflow seawater $\delta^{18}\text{O}$) and S_{sw} (salinity). Temperature conditions (not indicated) are also considered in the models. For complete descriptions see ([Rohling et al., 1998, 2004, 2009, 2014](#); [Rohling, 1999](#); [Siddall et al., 2002, 2003, 2004](#); [Grant et al., 2012, 2014](#)).

Figure 8. Hysteresis behavior in mean ice-sheet $\delta^{18}\text{O}$ relative to ice volume (based on [Rohling et al., 2021](#)). **A.** Results from our process-modeling analysis of the [Westerhold et al. \(2020\)](#) δ_c record (after correcting minor errors in the original script in closing the ice-volume budget with respect to sea-level change; see [section 4](#) and R scripts available). Black is Antarctic Ice Sheet (AIS; here taken to imply the entire West+East Antarctic ice-sheet complex), red is Laurentide Ice Sheet (LIS; here taken to imply the entire North American ice-sheet complex), blue is Eurasian Ice Sheet (EIS), and green is Greenland Ice Sheet (GrIS). **B.** Schematic illustration of the nature of the relationships in **A**. Number 1 represents the trajectory associated with gradual ice-volume build up, determined by continuous instantaneous ice-volume-based adjustment of the $\delta^{18}\text{O}$ of new precipitation (accumulation), and lagged adjustment of mean ice-sheet $\delta^{18}\text{O}$ according to the model residence-time calculation. Number 2 represents rapid ice loss during deglaciation, which

occurs at the mean ice-sheet $\delta^{18}\text{O}$ attained just before deglaciation onset; and 3 represents adjustment at the end of deglaciation, when new ice starts to build up at the initial $\delta^{18}\text{O}$ value of new precipitation (accumulation). Number 4 marks the trajectory associated with gradual partial glaciation (as 1); 5 is rapid partial deglaciation (as 2); and 6 represents more gradual mean ice-sheet $\delta^{18}\text{O}$ adjustment to conditions commensurate with the remaining ice volume after partial deglaciation.

Figure 9. Comparison of records on their original chronologies over the last 550,000 years.

Coral data (references given below), and both the Mediterranean (Rohling et al., 2014, 2017) and Red Sea (Grant et al., 2014) reconstructions are presented as RSL, and are used for chronological guidance of major transitions rather than for absolute sea-level information, as explained in sections 2 and 5.1. **A.** Sea level relative to present. Red is our process model-based median using the Lisiecki and Raymo (2005) δ_c record, and black for the Westerhold et al. (2020) δ_c record, both with (orange and gray) 99% probability envelopes for the median from bootstrap analysis (section 4). Blue is the reconstruction of Bates et al. (2014), yellow-green is the Miller et al. (2020) record, dashed black is Red Sea RSL (Grant et al., 2012, 2014), and green is Mediterranean Sea RSL based on core LC21 (Rohling et al., 2014, 2017). Individual symbols indicate coral-based RSL data, from the compilation of Hibbert et al. (2016), clipped to the range between -140 and +30 m to minimize clutter. Gray symbols represent all coral data for which age and Z_{cp} (see section 5.1) are reported, while magenta dots indicate the subset of that compilation that passes commonly applied age-reliability screening criteria ($\delta^{234}\text{U}_{\text{initial}}$, calcite $\leq 2\%$, and $[^{232}\text{Th}] \leq 2$ ppb; and $\delta^{234}\text{U}_{\text{initial}} = 147 \pm 5 \text{‰}$ when $0 < \text{age} \leq 17 \text{ ka}$, $142 \pm 8 \text{‰}$ when $17 < \text{age} \leq 71 \text{ ka}$, $147 \pm 5 \text{‰}$ when $71 < \text{age} \leq 130 \text{ ka}$, and $147 \pm 5/-10 \text{‰}$ when $\text{age} > 130 \text{ ka}$). **B.** Deep-sea temperature relative to the present. Red and black are as in **A**. Red dot with error bars in the Last Glacial Maximum represents a global ocean cooling estimate from ice-core noble gas data (Bereiter et al., 2018). Blue is the reconstruction of Bates et al. (2014). Note that the Bates et al. (2014) reconstruction represents one specific location and is plotted against a secondary Y-axis (blue), with the same scale increments that is offset in absolute values relative to the primary Y-axis. Source data for corals before screening (gray symbols): Australia (Veeh and Veevers, 1970; Eisenhauer et al., 1993, 1996; Zhu et al., 1993; Stirling et al., 1995, 1998, 2001; Stirling, 1996; Collins et al., 2006; Hearty et al., 2007; McCulloch and Mortimer, 2008; O'Leary et al., 2008a, 2008b, 2013; Andersen et al., 2010; Lewis et al., 2012; Leonard et al., 2016; Yokoyama et al., 2018); Bahamas (Chen et al., 1991; Hearty et al., 2007; Thompson et al., 2011); Barbados (Edwards et al., 1987, 1997; Bard et al., 1990a, 1990b, 1991; Hamelin et al., 1991; Gallup et al., 1994, 2002; Blanchon and Eisenhauer, 2000; Cutler et al., 2003; Thompson et al., 2003; Potter et al., 2004; Speed and Cheng, 2004; Chiu et al., 2005; Fairbanks et al., 2005; Mortlock et al., 2005; Thompson and Goldstein, 2005; Peltier and Fairbanks, 2006; Andersen et al., 2010; Abdul et al., 2016); Bermuda (Ludwig et al., 1996; Hearty et al., 1999; Muhs et al., 2002b); Cape Verde (Zazo et al., 2007); China (Zhao and Yu, 2002; Sun et al., 2005); Mayotte, Comoro Archipelago (Colonna et al., 1996; Camoin et al., 1997); Curacao (Hamelin et al., 1991; Muhs et al., 2012a); Eritrea, Red Sea (Walter et al., 2000); Tahiti, French Polynesia (Bard et al., 1996a, 2010; Thomas et al., 2009, 2012; Deschamps et al., 2012); Mururoa Atoll, French Polynesia (Bard et al., 1991; Camoin et al., 2001); Marquesas Islands, French Polynesia (Cabioch et al., 2008); Grand Cayman (Vezina et al., 1999; Blanchon et al., 2002; Coyne et al., 2007); Greece (Dia et al., 1997); Haiti (Bard et al., 1990b); Sumba Island, Indonesia (Bard et al., 1996b); Madagascar (Camoin et

al., 2004); Mauritius (Camoin et al., 1997); Baja California, Mexico (Muhs et al., 2002a); Yucatan, Mexico (Blanchon et al., 2009); New Caledonia (Frank et al., 2006); Niue (Kennedy et al., 2012); Huon Peninsula, Papua New Guinea (Dia et al., 1992; Edwards et al., 1993; Stein et al., 1993; Chappell et al., 1996; Esat et al., 1999; Yokoyama et al., 2001a; Cutler et al., 2002, 2003); Huon Gulf, Papua New Guinea (Galewsky et al., 1996); New Britain Island, Papua New Guinea (Riker-Coleman et al., 2006); Pitcairn, Henderson Island (Stirling et al., 2001; Ayling et al., 2006; Andersen et al., 2008, 2010); Réunion (Camoin et al., 1997); Seychelles (Israelson and Wohlfarth, 1999; Camoin et al., 2004; Dutton et al., 2015); US Virgin Islands, St Croix (Toscano et al., 2012); California, USA (Muhs et al., 2002a; 2006; 2012b); Florida, USA (Ludwig et al., 1996; Toscano and Lundberg, 1998; Fruijtier et al., 2000; Muhs et al., 2002a, 2011; Multer et al., 2002); Hawaii, USA (Sherman et al., 1999; Hearty, 2002; Muhs et al., 2002b; Hearty et al., 2007; McMurtry et al., 2010); Oregon, USA (Muhs et al., 2006); Vanuatu (Cabioch et al., 2003; Cutler et al., 2004). Source data for corals after screening (magenta dots): Australia (Eisenhauer et al., 1993, 1996; Zhu et al., 1993; Stirling et al., 1995, 1998, 2001; Collins et al., 2006; O'Leary et al., 2008a); Bahamas (Chen et al., 1991); Barbados (Hamelin et al., 1991; Gallup et al., 1994, 2002; Blanchon and Eisenhauer, 2000; Cutler et al., 2003; Thompson et al., 2003; Potter et al., 2004; Chiu et al., 2005; Fairbanks et al., 2005; Mortlock et al., 2005; Peltier and Fairbanks, 2006; Andersen et al., 2010; Abdul et al., 2016); Bermuda (Muhs et al., 2002b), China (Sun et al., 2005); Curacao (Muhs et al., 2012a); Tahiti, French Polynesia (Thomas et al., 2009; Deschamps et al., 2012); Mururoa Atoll, French Polynesia (Camoin et al., 2001); Marquesas Islands, French Polynesia (Cabioch et al., 2008); Grand Cayman (Blanchon et al., 2002); Yucatan, Mexico (Blanchon et al., 2009); New Caledonia (Frank et al., 2006); Huon Peninsula, Papua New Guinea (Dia et al., 1992; Stein et al., 1993; Yokoyama et al., 2001; Cutler et al., 2002, 2003); Huon Gulf, Papua New Guinea (Galewsky et al., 1996); Pitcairn, Henderson Island (Stirling et al., 2001; Ayling et al., 2006; Andersen et al., 2008, 2010); Seychelles (Israelson and Wohlfarth, 1999; Camoin et al., 2004; Dutton et al., 2015); US Virgin Islands, St Croix (Toscano et al., 2012); Hawaii, USA (Sherman et al., 1999; Hearty, 2002; Muhs et al., 2002b; Hearty et al., 2007; McMurtry et al., 2010); Vanuatu (Cabioch et al., 2003; Cutler et al., 2004).

Figure 10. Comparison of records on their original chronologies over the last 800,000 years. Relative to Figure 9, extension to 800 ka provides details of lower-amplitude glacial cycles before ~450 ka. **A.** Sea level relative to present. Red is our process model-based median using the Lisiecki and Raymo (2005) δ_c record, and black for the Westerhold et al. (2020) δ_c record, with (orange and gray) 99% probability envelopes for the median from bootstrap analysis (section 4). Yellow-green is the Miller et al. (2020) record, dashed black is Red Sea RSL (Grant et al., 2012, 2014). Blue is the reconstruction of Spratt and Lisiecki (2016), and green that of de Boer et al. (2010). **B.** Deep-sea temperature relative to present. Red and black are as in A. Red dot with error bars in the Last Glacial Maximum represents a global ocean cooling estimate from ice-core noble gas data (Bereiter et al., 2018). Cyan is Antarctic temperature relative to present (Jouzel et al., 2007), with a separate Y axis (scaled in 4:1 proportion relative to the main Y axis).

Figure 11. Comparison of records on their original chronologies over the last 5.3 million years. **A.** Sea level relative to present. Red/orange is our process model-based median using the Lisiecki and Raymo (2005) δ_c record, and black for the Westerhold et al. (2020) δ_c record, each with (orange and gray) 99% probability envelope for the median from

bootstrap analysis (section 4). Yellow-green is the Miller et al. (2020) record, dark blue is the Bates et al. (2014) reconstruction, light blue is the low-high range of Berends et al. (2021a). Green circles with error bars are GMSL benchmarks from Mallorca (GIA, dynamic topography, and tectonics corrected RSL), with 2σ age uncertainties and sea-level ranges between the 16th and 84th percentiles (Dumitru et al., 2019, 2021). Black box: GMSL mean and 1σ range from similarly treated coastal sediment benchmarks in Patagonia (Rovere et al., 2020). Magenta indicates RSL variability (with range) reconstructed from a combination of New Zealand sequence stratigraphy and δ_c (Naish et al., 2009; Miller et al., 2012). Lilac boxes represent the amplitude range of glacial-interglacial variations off New Zealand (Grant et al., 2019), vertically adjusted to the GMSL position in the process model solution. Green record between 2.4 and 2.75 Ma is the reconstruction of Jakob et al. (2020). **B.** Deep-sea temperature relative to present. Red/orange, black/gray, blue and green are as in **A.** Red dot with error bars in the Last Glacial Maximum represents a global ocean cooling estimate from ice-core noble gas data (Bereiter et al., 2018). Note the site-specific secondary (blue) Y-axis for the Bates et al. (2014) record, and the tertiary Y-axis (green) for the Jakob et al. (2020) record, which have the same scale increments with offset absolute values relative to the primary Y-axis. **C.** Comparison between the median sea-level reconstruction from our process model using the Lisiecki and Raymo (2005) δ_c record (black) and the central estimate from the inverse model of Berends et al. (2021a) using the same input record (red). **D.** Histogram of differences between the two records shown in **C.**

Figure 12. Comparison of records over the last 550,000 years after chronological fine-tuning. Similar to Figures 9a, 9b but after fine-tuning of the Lisiecki and Raymo (2004) based (red and orange) and Westerhold et al. (2020) based (black and gray) records detailed in section 5.2. **A.** Sea level relative to present. Red is our process model-based median using the Lisiecki and Raymo (2005) δ_c record, and black for the Westerhold et al. (2020) δ_c record, both with (orange and gray) 99% probability envelopes for the median from bootstrap analysis (section 4). Blue is the reconstruction of Bates et al. (2014), yellow-green is the Miller et al. (2020) record, dashed black is Red Sea RSL (Grant et al., 2012, 2014), and green is Mediterranean Sea RSL based on core LC21 (Rohling et al., 2014, 2017). Individual symbols indicate coral-based RSL data, from the compilation of Hibbert et al. (2016), clipped to the range between -140 and +30 m to minimize clutter. Gray symbols represent all coral data for which age and Z_{cp} (see section 5.1) have been reported, while magenta dots indicate the subset of that compilation that passes commonly applied age-reliability screening criteria ($\delta^{234}\text{U}_{\text{initial, calcite}} \leq 2\%$, and $[^{232}\text{Th}] \leq 2$ ppb; and $\delta^{234}\text{U}_{\text{initial}} = 147 \pm 5 \text{‰}$ when $0 < \text{age} \leq 17$ ka, $142 \pm 8 \text{‰}$ when $17 < \text{age} \leq 71$ ka, $147 \pm 5 \text{‰}$ when $71 < \text{age} \leq 130$ ka, and $147 \pm 5/-10 \text{‰}$ when $\text{age} > 130$ ka). For coral source-data references, see Figure 9 caption. **B.** Deep-sea temperature relative to present. Red and black are as in **A.** Red dot with error bars in the Last Glacial Maximum represents a global ocean cooling estimate from ice-core noble gas data (Bereiter et al., 2018). Blue is the reconstruction of Bates et al. (2014). Note that the Bates et al. (2014) reconstruction represents one specific location and is plotted against a secondary Y-axis (blue), which has the same scale increments with offset absolute values relative to the primary Y-axis. Between **A** and **B**, red diamonds indicate tuning tie-points for the Lisiecki and Raymo (2004) based record, and black diamonds for the Westerhold et al. (2020) based record, as summarized in Table 1.

Figure 13. Comparison of records over the last 800,000 years after chronological fine-tuning. Similar to Figures 10a, 10b after fine-tuning of the Lisiecki and Raymo (2004) based (red and orange) and Westerhold et al. (2020) based (black and gray) records as detailed in section 5.2. The extension to 800 ka provides details of lower-amplitude glacial cycles before ~450 ka. **A.** Sea level relative to present. Red is our process model-based median using the Lisiecki and Raymo (2005) δ_c record, and black for the Westerhold et al. (2020) δ_c record, with (orange and gray) 99% probability envelopes for the median from bootstrap analysis (section 4). Yellow-green is the Miller et al. (2020) record, dashed black is Red Sea RSL (Grant et al., 2012, 2014). Blue is the reconstruction of Spratt and Lisiecki (2016), and green that of de Boer et al. (2010). **B.** Deep-sea temperature relative to present. Red and black are as in A. Red dot with error bars in the Last Glacial Maximum represents a global ocean cooling estimate from ice-core noble gas data (Bereiter et al., 2018). Cyan is Antarctic temperature relative to present (Jouzel et al., 2007), shown against a separate Y axis (scaled in 4:1 proportion relative to the main Y axis). Between A and B, red diamonds indicate tuning tie-points for the Lisiecki and Raymo (2004) based record, and black diamonds for the Westerhold et al. (2020) based record, as summarized in Table 1.

Figure 14. Comparison of records over the last 5.3 million years after chronological fine-tuning. Similar to Figures 11a, 11b after fine-tuning of the Lisiecki and Raymo (2004) based (red and orange) and Westerhold et al. (2020) based (black and gray) records as detailed in section 5.2. **A.** Sea level relative to present. Red/orange is our process model-based median using the Lisiecki and Raymo (2005) δ_c record, and black for the Westerhold et al. (2020) δ_c record, each with (orange and gray) 99% probability envelope for the median from bootstrap analysis (section 4). Yellow-green is the Miller et al. (2020) record, dark blue is the Bates et al. (2014) reconstruction, light blue is the low-high range of Berends et al. (2021a), and green is the reconstruction of de Boer et al. (2010). Green circles with error bars are GMSL benchmarks (GIA, dynamic topography, and tectonics corrected RSL) from Mallorca, with 2σ age uncertainties and sea-level ranges between the 16th and 84th percentiles (Dumitru et al., 2019, 2021). Black box: GMSL mean and 1σ range from similarly treated coastal sediment benchmarks in Patagonia (Rovere et al., 2020). Magenta denotes RSL variability (with range) reconstructed from a combination of New Zealand sequence stratigraphy and δ_c (Naish et al., 2009; Miller et al., 2012). Lilac boxes represent the amplitude range of glacial-interglacial variations off New Zealand (Grant et al., 2019), vertically adjusted to the GMSL position in the process model solution. The green record between 2.4 and 2.75 Ma is the reconstruction of Jakob et al. (2020). **B.** Deep-sea temperature relative to present. Red/orange, black/gray, blue and green are as in A. Red dot with error bars in the Last Glacial Maximum represents a global ocean cooling estimate from ice-core noble gas data (Bereiter et al., 2018). Note the site-specific secondary (blue) Y-axis for the Bates et al. (2014) record, and the tertiary Y-axis (green) for the Jakob et al. (2020) record, which have the same scale increments with offset absolute values relative to the primary Y-axis. Between A and B, red diamonds indicate tuning tie-points for the Lisiecki and Raymo (2004) based record, and black diamonds for the Westerhold et al. (2020) based record, as summarized in Table 1.

Figure 15. Plio-Pleistocene synthesis records. **A.** Sea level relative to present. Orange is our synthesis (median with 99% probability interval from bootstrap analysis) of the joint process model assessment of the Lisiecki and Raymo (2004) based and Westerhold et al. (2020)

based records after chronological assessment ([section 5.2](#)). Green circles with error bars are GMSL benchmarks (GIA, dynamic topography, and tectonics corrected RSL) from Mallorca, with 2σ age uncertainties and sea-level ranges between the 16th and 84th percentiles ([Dumitru et al., 2019, 2021](#)). Black box: GMSL mean and 1σ range from similarly treated coastal sediment benchmarks in Patagonia ([Rovere et al., 2020](#)). Cyan is the low-high range of [Berends et al. \(2021a\)](#). Dashed green is the reconstruction of [Hansen et al. \(2013\)](#). The stepped navy-blue dotted line schematically highlights key transitions toward the maximum glacial conditions of the last 650 kyr ([section 6.4](#)). **B.** Deep-sea temperature relative to present. Orange, dashed green, and stepped navy-blue dotted lines are as in **A**. Light blue is Antarctic temperature relative to present ([Jouzel et al., 2007](#)), versus a separate Y axis (scaled in 4:1 proportion relative to the main Y axis). Magenta dot with error bars in the Last Glacial Maximum represents a global ocean cooling estimate from ice-core noble gas data ([Bereiter et al., 2018](#)). **C.** Deep-sea seawater $\delta^{18}\text{O}$ relative to present. Orange is as in **A**. Light blue dots (with 11-pt moving average line) are the $\Delta\delta_w$ reconstruction of [Elderfield et al. \(2012\)](#) for ODP Site 1123 (SW Pacific). Dark blue line is a three-record $\Delta\delta_w$ stack, including ODP Site 1123, with $1\times$ bootstrap error envelopes ([Ford and Raymo, 2019](#)).

Figure 16. Comparison of records over the last 40 million years, with sensitivity tests. In all panels, gray is the median for our process model main scenario using the [Westerhold et al. \(2020\)](#) δ_c record, while light blue is sensitivity test *i* with modified $\Delta\delta_c:\Delta z_{SL}$ regression but unchanged “cold ice-sheet” Rayleigh fractionation for $\delta^{18}\text{O}$ of precipitation over the AIS, and pink is sensitivity test *ii* with both modified $\Delta\delta_c:\Delta z_{SL}$ and “warm (LIS-like) ice-sheet” Rayleigh fractionation for $\delta^{18}\text{O}$ of precipitation over AIS. For sea level (panels **A** and **D**), therefore, the pink and light blue solutions are identical. **A.** Sea level relative to present. Magenta is the [de Boer et al. \(2010\)](#) record and yellow-green is the [Miller et al. \(2020\)](#) record. Cyan follows the two-segment linear approach of [Hansen et al. \(2013\)](#), which is applied here to the [Westerhold et al. \(2020\)](#) δ_c record rather than the [Zachos et al. \(2008\)](#) δ_c record that was originally used (see segment control points in **D**). Red dots with error bars represent the [Kominz et al. \(2016\)](#) reconstruction (with “high–low” range). Purple circles are central values of GMSL benchmarks (GIA, dynamic topography, and tectonics corrected RSL) from Mallorca ([Dumitru et al., 2019, 2021](#)). Black box: GMSL mean and 1σ range from similarly treated coastal sediment benchmarks in Patagonia ([Rovere et al., 2020](#)). **B.** Deep-sea temperature relative to present. Gray, light blue, pink, and cyan are as in **A**. Yellow-green is calculated here from $\Delta\delta_w$ and $\Delta\delta_c$ used and reported by [Miller et al. \(2020\)](#), after first expressing both input records to variations relative to present. Using the main Y-axis (black), red dots and 7-point moving average are Mg/Ca-based estimates of [Lear et al. \(2004\)](#) relative to present (i.e., 1.6°C at 4.8 km depth in the equatorial Pacific). Using the secondary Y-axis (dark blue), which has the same scale increments with offset absolute values, dark blue dots with thin blue trend line are Mg/Ca-based estimates of [Modestu et al. \(2020\)](#), while the heavy dark blue line is the gradient in the Δ_{47} data of [Modestu et al. \(2020\)](#). **C.** Deep-sea $\delta^{18}\text{O}$ relative to present, which combines information on $\delta^{18}\text{O}$ of carbonate and seawater. For carbonate, red is the [Westerhold et al. \(2020\)](#) δ_c record, light green is the δ_c record used by [Miller et al. \(2020\)](#), and purple dots with 7-point moving average are [Lear et al. \(2004\)](#) δ_c data; all versus the main Y-axis (black). The dark blue dots represent the δ_c data of [Modestu et al. \(2020\)](#) versus the secondary Y-axis (dark blue), which has the same scale increments offset for absolute values. For seawater values, gray, light blue, and pink are δ_w records for our process model using the main scenario and sensitivity scenarios *i* and *ii*, respectively, while

yellow-green is the [Miller et al. \(2020\)](#) δ_w record, and brown dots with 7-point moving average are [Lear et al. \(2004\)](#) δ_w data; all versus the main Y-axis (black). Note that the [Lear et al. \(2004\)](#) data have been clipped to the EOT because earlier data are affected by dissolution. Dark green dots represent the [Modestu et al. \(2020\)](#) δ_w data from Mg/Ca-temperature-based $\Delta\delta_{(Tw)}$ correction of their δ_c data on the secondary Y-axis (dark blue). Black dots are the dark green data adjusted here for (1) the extra temperature slope in Δ_{47} -based temperature data relative to the Mg/Ca-based temperature data of [Modestu et al. \(2020\)](#) (B), and (2) an empirical mean-shift of $\sim 5.5^\circ\text{C}$ ([sections 5.3](#) and [6.1](#)). D. Comparison of $\Delta\delta_c:\Delta z_{SL}$ relationships used in our process model main scenario (gray), sensitivity scenarios *i* and *ii* (blue and pink), and the assumed [Hansen et al. \(2013\)](#) two-segment relationship as applied here to the [Westerhold et al. \(2020\)](#) δ_c record (cyan). E. Relationships between $\Delta\delta_c$ and $\Delta\delta_w$ implied by our process model for the three scenarios investigated.

Figure 17. Theoretical evaluation of the $\Delta\delta_c:\Delta z_{SL}$ relationship. A. Contributions (to $\Delta\delta_c$) of $\Delta\delta_w$ and $\Delta\delta_{(Tw)}$ in relation to sea level, relative to present. The $\Delta\delta_w$ contributions are mean seawater δ_w variations from our process model (cf. [Rohling et al., 2021](#)) using the main scenario “cold ice-sheet” Rayleigh fractionation for $\delta^{18}\text{O}$ of precipitation over AIS (blue) and the sensitivity-test “warm (LIS-like) ice-sheet” Rayleigh fractionation for $\delta^{18}\text{O}$ of precipitation over AIS (pink). Black is the theoretical $\Delta\delta_{(Tw)}$ contribution through three temperature control conditions (yellow stars), as discussed in [section 5.3](#). B. Pink and blue are the Δz_{SL} versus $\Delta\delta_c$ relationships that result from combining the pink and blue $\Delta\delta_w$ contributions with the theoretical $\Delta\delta_{(Tw)}$ contribution from A, respectively. For comparison, gray is the $\Delta\delta_c:\Delta z_{SL}$ regression used in the process model ([Figures 4d, 5](#)) (after [Rohling et al., 2021](#)). This reveals that the overall convex $\Delta\delta_c:\Delta z_{SL}$ relationship shape is robust within the uncertainties considered; i.e., deviations fall well within the main scenario prediction intervals ([Figure 5b](#)) and the range of alternative regressions considered ([Figure 5a](#)). C. Comparison between theoretical ΔT_w estimates (black; as used in A), and actual ΔT_w calculated with the process model (blue and pink as in A). For discussion see [section 5.3](#).

Figure 18. Synthesis of records through the last 40 million years.

A. Sea level relative to present. Dark orange is our Plio-Pleistocene synthesis record ([Figure 15a](#)). Gray is the median for our process model main scenario using the [Westerhold et al. \(2020\)](#) δ_c record, and blue is sensitivity test *i* with modified $\Delta\delta_c:\Delta z_{SL}$ regression but unchanged “cold ice-sheet” Rayleigh fractionation for $\delta^{18}\text{O}$ of precipitation over AIS (both as in [Figure 16a](#)). As discussed in [section 6.1](#), sensitivity test *ii* was discarded. We infer that total uncertainty before 5.3 Ma is given by the blue hatching between the gray and blue lines. Note: this blue-hatched uncertainty zone does not represent random uncertainties, but the potential range of structured, long-term variability; see [Supplementary Figure S1a](#). B. Deep-sea temperature relative to present. Colors and shading are as in A. C. Deep-sea $\delta^{18}\text{O}$ relative to present, which combines information on $\delta^{18}\text{O}$ of carbonate and of seawater. Green is the [Westerhold et al. \(2020\)](#) δ_c record. Dark orange, gray, blue, and blue shading (between the gray and blue lines) are as in A. D. Comparison of $\Delta\delta_c:\Delta z_{SL}$ relationships used in our process model main scenario (gray) and sensitivity scenario *i* (blue). E. Relationships between $\Delta\delta_c$ and $\Delta\delta_w$ implied by the process model main scenario (gray) and sensitivity scenario *i* (blue). F. Relationships between deep-sea temperature change (ΔT_w) and $\Delta\delta_w$ implied by process model main scenario (gray) and sensitivity scenario *i* (blue).

Supplementary Figure S1. Rate of change comparison between RSL and GMSL reconstructions at Hanish Sill, Bab-el-Mandab strait, southern Red Sea. After [Grant et al. \(2012\)](#). **A.** Comparison between rates of change in reconstructions of (red) RSL and (blue) GIA-corrected Global Mean Sea Level (GMSL) over the last 150,000 years. **B.** Linear regressions for this comparison using GMSL from GIA corrections based on two different Earth models (black crosses with red line, versus gray crosses with cyan line).

Supplementary Figure S2. As Figure 15, but using an alternative chronological fine-tuning. Here the tie points listed in [Table 1](#) are used to fine-tune the [Lisiecki and Raymo \(2004\)](#) chronology in the interval >792 ka to that of [Westerhold et al. \(2020\)](#), instead of the other way around (as was done in [Figure 15](#)).

Supplementary Figure S3. Illustration of the role of long-term inertia on the potential “pathway” through the uncertainty envelope ([section 6.5](#)). **A.** As [Figure 18a](#) with only the blue shaded uncertainty interval between the process model main scenario (upper limit) and sensitivity scenario *i* (lower limit) in the 5.3-40 Ma interval. Magenta dashed line is a smoothing spline (9 degrees of freedom) through the main scenario record; we use the signs of its time derivatives to determine which sea-level increment to use per time step (see details in [section 6.5](#)). Black is the resultant sea-level “pathway” through time, which accounts for multi-million-year inertia that causes systematic sampling through the uncertainty envelope. **B.** Illustrative comparison of $\Delta\delta_c:\Delta z_{SL}$ relationships used in our process model main scenario (upper blue) and sensitivity scenario *i* (lower blue), and the complication in this relationship that arises from considering multi-million-year inertia that causes systematic sampling through the uncertainty envelope, as illustrated in **A**.

Figure 1

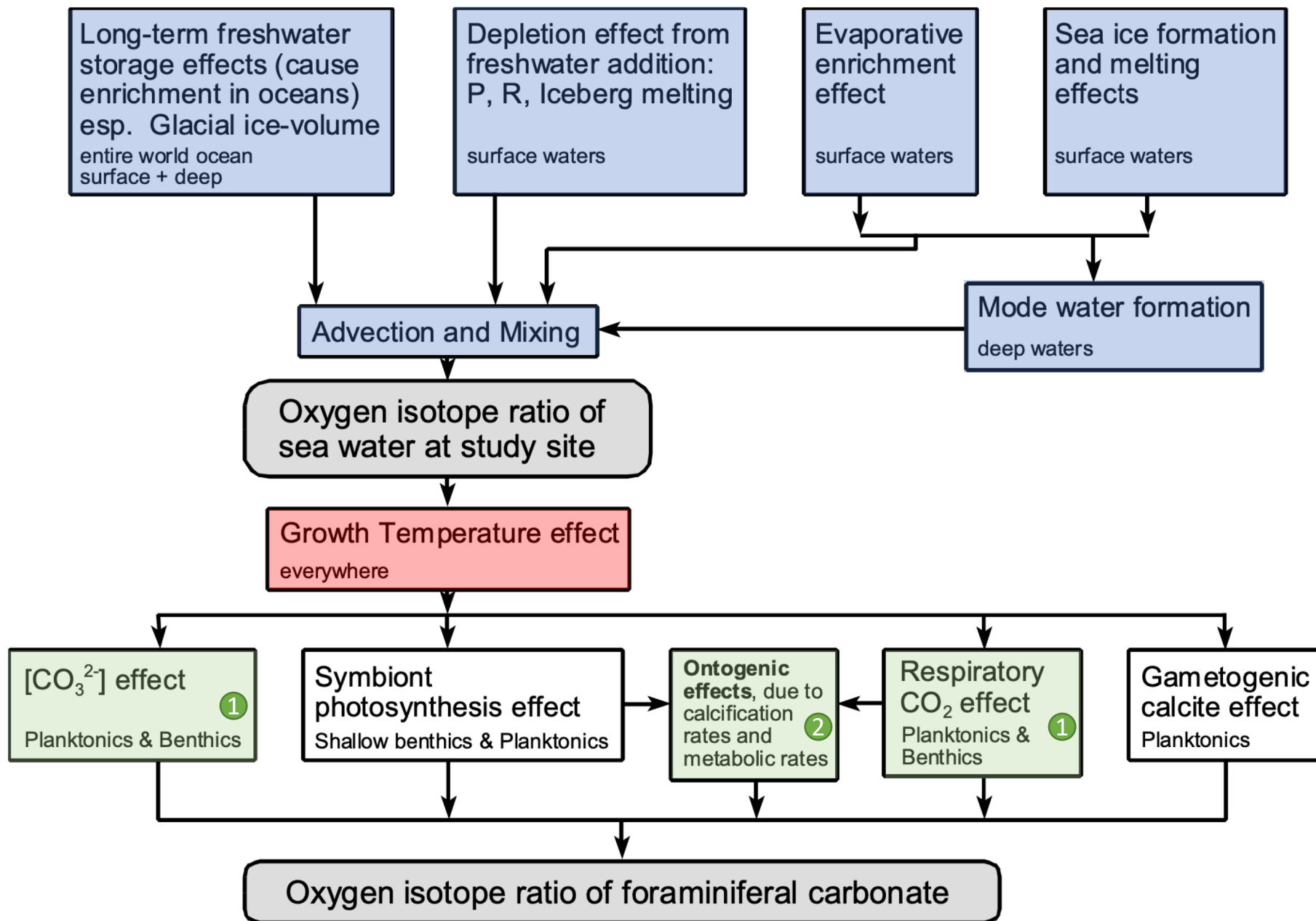


Figure 2

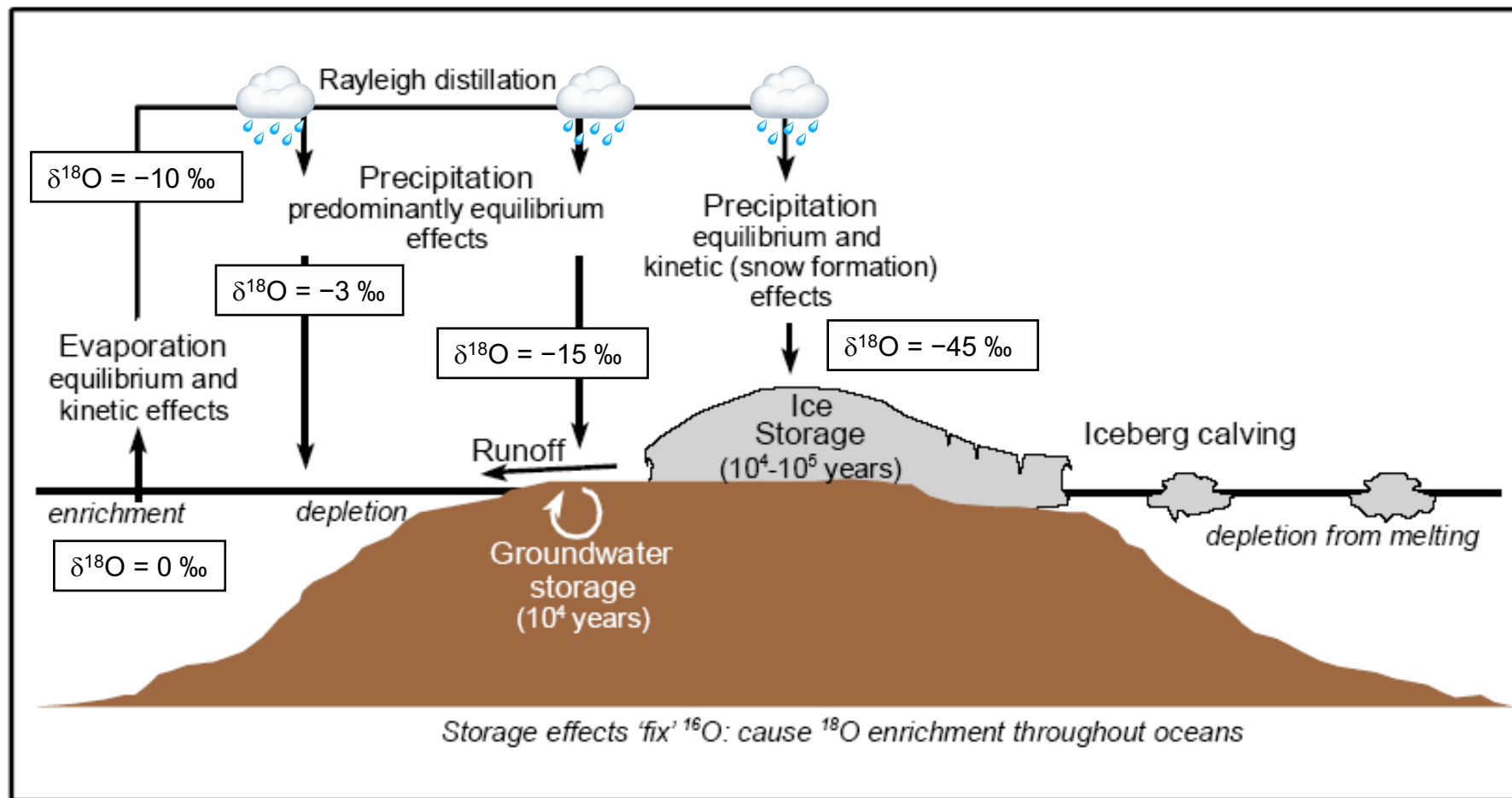


Figure 2

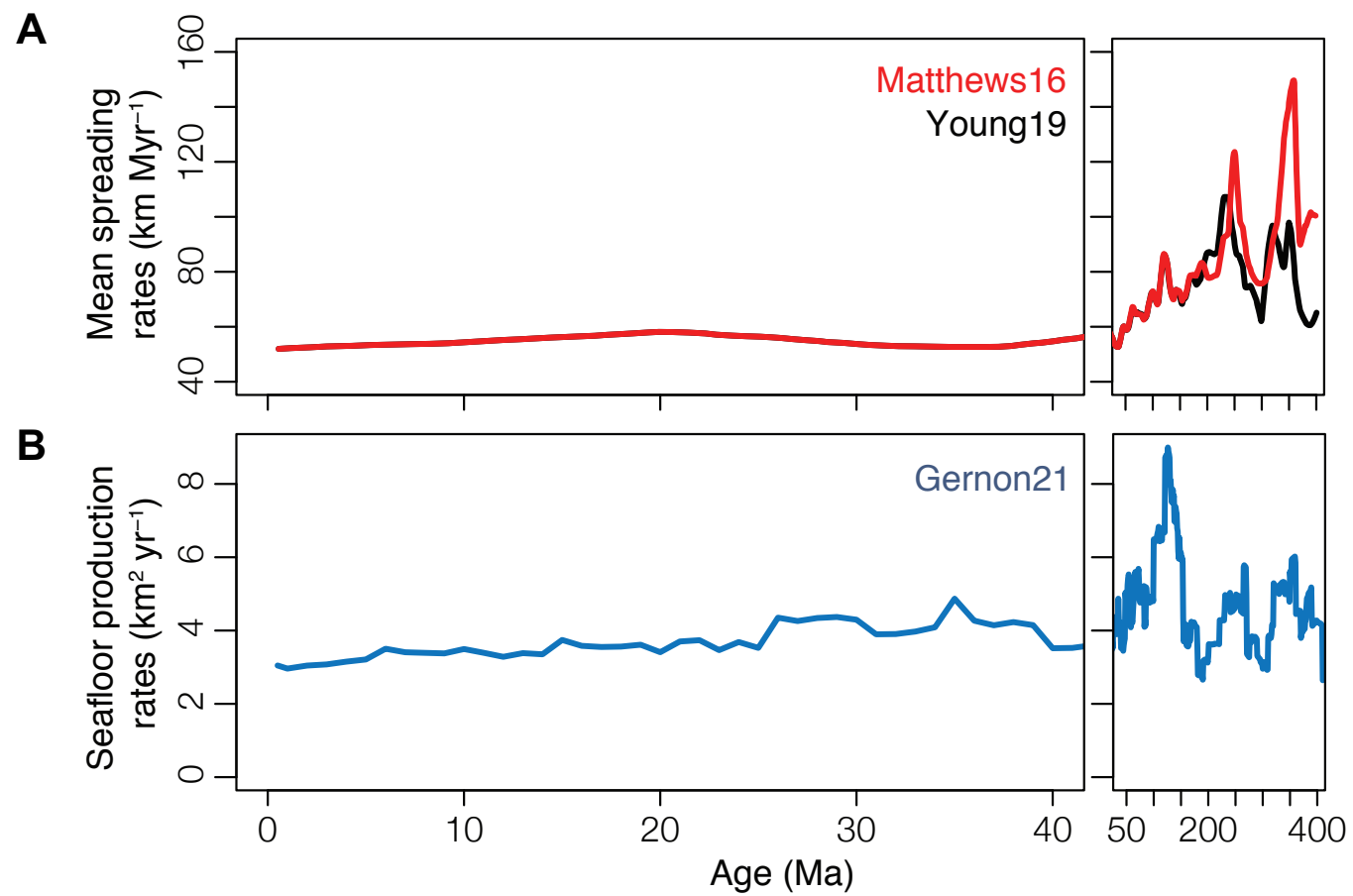


Figure 4

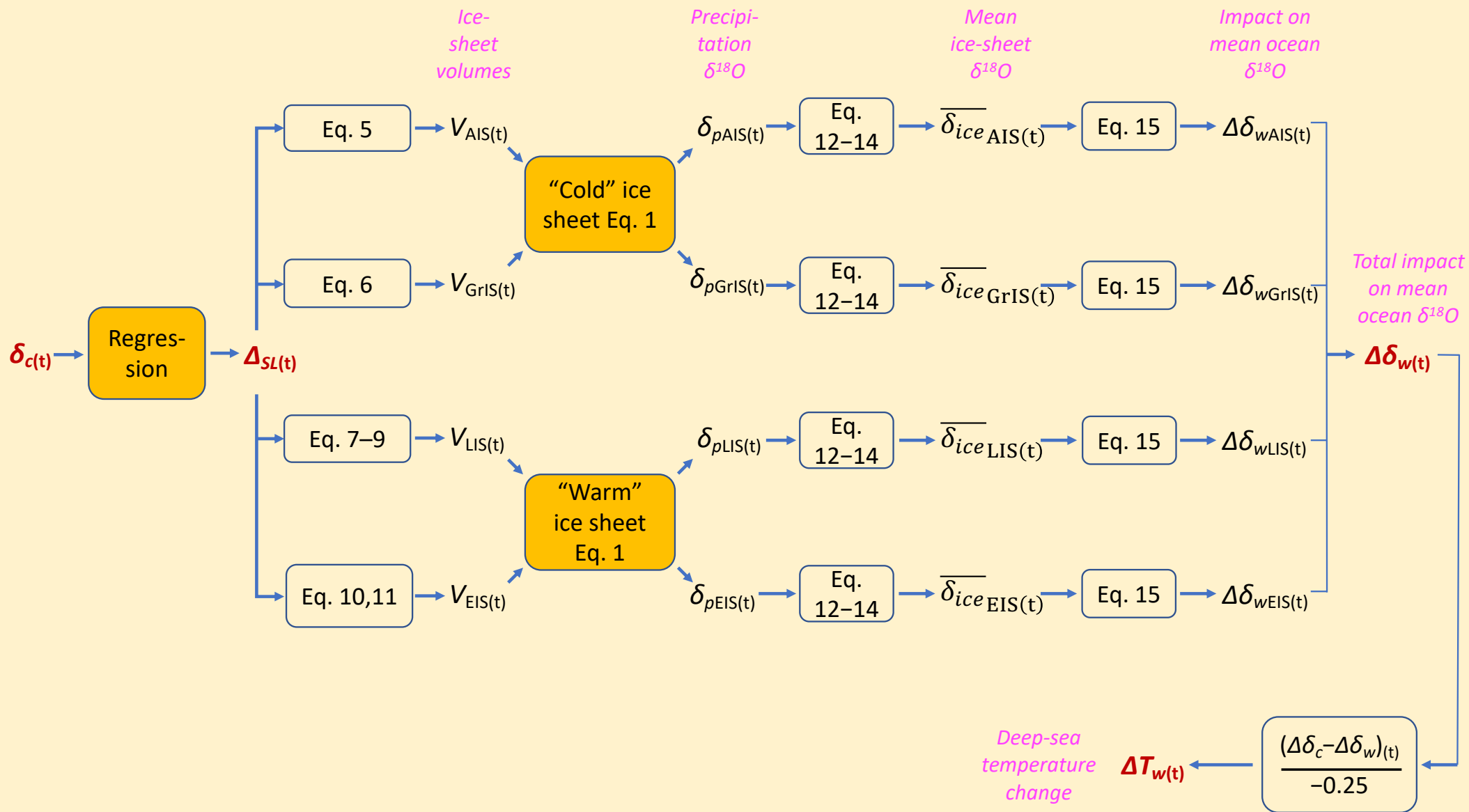


Figure 5

Last 40 Myr overview

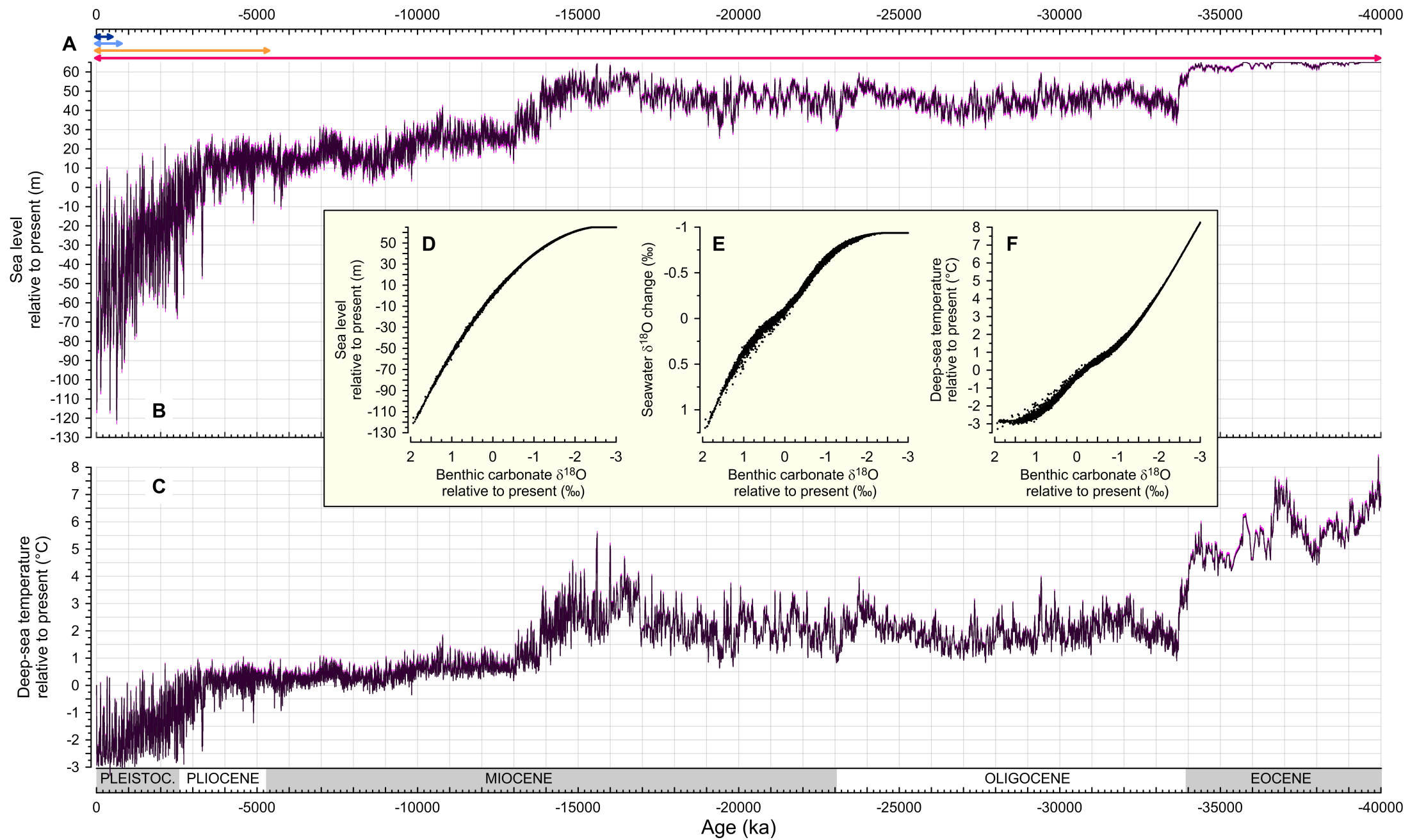


Figure 6

Sea-level regression uncertainties

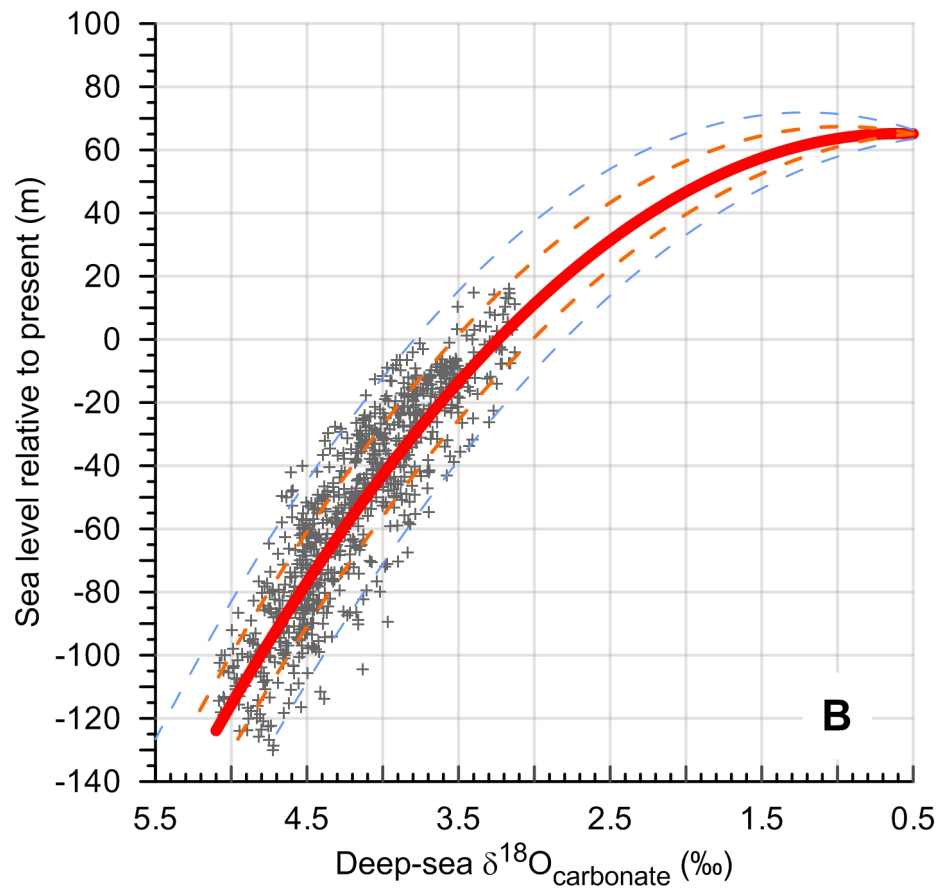
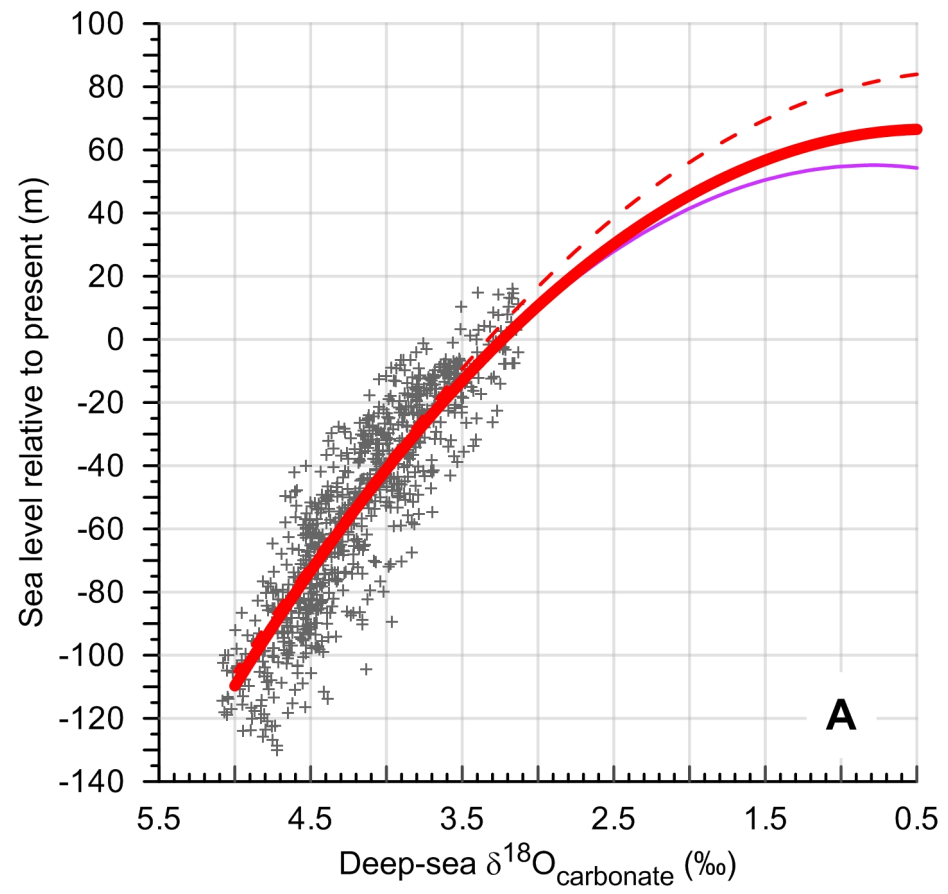


Figure 7

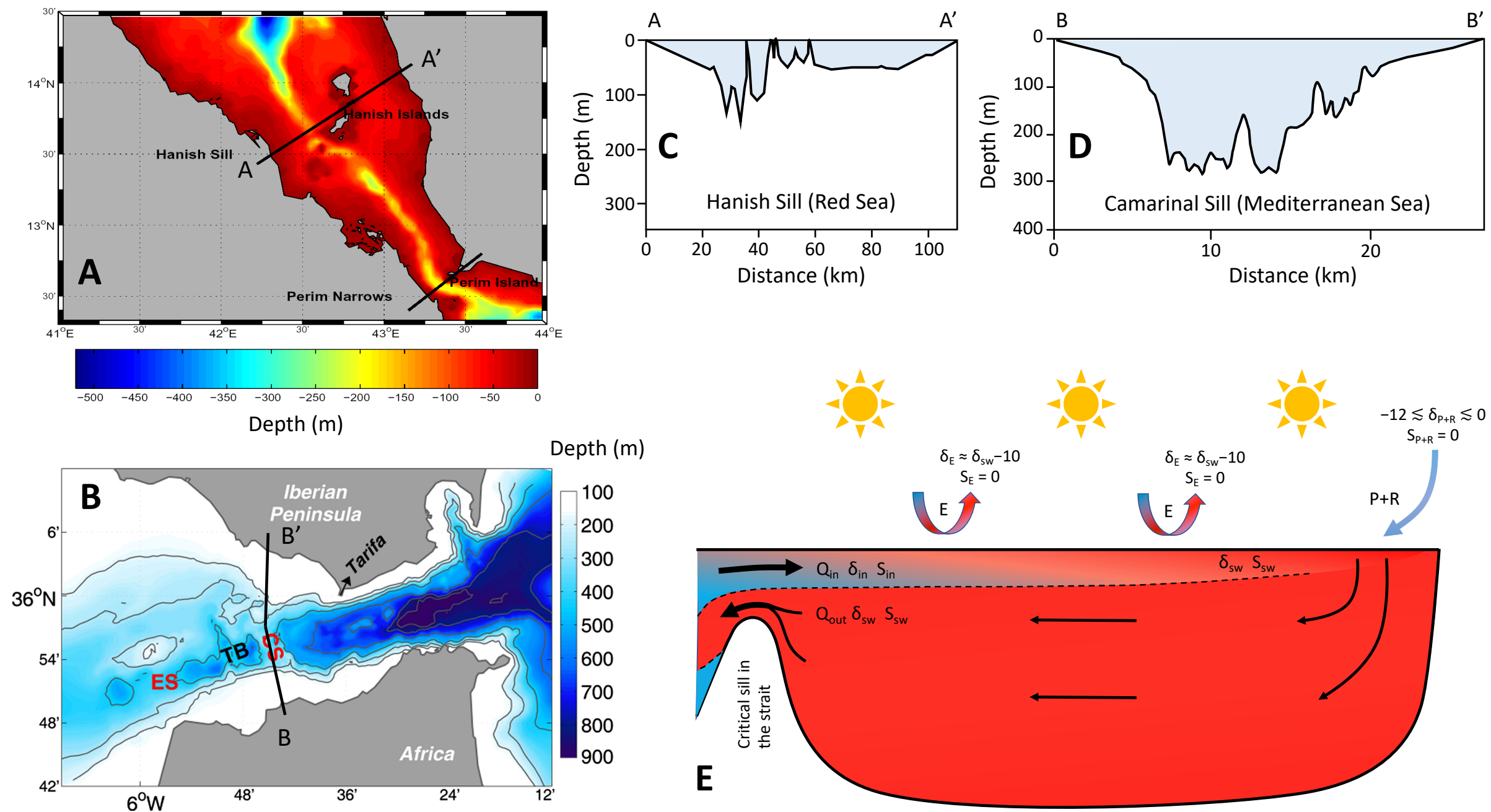


Figure 8

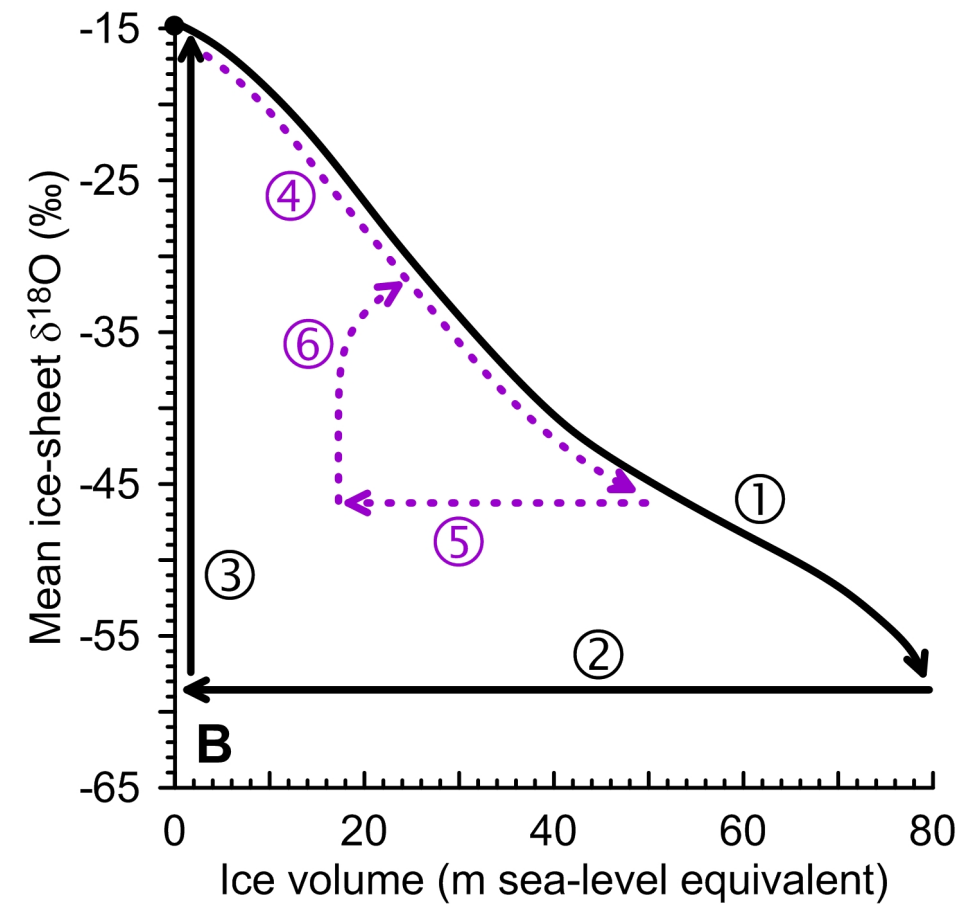
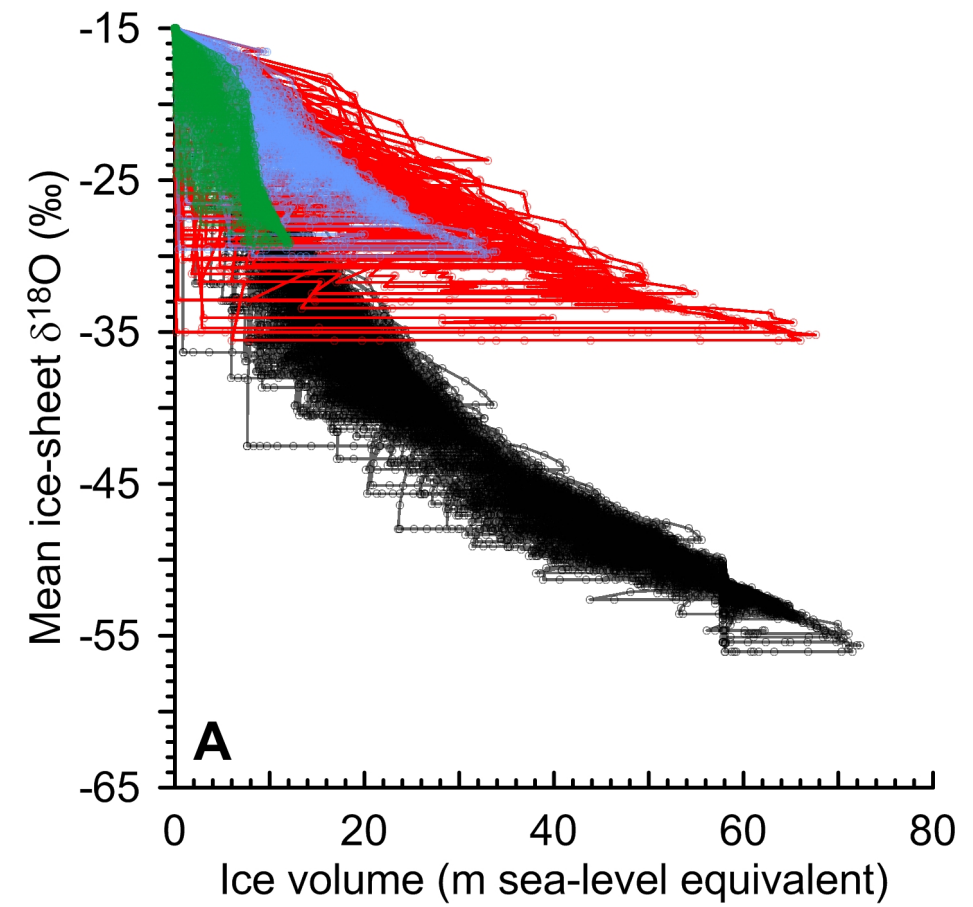


Figure 9

Last 550 kyr (before tuning)

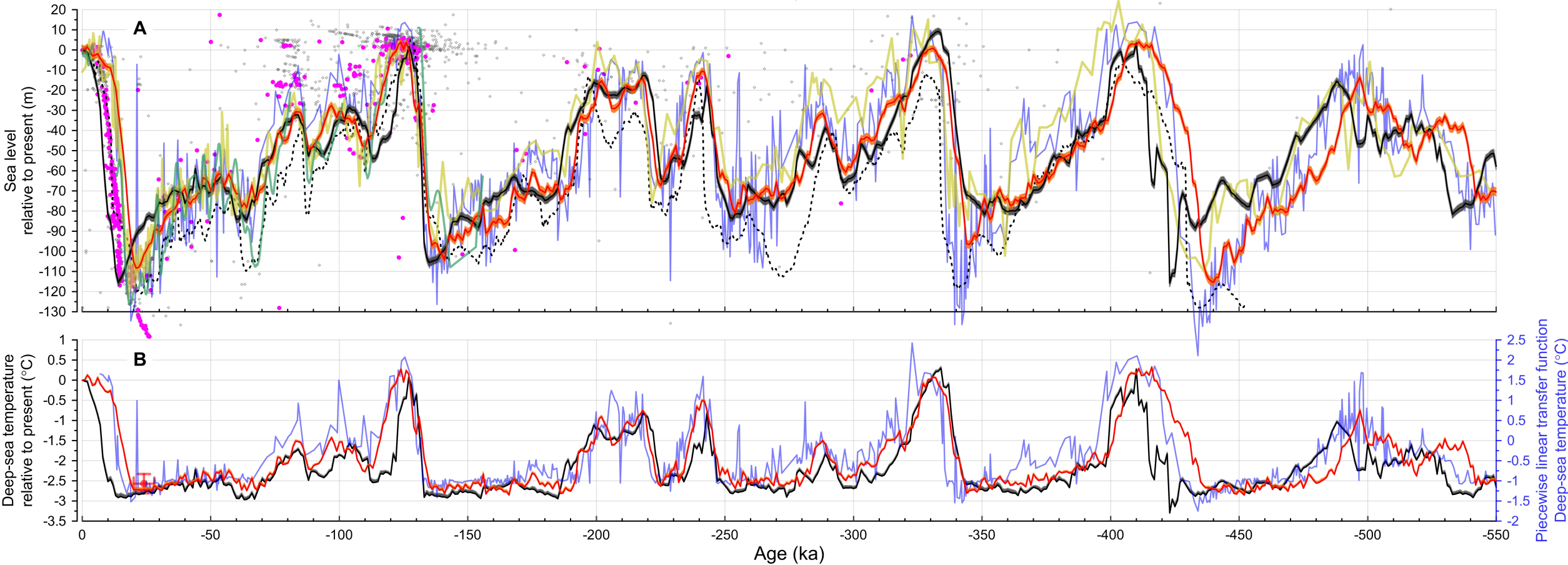


Figure 10

Last 800 kyr (before tuning)

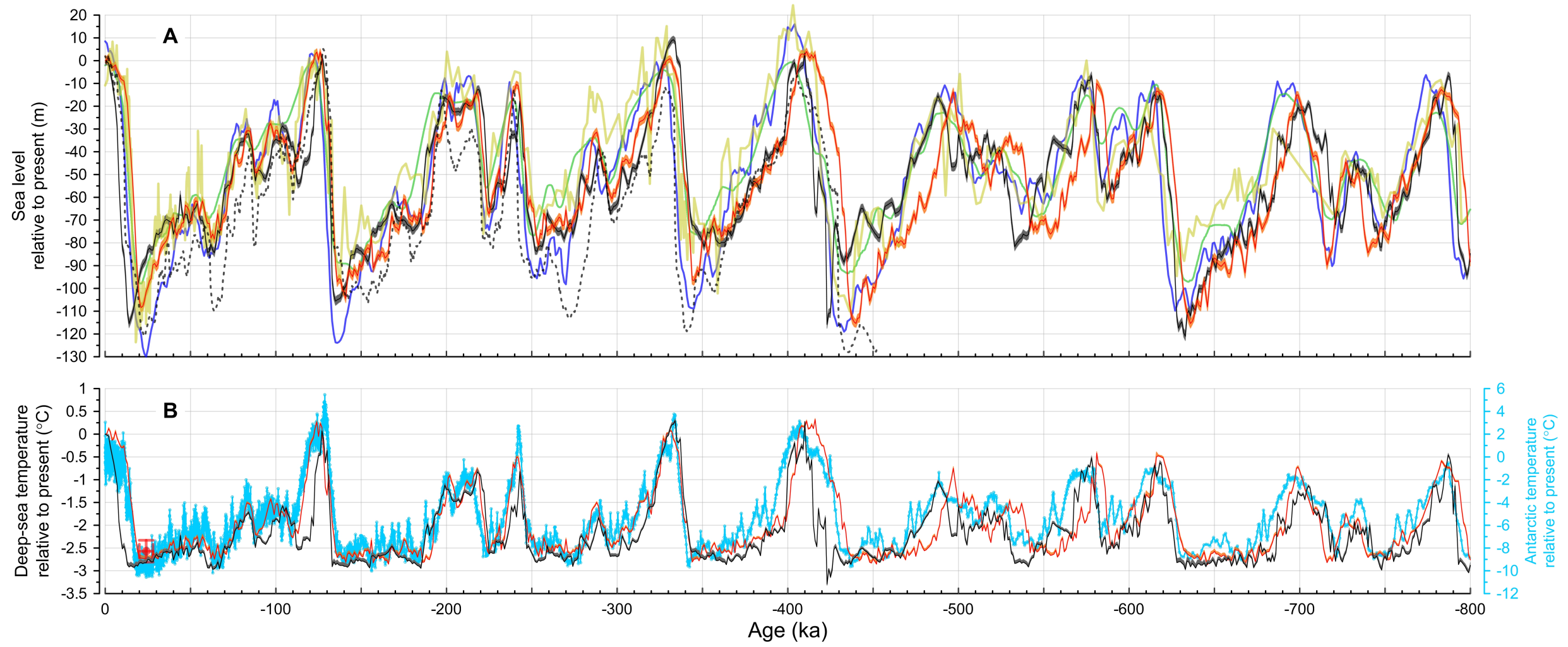


Figure 11

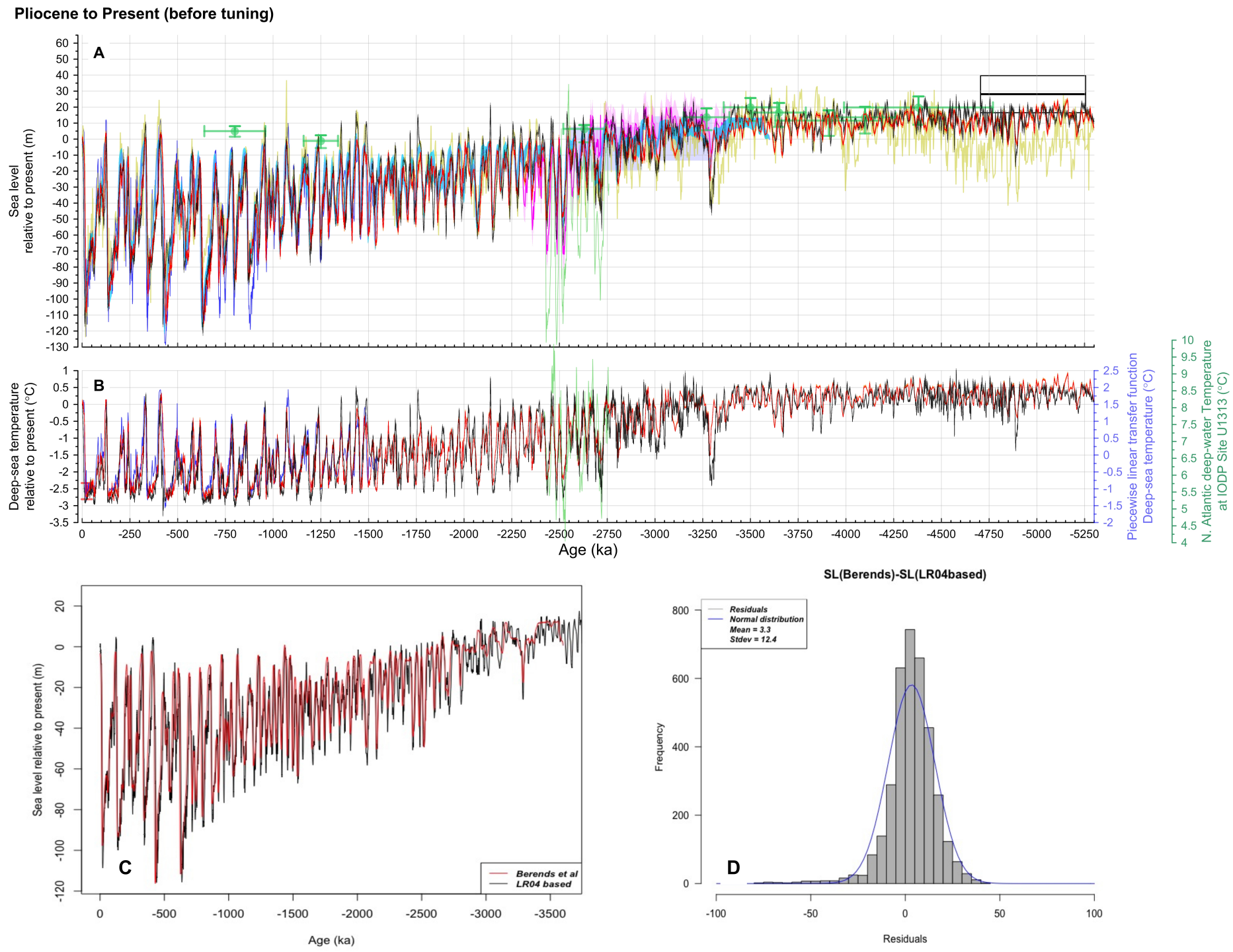


Figure 12

Last 550 kyr (tuned)

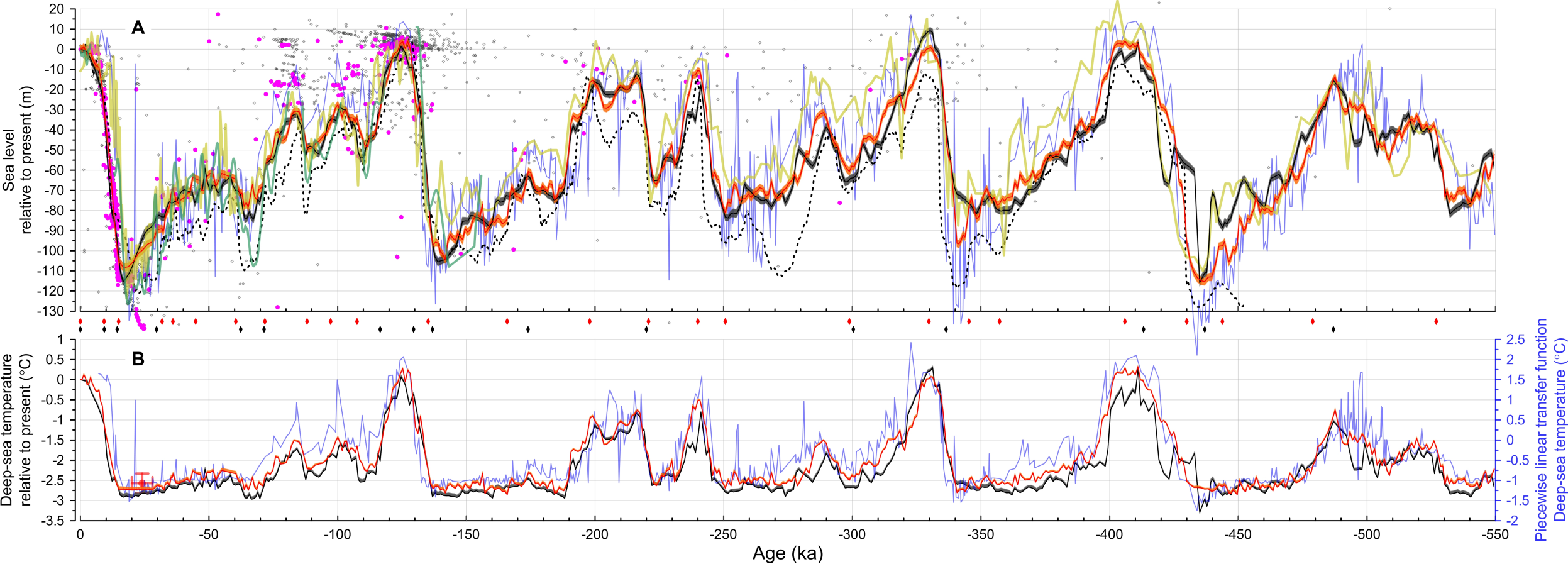


Figure 13

Last 800 kyr (tuned)

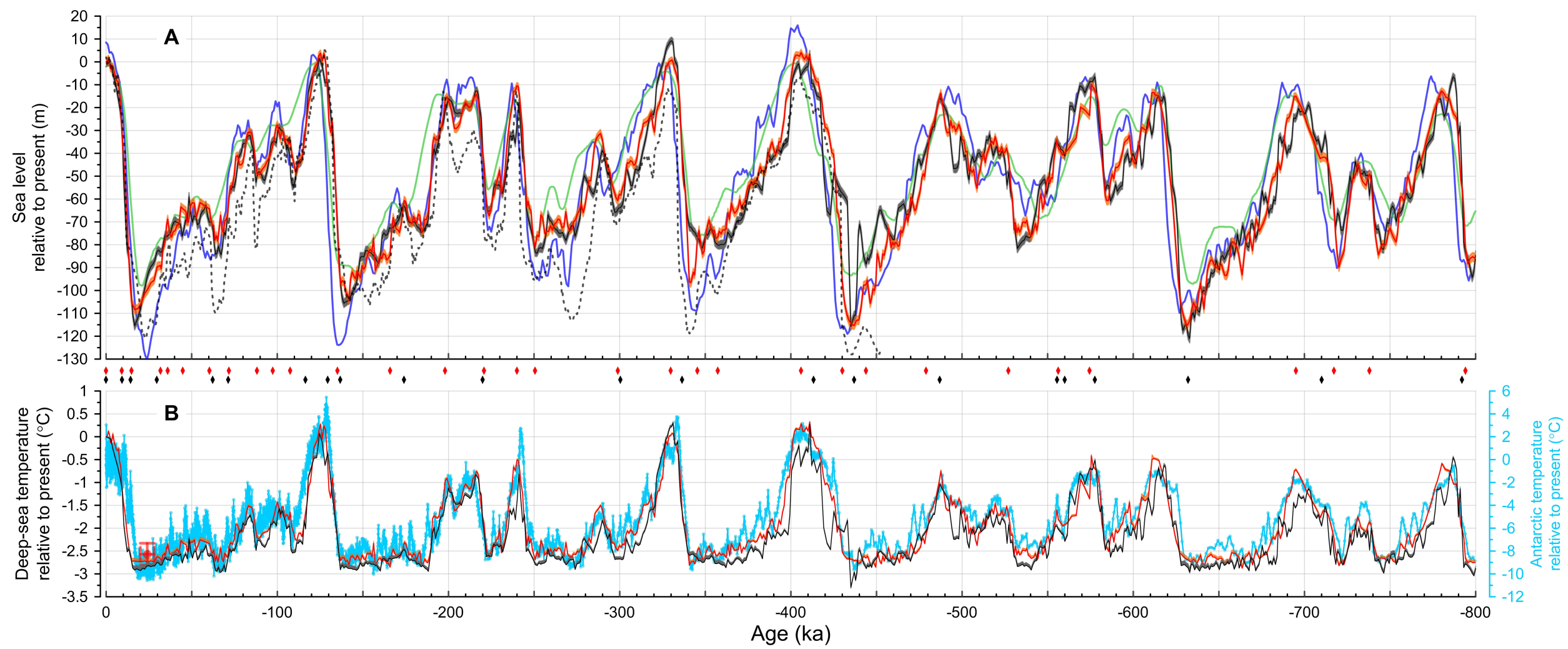
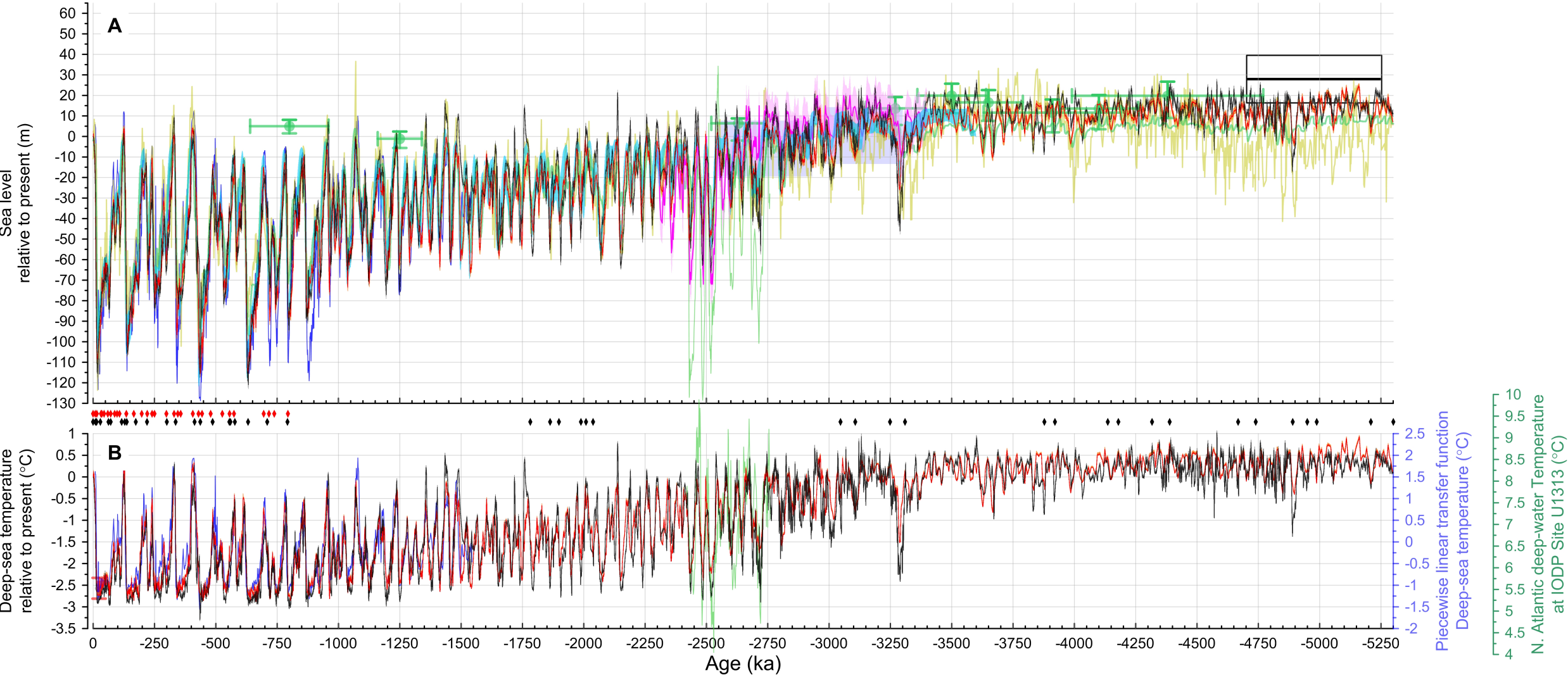


Figure 14

Pliocene to Present (tuned)



Pliocene to Present synthesis (tuned)

Figure 15

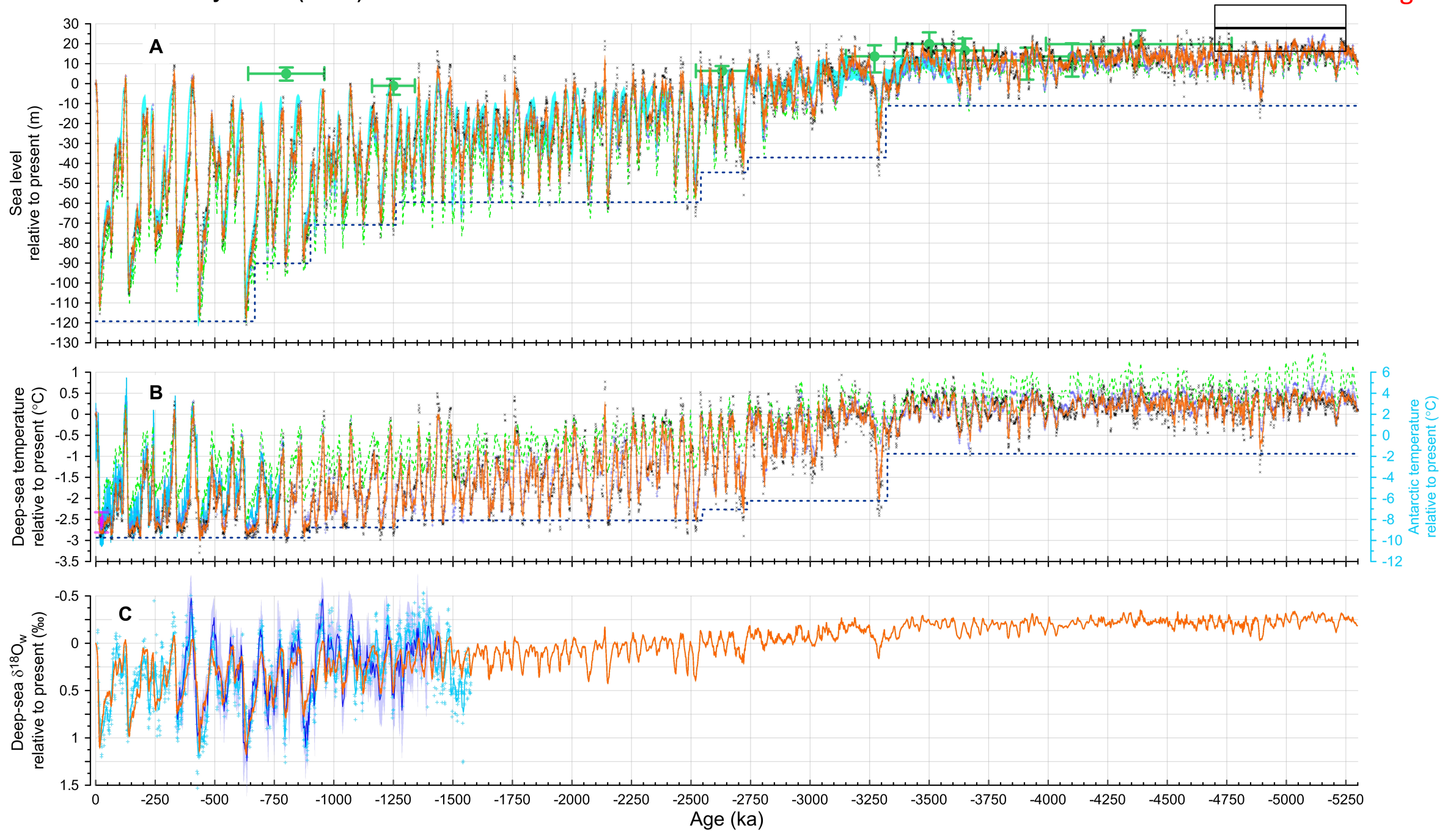
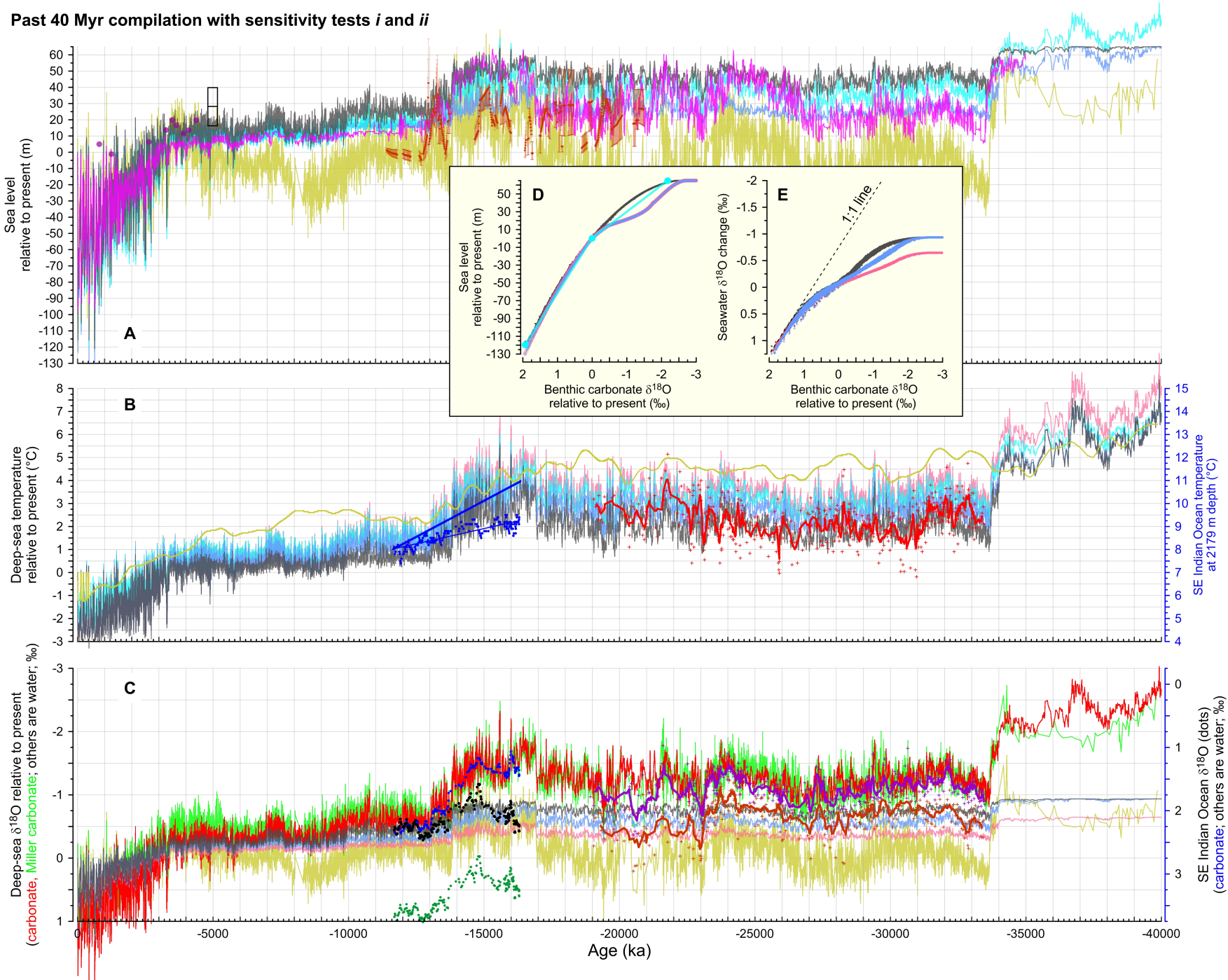
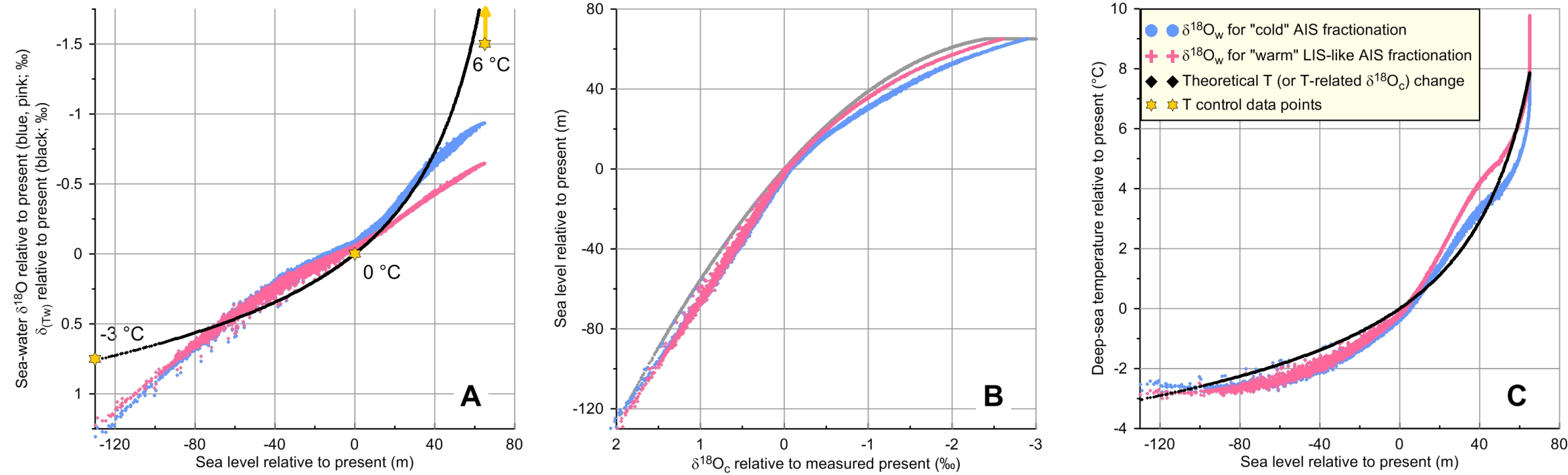
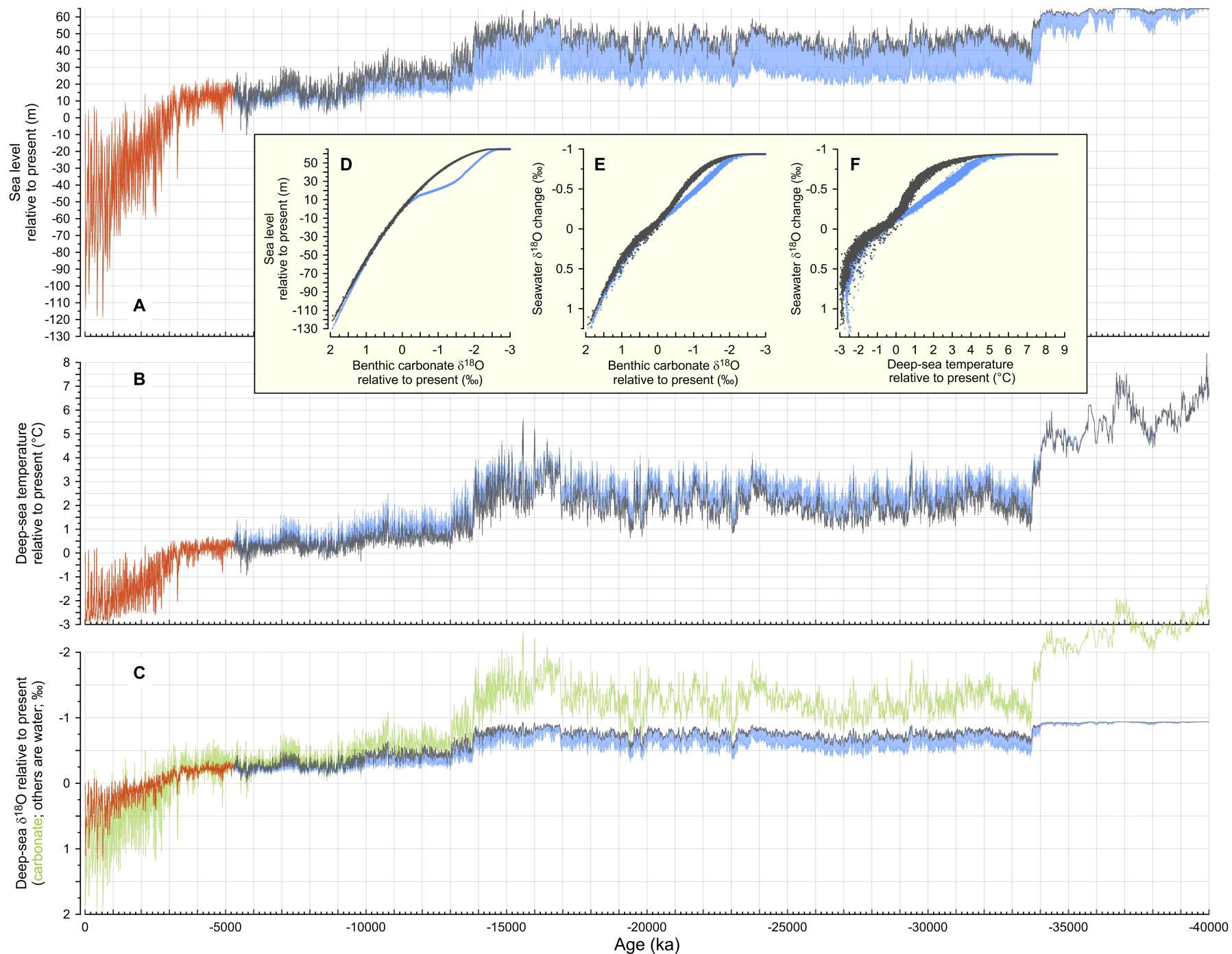


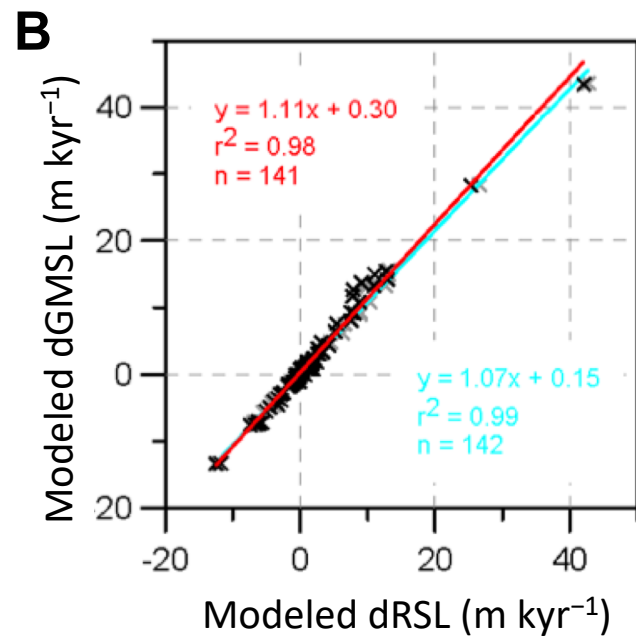
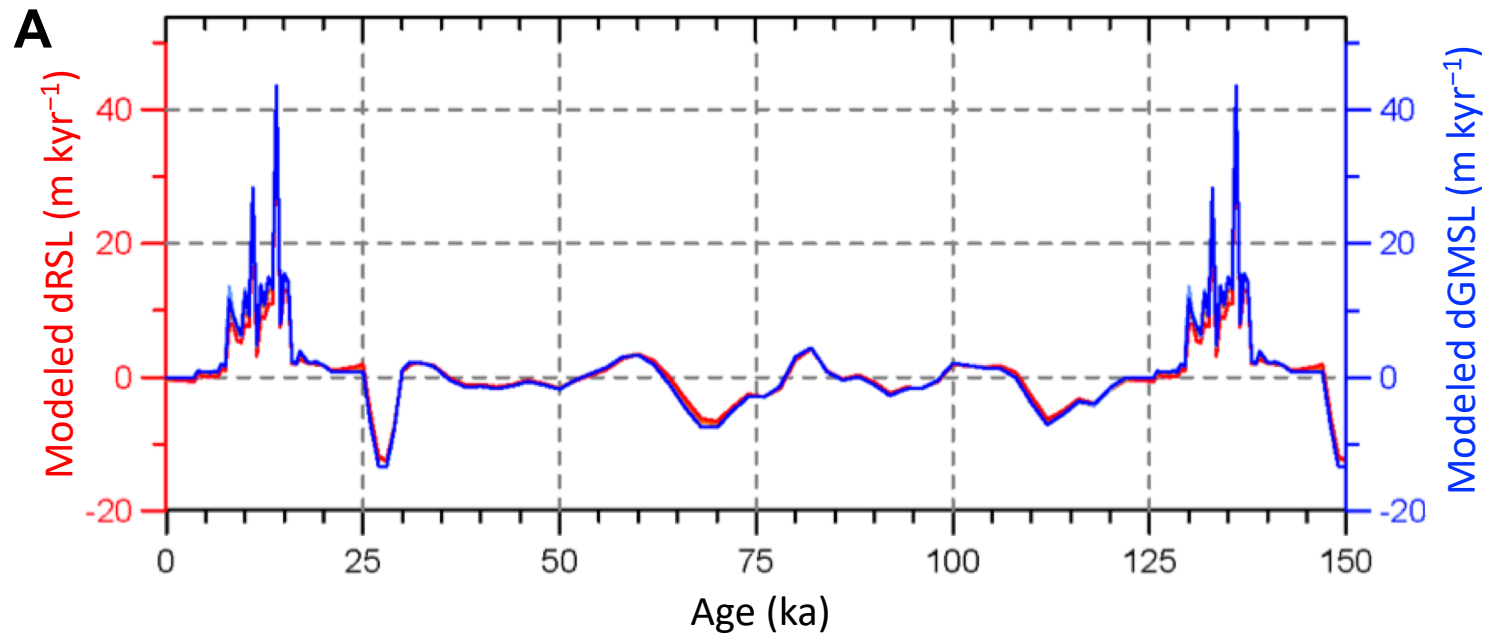
Figure 16



Theoretical assessment

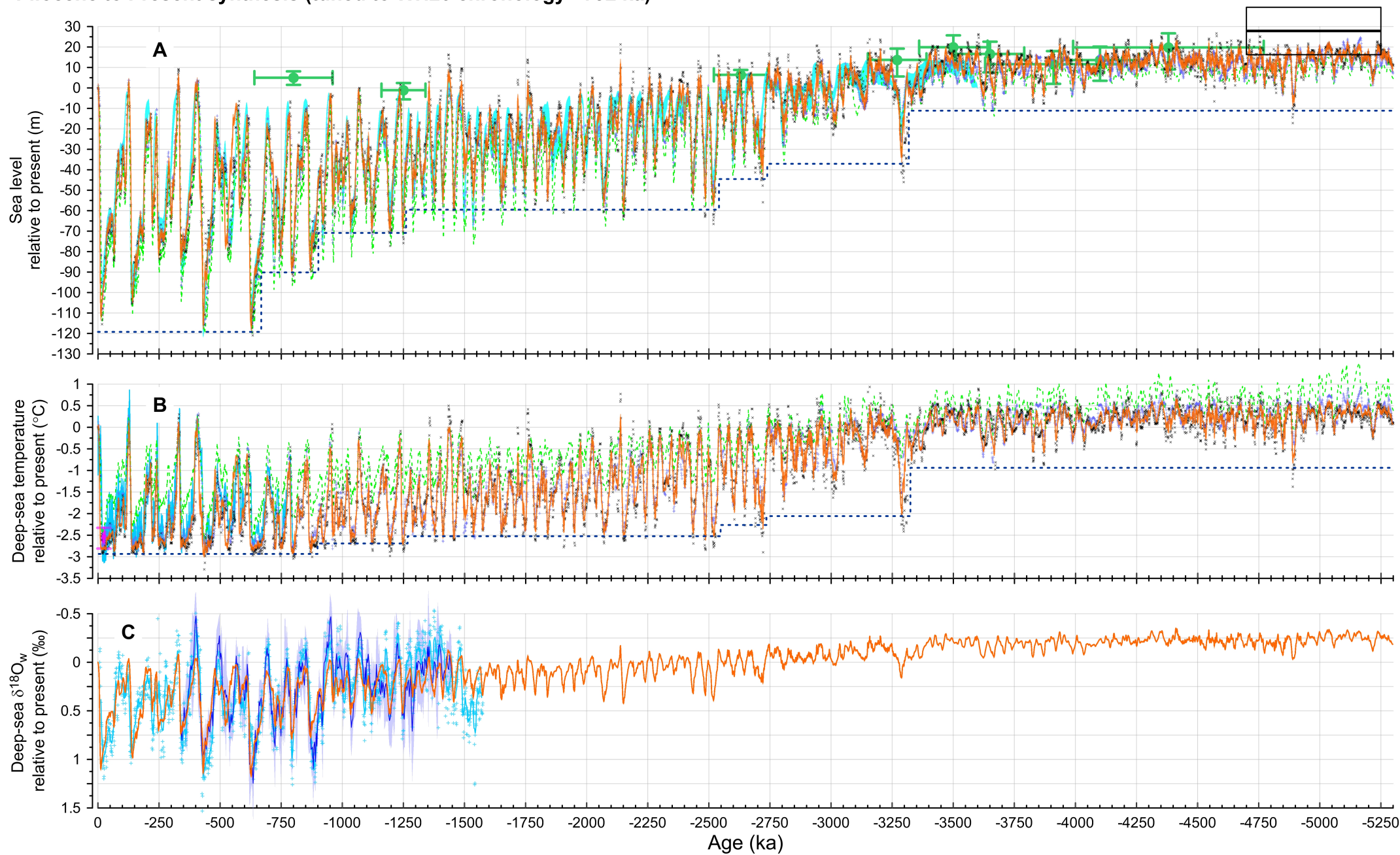






Pliocene to Present synthesis (tuned to WH20 chronology >792 ka)

Supplementary
Figure S2



Last 40 Myr synthesis with illustrative sea-level "pathway" through the uncertainty envelope

